Doctoral Dissertation
Doctoral Program in Physics (34th Cycle)

Design and optimization of a YBCO based superconducting bolometer

By

Andrea Napolitano
******

Supervisor:
Prof. Francesco Laviano

Referees:
Prof. G.P Pepe, Università degli studi di Napoli
Prof. N. Pompeo, Università degli studi Roma Tre

Politecnico di Torino
2022

Declaration

I hereby declare that, the contents and organization of this dissertation constitute my own original work and does not compromise in any way the rights of third parties, including those relating to the security of personal data.

Andrea Napolitano

2022

Acknowledgment

I would like to thank all the people who supported me in the path of my PhD, colleagues and especially friends. I am sorry, I cannot write all the names, you are too many, but if you are reading this sentence, then yes, I want to thank you.

Thanks to the "xkè" family, from the "bidelle", Lara e Consuelo, to the entire tutor team. You helped me to stay with my feet on the ground during the whole path. For sharing laboratories and pizzas, and still waiting for the karaoke. Happy to be part of this family, which is evolving with time, and ageing well, such a board game.

To the "Tatratea" group, for the dinner and the night spent together in a small house in the mountain or in a Brazilian reproduction in the city.

Thanks to all the AUT family, for the parties and the training, for the transfer and the tournament. Thanks to my team, Moletov. You drain my energy and give me the spirit that I need, I always feel welcomed despite my various departure in different teams. Thank you, Franza for creating such a great team and to all cutters and handler which manage such a wired player.

To all the colleagues from the electronic to management department, from chemistry to material engineering, from the underground laboratories up to the third floor. Thanks for sharing a coffee, listening to me and supporting me on many occasions. Thanks to the MESH group, from the youngest to the wisest, to Michela and Simone, because you shared much time and struggle, Daniele, because you opened my way, Laura, always available and open, and Francesco.

Abstract

This thesis deals with the optimization of a Transition Edge Bolometer (TEB) and the preliminary design of a Hot-Electron Bolometer (HEB), both based on optimally doped $YBa_2Cu_3O_{7-\delta}$ (YBCO) films. This work partly fulfils the milestones of the INFN-TERA project.

The introduction provides a general overview of the phenomenology and theories of superconductivity, emphasizing aspects such as vortex dynamics and the difference between type I and type II superconductivity. Then, the most promising technological superconducting materials are summarized before focusing on the YBCO films, whose crystal structure and phase diagram are presented. Finally, the application of the THz frequencies and the detectors working in this spectrum are introduced, before directing the attention to the working principle of a TEB: responsivity, noise, and time constant are presented, namely concepts that will be used in the following parts of the work.

Section 4 focuses on the YBCO based TEB and its optimization. The choice of the MgO substrate based on the optimal lattice matching with YBCO and its both electrical and thermal properties is explained. Then, the irradiation through high-energy heavy-ions for modifying the RvsT curve are described before the presentation of a portable cryostat in which the bolometer is held. Using the experimental data, the optimization of the working conditions is carried out, in terms of temperature, on the basis of the general study of the interplay between responsivity and noise, which will be the starting point for the simulation work. The bolometer is then reproduced with the finite element method employing the software COMSOL Multiphysics®. The first simulations helped in determining the most suitable materials for the sensor housing, which will be used for a detailed study of the response of the detector. Finally, a preliminary study of a new layout is realized and compared with the original geometry.

The last section is devoted to the design of an YBCO based HEB and the theory behind it. The high-frequency response is studied employing the SONNET® simulation software, mainly for matching the 50 Ω of the input impedance. The

final configuration is then manufactured through Electron Beam Lithography (EBL) after the deposition of the YBCO film by means of Pulsed Laser Deposition (PLD), still on a MgO substrate. The fabricated devices are characterized, then the results are used for calculating the performance of the detector.

Contents

List of Figures

List of Tables

List of abbreviations

GL	Ginzburg-Landau
LTS	Low-Temperature Superconductor
T_C	Critical Temperature
LN_2	Liquid Nitrogen
B_C	Critical Magnetic Field
J_C	Critical Current Density
HTS	High Temperature Superconductor
IBS	Iron-Based Superconductor
H_C	Critical Filed
RvsT	Resistance Temperature
ρvsT	Resistivity Versus Temperature
H_{C1}	Lower Critical Field
H_{C2}	Upper Critical Field
λ	London Penetration Depth
ξ	Coherence Length
Φ	Quantum Flux ($\approx 2 \cdot 10^{-15}\, T \cdot m^2$)
FLL	Flux-Line Lattice
TAFF	Thermally-Assisted Flux Flow
$H_{IRR}(T)$	Irreversibility Field
FC	Field Cooling
ZFC	Zero Field Cooling
$\Psi(r)$	order parameter
Δ	Superconducting energy gap
MTS	Medium Temperature Superconductor
MgB_2	Magnesium Diboride

NbTi   Niobium-titanium

NbN   Niobium Nitride

JJ   Josephson Junction

SIS   superconductor-insulator-superconductor

SNS   superconductor-Normal metal-superconductor

LHe   Liquid Helium

SQUID   Superconducting Quantum Interference Devices

THz   Terahertz

SMES   Superconducting Magnetic Energy Storage systems

YBCO $YBa_2Cu_3O_7$

Bi2212 $Bi_2Sr_2CaCu_2O_X$

Bi2223 $Bi_2Sr_2Ca_2Cu_3O_X$

1G   First generation

2G   Second Generation

AF   Antiferromagnetic

CDW   Charge Density Wave

PLD   Pulsed Laser Deposition

CVD   Chemical Vapor Deposition

MOCVD   Metal-Organic Chemical Vapor Deposition

CSD   Chemical Solution Deposition

SQIF   Superconducting Quantum Interference Filters

FIR   far infrared

FET   Field-Effect Transistor

TERA   High field Terahertz Era

TCR   temperature coefficient of resistance

NEP   Noise Equivalent Power

S/N	Signal-To-Noise Ratio
TEB	Transition Edge Bolometer
FEM	Finite Element Method
THEVA	Theva Dünnschichttechnik GmbH
ϵ_r	dielectric constant
LNL	Laboratori Nazionali di Legnaro
INFN	Istituto Nazionale di Fisica Nucleare
HEHI	High-Energy Heavy Ions
SMD	surface mounted device
PID controller	proportional–integral–derivative controller
PDE	Partially Differential Equation
HEB	Hot-Electron Bolometer
CPW	coplanar guideline
Z0	characteristic impedance
W	trace width
S	ground plane spacing
FFT	Fast Fourier Transform
EBL	Electron Beam Lithography
IPA	Isopropyl Alcohol
PVD	Physical Vapor Deposition
RIE	Reactive Ion Etching
XRD	X-ray diffraction
SEM	Scanning Electron Microscope

1. Superconductivity: phenomenology and theory

1.1 History

The phenomenon of superconductivity was discovered more than 100 years ago by Heike Kamerlingh Onnes, favored by the capability of liquefying helium. While studying the behavior of mercury at low temperatures, he discovered that its electrical resistance disappears below 4 K [1]. Since 1911, superconductivity has been extensively studied; many other materials have been discovered to become superconductors, and applications have been developed in various fields [2].

While superconductivity was investigated in various materials, numerous theories have been proposed to explain this exotic phenomenon. The London brothers proposed the first model for describing superconductivity in 1935 [3] based on empirical observations, which was then followed by the Ginzburg-Landau (GL) theory in 1950 [4], which introduced the quantum formulation by means of the complex order parameter. Finally, a fascinating picture (the so-called BCS theory), for explaining the superconductivity was given by J. Bardeen, L. N. Cooper, and J. R. Schrieffer, with the introduction of the so-called Cooper pair [5].

These theories well explain the behavior of Low-Temperature Superconductors (LTS), which include pure elements and some compounds. They usually present low critical Temperature (T_C), further below the Liquid Nitrogen (LN$_2$) boiling point, low critical magnetic field (H_C), and well fit the theoretical prediction [6].

Almost 30 years ago, the discovery of the High-Temperature Superconductors (HTS), a large family of ceramic materials belonging to the cuprates, broke the barrier of the LN$_2$ temperature. These compounds present high T_C, critical current (J_C), and upper critical field (H_{C2}) but, because of their complex structure, they usually present high anisotropy and difficulties in manufacturing [7][8]. In addition, a complete and exhaustive theory able to explain their behavior has not been formulated until now [9].

More recently, a new family of superconductors has been discovered in recent years: the Iron-Based Superconductors (IBS) [10][11]. Despite a lower T_C than cuprates, they present a smaller anisotropy and still a considerably high H_{C2}, and therefore they may be promising for applications in the near future.

1.2 Phenomenology

Superconductivity is a particular state of matter in which two conditions must be met simultaneously: the perfect conductivity and the perfect diamagnetism. In order to remain in the superconducting state, the material needs to stay below the T_C, the current flowing in the sample must result in a current density lower than J_C, and the magnetic field must be lower than H_C. These parameters, which are proper of each material, are interconnected and can be presented in a three-dimensional space, as shown in Figure 1a.

a)   b)
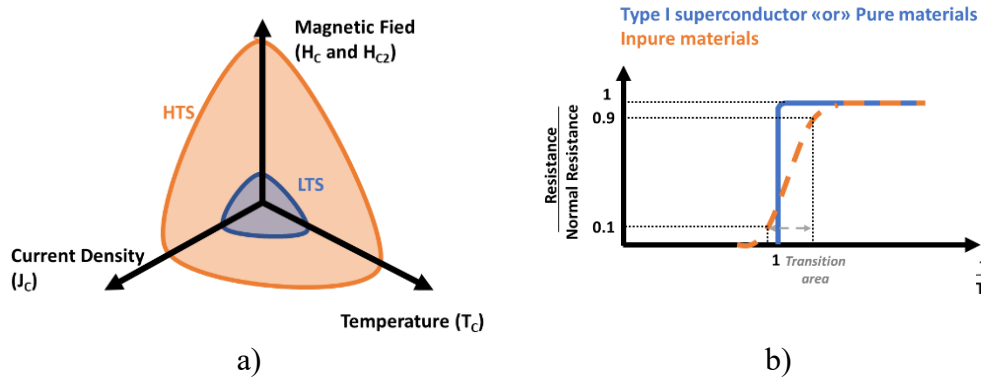
Figure 1: a) Superconducting critical surface parameters for LTS (blue) and HTS (orange), not in scale. b) The transition between superconducting and normal state for two example material, impure (orange) and pure (blue)

A material shows perfect conductivity when it exhibits a null electrical resistance. The transition between the normal and the superconducting state occurs in the so-called transition area. It is defined in correspondence to the resistance variation from 10% to 90% of the normal state value. It can range from fractions of Kelvin to several ones, depending on the material, its purity, and the treatment it has undergone. A remarkable difference also appears between LTS and HTS, as schematically shown in Figure 1b; the former ones are usually associated with sharper transitions. The T_C can be defined as the temperature which corresponds to the highest slope of the curve resistance versus temperature (RvsT).

On the other hand, the perfect diamagnetism, known as the Meissner effect, discovered in 1933 [12], refers to the predisposition of a superconductor to expel any external applied magnetic field below the H_C. This effect fundamentally differentiates a perfect conductor from a superconductor, which exhibits a truly macroscopic quantum behavior. The perfect diamagnetism is fully achieved only for low magnetic fields, after which part of the magnetic field starts penetrating the material, wholly or partially destroying the superconducting phase.

The transition between the normal and the superconducting state is observed in many other physical parameters, such as specific heat, bulk modulus, or friction coefficient, confirming that the superconductivity is indeed a new state of matter. For example, as the resistivity, also the specific heat shows a sudden variation at T_C; this phenomenon has been extensively studied in superconducting materials [13][14].

1.3 Type I and Type II

Superconducting materials can be divided into two main families, type I and type II, depending on the material response to an external magnetic field. A schematic view of the different behavior of type I and II are shown in Figure 2a.
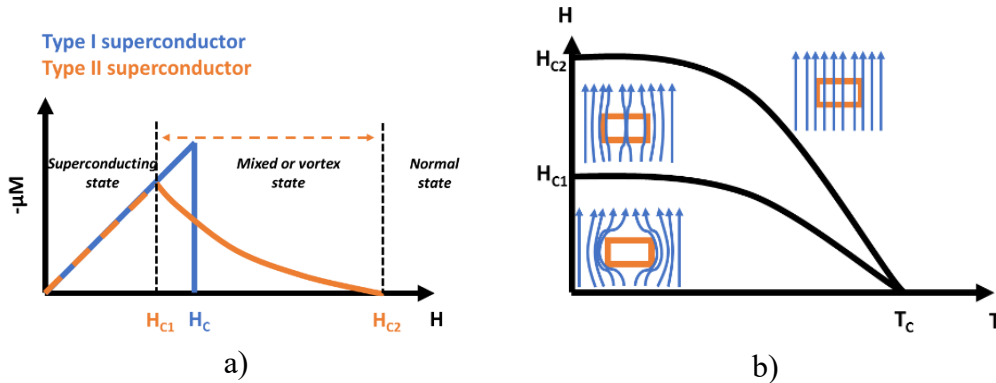
Figure 2: a) Behavior of type I (blue) and type II (orange) superconductor in a magnetic field b) The magnetic field penetration in a type II superconductor

Many pure elements display a type I superconductivity. They expel the whole magnetic field until it reaches the critical value of H_C, which is usually relatively small. When the magnetic field reaches a specific value, it is possible to identify a portion of material that passes to the normal state where the field penetrates, leaving the other part in the superconducting state [15]. Lead, mercury (phase α), indium, and tantalum are some examples of type I superconductors.

Type II superconductors include compounds, alloys, and a few other elements such as niobium. They completely flush out the magnetic field up to a first lower critical field H_{C1} usually lower than the H_C of type I superconductors. Above this threshold, the magnetic field partially penetrates inside the superconductor as vortices (also named fluxons or flux lines), locally destroying the superconductivity, as shown in Figure 2b. When the external field reaches the upper critical field H_{C2}, is usually considerably larger than H_C and hence H_{C1}, a continuous, entirely superconducting path is not available anymore, and therefore the material passes to the normal state [16][17]. The penetration of the magnetic field through the vortices allows the type II materials to withstand stronger magnetic fields before losing their superconductivity, as shown in Figure 2a. After H_{C1}, the magnetic field is less and less screened and the Meissner effect is strongly suppressed compared with type I superconductors. Type II materials are more numerous than type I ones, and they include cuprates, niobium and its alloys, IBS, and some other families.
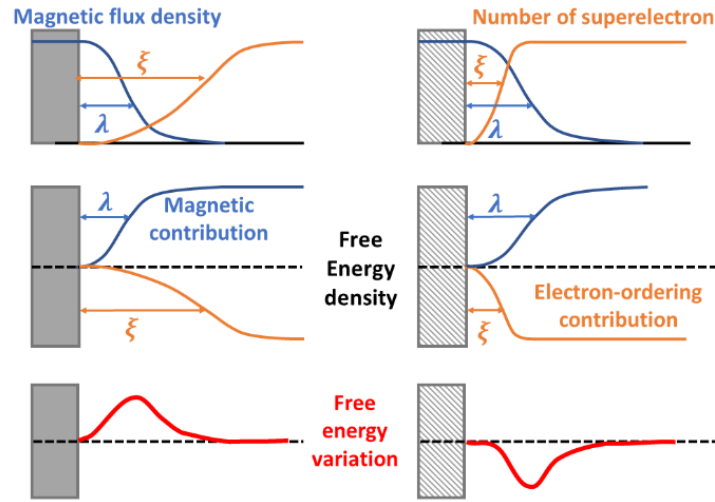
Figure 3: Variation of the free energy density at the interface between the normal (grey) and superconducting state for type I (left) and type II (right). The magnetic contribution (blue line) and electron-ordering one (orange) are represented in the upper sketches, while the sum is reported in the last one. The advantage for type II in creating the interface is evident because of the negative contribution to the total free energy

From the theoretical point of view, the difference between the two types of superconductors is expressed by the variation of the free energy at the interface between normal and superconducting states. It is useful to consider the ratio between two important parameters: the London penetration depth (λ) and the

coherence length (ξ). It gives a reasonable estimation of the type of superconductor [18]. If the parameter κ expressed as λ/ξ is lower than $1/\sqrt{2}$ ($\kappa = \lambda/\xi \leq 1/\sqrt{2}$), then the superconductor is a type I, otherwise a type II [19][20]. These two lengths are directly linked to the magnetic and electronic ordering which affect the free energy. Their ratio is a useful parameter for determining if a material shows an advantage in having an interface between normal and superconducting states or not, as shown in Figure 3.

The type I superconductors have no advantage in creating interfaces between the two states, while type II do have. Therefore, the latter ones try to maximize the length of this interface by including more and more vortices in the materials.

1.4 Vortices

When the magnetic field reaches H_{C1}, vortices start penetrating type II superconductors. Vortices have a length scale of ξ and are surrounded by a current that decays over λ, schematically reported in Figure 4 and previously shown in Figure 3. Each vortex carries precisely one flux quantum which is the minimum flux quantity achievable ($\Phi = \frac{h}{2e} \approx 2 \cdot 10^{-15}\ T \cdot m^2$) and, again, remarks the quantum nature of the phenomenon [21][22].
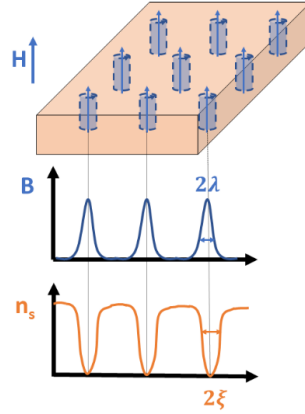
Figure 4: Schematic view of the parameters involved in the vortex penetration, the magnetic field (blue), and order parameter (orange). The current flows in the same direction in all vortices. The magnetic field penetrates and decays over λ and the superconductivity is suppressed in a distance ξ

The superconducting current surrounding the vortices creates a repulsive force among them, and therefore the distance is maximized to reduce the mutual interaction. In a perfect sample, it results in a triangular distribution, called flux-

line lattice (FLL), which maximizes the distance and reduces the interaction between vortices, as reported in Figure 5a and Figure 5b [23][24].

a)   b)
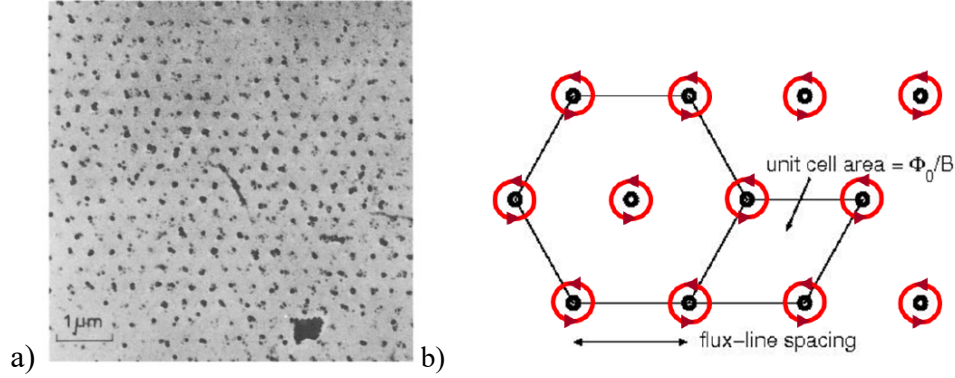
Figure 5: a) Distribution of the vortices in the superconductor. b) The sketch highlights the direction of the current and the geometrical distribution of the vortices

1.4.1 Flux pinning

In real samples, superconductivity is locally depressed in correspondence of crystal defects such as grain boundaries, dislocations, and inclusions [25][26]. Similarly, the nucleation of a vortex reduces the condensation energy in a region corresponding to the volume occupied by its core. Consequently, when the vortex core is located in correspondence of a crystal defect, there is a net energy gain for the superconductor, and the vortex remains anchored to the defect until it obtains an energy higher than the pinning one [27]. When the magnetic field is low, vortices may arrange themselves in a non-regular disposition to occupy higher potential sites created by defects, usually placed randomly in the sample [28]. This phenomenon, called vortex pinning, refers to the friction on vortex movement due to crystal defects, and it is weakened by thermal fluctuations, applied electrical current, and magnetic flux density. In the presence of flux pinning, it is possible to identify two different phases (Figure 6); the vortex glass, at high temperature and magnetic field, and the Bragg glass, in which the superconductor displays a long-range order because of the lower thermal and magnetic energy [29].
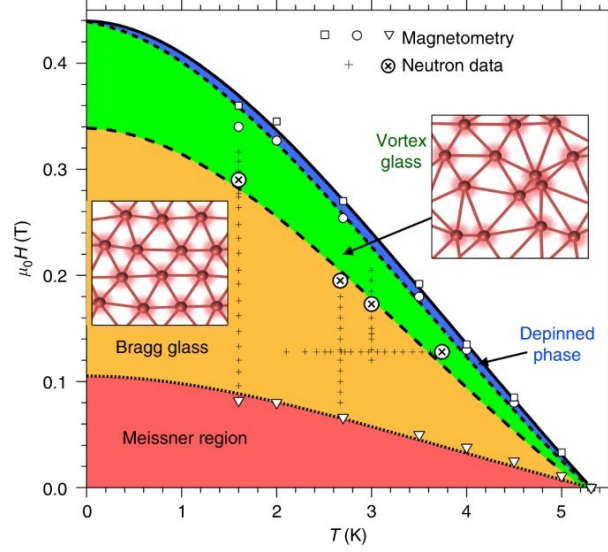
Figure 6: Different magnetic phases represented in terms of the magnetic field and the temperature [30]

1.4.2 Flux motion

Thermal fluctuations may provide enough energy to the fluxon to leave the pinning center, but it scales as the temperature: the lower it is, the lower is the probability too. When the energy provided to the vortices is high enough, it melts the FLL and generates the vortex liquid phase until the H_{C2} is reached. Indeed, another origin for the vortex motion is the Lorentz force, which is due to a current flowing in the superconductor (1.1), and tends to move vortices normally to it. This phase is called flux creep, and it is associated with a small resistivity due to the limited flux speed and low depinning probability.

$$\boldsymbol{F_L = J \times B} \qquad\qquad 1.1$$

The relation between the Lorentz and the pinning force defines the critical current density; when the first overcomes the second one, vortices start moving (1.2). Other contributions, such as the vortex mass and the Magnus force, are usually neglected [31][32].

$$F_P = F_L = J_C \cdot B \qquad\qquad 1.2$$

Eq. (1.2), where F_L is the Lorentz force, F_P is the pinning one, J_C is the critical one and F_P is the pinning force. When $J \geq J_C$, the dissipative electric field induced

by the lattices' motion creates a flux flow resistivity, ρ_f, which can be expressed as (1.3). Here, μ is linked to the material viscosity and can be seen as the friction of the vortices.

$$\rho_f = \frac{E}{J} = B \cdot \frac{\Phi}{\mu} \qquad\qquad 1.3$$

Between these two phases, i.e., when $0 < J \ll J_C$, the material passes from the thermally-assisted flux flow (TAFF) to the flux creep phase. Here the system acts like a viscous liquid and shows a resistivity which can be expressed as (1.4), in which ρ_0 and U_0 are function of the flux and the temperature, and k_B is the Boltzmann constant [33].

$$\rho = \rho_0 e^{-\frac{U_0}{k_B T}} \qquad\qquad 1.4$$

1.4.3 Pinning effect on the magnetic field and critical current

The flux pinning has a substantial impact on the magnetic field in the superconductor. Since the pinned vortices freeze the magnetic lines in the superconductor, a magnetic hysteresis appears, as schematically reported in Figure 7.
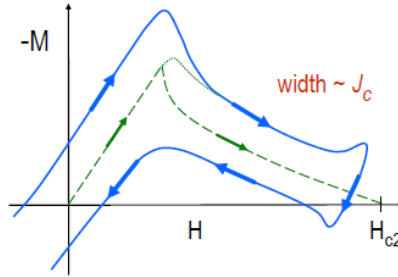
Figure 7: Magnetic hysteresis due to the flux pinning effect

The irreversibility field $H_{IRR}(T)$ is an important parameter directly linked with the vortex pinning and the temperature, which affect the pinning strength. It represents a threshold field above which the magnetization after cooling (FC) and zero-field cooling (ZFC) displays the same curve, and therefore, there is no hysteresis loop. It represents the transition between fields for which the vortices are pinned, below $H_{IRR}(T)$, and are free to move, above it. Since it defines two areas

with and without dissipation, it is usually the crucial parameter for technological applications.

The interaction between the current density and the pinning potential is represented in Figure 8a. Here is highlighted the current contribution in triggering the movement of the vortex, i.e., the ratio between the Lorentz and pinning force. Indeed, the pinning effect strongly affects the E-J curve (Figure 8b), in which it is possible to define four main zones. First, the fully superconducting state, where the pinning force is higher than the thermal fluctuation and Lorentz force and, therefore, there is no dissipation. Then the flux creep, when dissipation starts to appear due to the vortex motion. This regime starts when the current density reaches the critical value J_C: above this threshold, the dissipation quickly grows and can lead to a sharp transition to the normal state due to the thermal runaway of the material. It can bring the superconductor in the flux flow regime with even higher dissipation before reaching the normal state with a sudden jump in the resistivity. From this point the Joule heating plays an important role in the transition, accelerating it and bringing the superconductor into the ohmic regime.

a)   b)
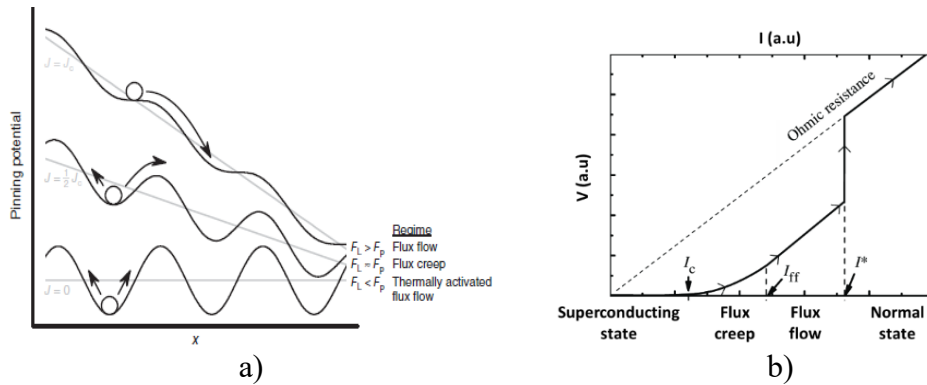
Figure 8: a) Effect of the current density on the different regimes and b) different phases in the I-V characteristic

1.5 Theory

The phenomenology explained above was investigated deeply for a long time, during which several theories have been proposed. The first attempt to explain the superconductivity was based on empirical observations, considering it in a simple classical way. Then, the introduction of the quantum formalism enables to both describe and understand the principles behind the phenomenology of superconductivity.

1.5.1 London theory

The London brothers proposed the first theory that describes both perfect conductivity and perfect diamagnetism in 1935. They proposed a two-fluid system starting from a classical description of the phenomenon. One represents standard electrons, responsible for the "normal" conductivity at temperatures higher than T_C and still present below it. The other is composed of charge carriers, called super-electrons, accountable for the superconducting current, which appears below T_C.

According to this theory, the percentage of super-electrons is proportional to the temperature and falls to zero at $T \geq T_C$. Below T_C, the behavior of the electrons is described by the Drude equation [34], in which the relaxation time for the super-electrons is set to infinite, i.e., they do not undergo scattering. As a result, the two London equations (1.5 and 1.6) describe the superconducting current. Here Js is the current of super-electrons attributed to the super-electron density n_S, e^* and m^* are the effective charge and mass of the super-electron, respectively twice the charge and the mass of the electron, and E and B are the electric and the magnetic field.

$$\frac{dJ_s}{dt} = \left(\frac{n_s e^{*2}}{m^*}\right) E \qquad\qquad 1.5$$

$$\vec{\nabla} \times J_s = -\frac{n_s e^{*2}}{m^*} B \qquad\qquad 1.6$$

As described by 1.5, a constant current density results in $E=0$, while when it varies in time, a voltage drop appears across the superconductor with consequential losses in the material. Eq. 1.5 describes the phenomenon of perfect conductivity, while Eq. 1.6 describes the Meissner state. Combining 1.6 and the Ampere's law, Eq. 1.7 is obtained, which describes the exponential decay of the magnetic field inside the material. In 1.8, the parameter λ, the London penetration depth, describes the characteristic length in which B decades to zero because of the screening current.

$$\nabla^2 B = \frac{1}{\lambda^2} B \qquad\qquad 1.7$$

$$\lambda = \sqrt{\frac{m^*}{\mu_0 n_s e^{*2}}} \qquad\qquad 1.8$$

1.5.2 Ginzburg and Landau theory

Ginzburg and Landau gave a more detailed and precise description of superconductivity in 1950. In contrast to the London theory, which considered the fraction of super-electron constant in the whole sample, the GL theory introduces the order parameter $\Psi(r)$ (1.9), which varies in the space in function of the magnetic field. It describes both the phase and the density of the superconducting fluid with an exquisite quantum formalism. The properties of order parameter Ψ varies only on the length scale of the coherence length, ξ (1.10), which is linked to the Fermi velocity, v_F, and the energy gap of the superconductor (Δ).

$$\Psi(\vec{r}) = |\Psi(\vec{r})| \cdot e^{i\theta(r)}$$

$$\Psi(\vec{r}) = \sqrt{n_s^*(\vec{r})} \cdot e^{i\theta(r)}$$

1.9

$$\xi \sim \frac{v_F \hbar}{\pi \Delta}$$

1.10

The variables previously described in 1.8 and 1.10, λ and ξ are the characteristic lengths of a superconductor and depend on the material. Their ratio discriminates materials between type I and type II superconductors.

The GL theory was obtained by calculating the difference of the Gibbs free energy per unit volume between the normal and the superconducting state. The spatial variation of $\Psi(r)$ is due to the presence of the magnetic field and, since a perturbative approach was used, the necessary condition was to set the study point at $T \sim T_C$ and truncate the expression to the second order. For some superconductors, i.e. type I, the formation of the surface between normal and superconducting state brings a positive contribution and therefore, vortices are not formed at equilibrium. On the other hand, for type II it is negative and, consequently, there is an advantage in creating them.

1.5.3 Abrikosov Contribution

A significant contribution to understanding the type II superconductor was brought by Abrikosov and his description of the vortex nature. In 1957, many years later after the first observation of type II superconductors, Abrikosov theoretically described their behavior in the framework of the GL theory. He described what was presented in section 1.4, including the geometrical distribution, the order parameter

suppression, and the magnetic properties. His contribution considerably helped to understand the role of impurities in superconducting materials [35].

1.5.4 BCS theory

Despite the success of the phenomenological model and the microscopic description provided by the previous theories, it was necessary to wait some more years before the mechanism responsible for superconductivity was identified. In 1957, Bardeen, Cooper, and Schrieffer proposed that the Cooper pairs could be at the base of the superconducting phenomenon [36]. The pair is composed of two coupled electrons that provide to the new quantum object an integer spin and, therefore, a boson behavior. This connection is due to the interaction between the electrons and the phonon lattice of the material: the first electron slightly deforms the lattice and consequently, the local potential; the second electron, with appropriate momentum and opposite spin, feels the attractive force and couples with the first electron forming the pair [5]. Because of their bosonic nature, the Cooper-pairs condense into the same ground-state described by the GL theory (1.11). In order to exist, the Cooper-pair needs to be energetically favorite compared with the single electron. Indeed, for $T < T_C$, the binding energy of the Cooper pairs is 2Δ (1.11), in which Δ is the superconductive energy gap.

$$\Delta \approx 2\hbar\omega_D e^{-\frac{1}{N(E_F)g_{eff}}}$$

1.11

$$\Delta \approx 1.76 k_B T_C$$

In 1.11 ω_D is the Debye frequency, E_F is the Fermi energy, $N(E_F)$ is the electron density state at that energy, g_{eff} is the effective electron-phonon coupling and k_B the Boltzmann constant.

The theoretical predictions of the BCS theory were confirmed in the following years by many experiments and calculations. Among the scientists who contributed to it, two noteworthy ones are Giaever and Josephson: the first scientist used quasiparticle tunneling to confirm the density of states and temperature dependence of the energy gap predicted by BCS, the second theoretically predicted that the Cooper pair could perform quantum tunneling through a narrow insulating barrier (Josephson effect) [37][38].

2. Superconducting materials and their applications

Superconductors can be classified according to different properties: the theoretical accordance with the BCS theory, the magnetic behavior, and the critical temperature.

Superconducting materials, which have a phononic mechanism at their bases and can be fully described by the BCS theory or its extension are called conventional superconductors. They fit the theoretical predictions, show a conventional electron-phonon mechanism and are mainly pure elements. The remaining materials, which represent the vast majority of superconductors, are categorized as unconventional ones [39].

The magnetic behavior determines if a material belongs to type I or type II. The two types respond differently to an external magnetic field and because of different magnetic and electronic contributions, the overall variation of the free energy at the interface between the superconducting and normal state is different. Technologically speaking, the choice of type I or II is strongly influenced by the requirements: type II materials present higher magnetic field and are used for power applications such as magnets, cable and motors [40][41][42], medical applications, environmental filed and many others [43][44]. On the other hand, type I superconductors have application mainly in sensor devices and research because of their low critical magnetic field [45].

The critical temperature is a parameter that provides a more straightforward classification. LTS present a T_C lower than 30 K and include all pure elements, niobium and its compounds, and the A15 class. HTS have a T_C noticeably higher than LTS, usually above the LN_2 boiling point. In recent years, it was possible to define a new category, the Medium Temperature Superconductors (MTS), which includes the MgB_2 and the IBS with T_C between 30 K and the LN_2. An overview of different superconducting materials (elements and compounds) with their discovery date and T_C is shown in Figure 9.
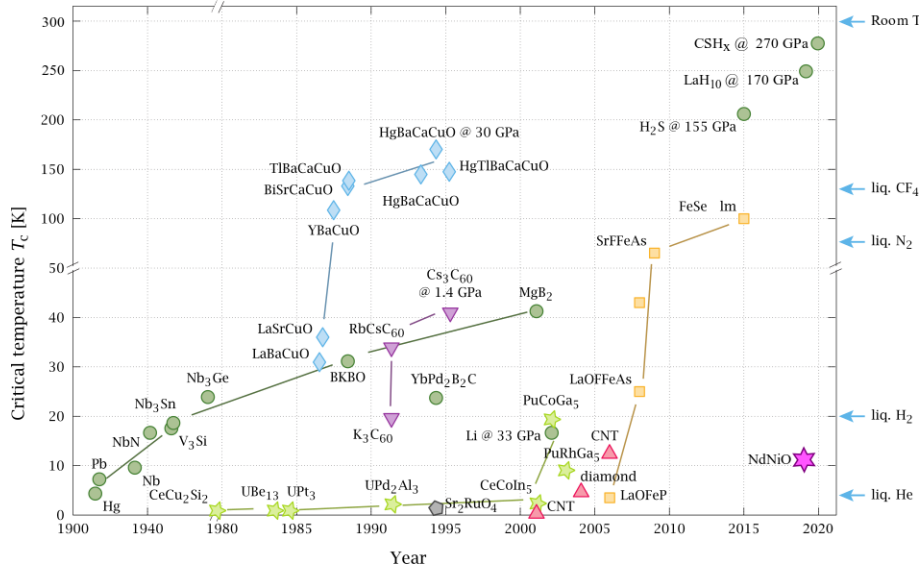
Figure 9: Overview of some superconducting materials from the discovery of the phenomenon until today [46]

The following paragraphs describe some of the most interesting elements, alloys, and compounds for technological applications.

2.1 Low-Temperature Superconductor (LTS)

LTS present a low T_C and are generally easy to manufacture because of their metallic nature. Among them, niobium is extensively used: it can be employed both as an element or as part of an alloy. Another group belonging to the same family are the so-called A15 compounds.

2.1.1 NbTi

Niobium-titanium (NbTi) has a T_C of about 9 K and a $\mu_0 H_{C2}$ that reaches 15 T but is usually limited to 10 T for applications [47][48]. The alloy, discovered in 1962, has been optimized to meet the requirement of the market; for example, it has been found out that to maximize the critical current and other superconducting properties, the optimal content of Ti is between 45 and 50% [49]. NbTi is widely used for superconducting wires, for which many designs have been proposed, as reported in Figure 10. Despite the drawback of the low operating temperature, usually set at 4.2 K, the advantages in employing this alloy are still numerous, especially for cables. It is ductile, cheap to produce, costing below 1 €/kA/m, presents a sizable J_C, up to 3 kA/mm^2 (0.3 MA/cm^2) at 5T, and presents the

possibility to engineer the pinning in the material [51][52][53]. The alloy is chemically stable and the components, both Nb and Ti, are largely available [54].
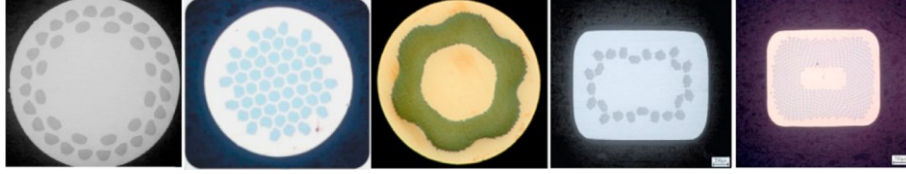
Figure 10: Cross-section of monolith superconducting wires with different filament arrangements [50]

2.1.2 NbN

Niobium Nitride (NbN) is primarily used for electronic devices, particularly for infrared and nanowire single-photon detectors [55][56], but if find applications also as a mixer for high frequencies, alone or combined with other materials such as GaN [57]. For the electronic device, it is grown as thin film and then patterned to maximize the detectivity. It presents a $T_C \approx 16K$, a $\mu_0 H_{C2}$ of 20 T, and a J_C around 10 MA/cm^2 at 4.2 K in 5 T magnetic field [58].

2.1.3 Nb and Josephson junction

Niobium (Nb) is the element that for a long time held the record for the highest T_C, around 9 K, and presents a $\mu_0 H_{C2}$ in the order of 3.5 T [59]. It is generally used in compounds, but it finds applications in superconducting radiofrequency cavities [60] and Josephson Junctions (JJs). For these devices, niobium is used as the superconductor in the superconductor-insulator-superconductor (SIS) junction, where the insulating barrier is usually made of AlO$_x$ [61]. New barriers were recently built in which the insulator is replaced by a metal, creating the so-called superconductor-Normal metal-superconductor (SNS) junction. Nb is also used for nanowire single-photon detectors from the visible to the soft x-ray range [62].

2.1.4 A15 family

The family of the A15 superconductors presents a typical A$_3$B chemical composition, in which A is a transition metal while B has less restrictive requirements. The superconductivity in these materials was discovered in 1954 for the V$_3$Si compound [63]. Since then, the chemical structure, shown in Figure 11a for Nb$_3$Sn, has been extensively investigated, reaching remarkable T_C, up to the value of 23 K for Nb$_3$Ge, which maintained the record for the higher T_C until the discovery of cuprates [64]. Because of their high J_C and $\mu_0 H_{C2}$, and relatively high

T_C, shown in Figure 11b, these compounds are applied primarily for cable and magnets [65].

<div align="center">a)   b)</div>
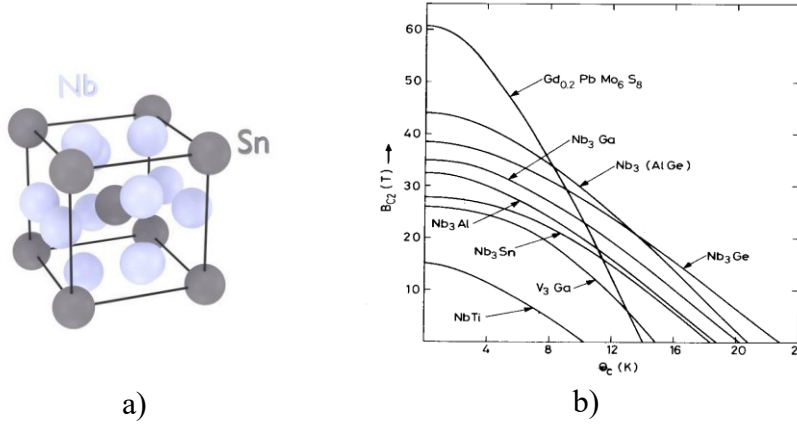
Figure 11: a) Typical structure of A_3B of the A15 compound (Nb_3Sn) b) Summary of the critical field of various A15 superconductors in function of the temperature

Among the different A15 superconductors, Nb_3Sn is one of the most used, especially for wires, because of its better performance than NbTi. Nb_3Sn has a $T_C \sim 18\ K$ and $\mu_0 H_{C2}$ at 0K of 28 T. At the working temperature of Liquid Helium (LHe), Nb_3Sn is employed for magnetic fields between 10 and 20 T [66]. The requirement of various steps in the fabrication process and the associated high cost for the cable, around 10 €/kA/m [67], limits the spread of the alloy in the cable field, still dominated by the NbTi. Despite the high current density and good performance in high fields, the difficulty of manufacturing thin films or nanowires, strongly limits the employment of the A15-type superconductors in the detector field.

2.2 Medium-Temperature Superconductor (MTS)

Discovered in recent years, MTSs include MgB_2 and the iron-based superconductors. They present a transition temperature between Nb_3Ge and the HTS, with a simpler chemical structure and a lower anisotropy.

2.2.1 MgB₂

Superconductivity in MgB_2 was discovered in 2001, obtaining a strong interest from both theoretical and technological points of view [68]. Magnesium diboride is an intermetallic compound, with a T_C of 39 K in bulk and shows a conventional BCS superconductivity with a double gap structure [69]. Many procedures have been developed to fabricate superconducting samples, which found application as bulks, thin-films, and cables [70]. The high interest in MgB_2 cables is due to many

factors: the low density, 2.6 g/cm^3, the absence of critical materials, their low cost, and the capability to fabricate cables with lengths above 10 km. On the other hand, the fabrication process is still tricky and the $\mu_0 H_{C2}$ is relatively low, below 10 T. However, there is a space for improvement thanks to pinning engineering [71]. The relatively high T_C makes MgB$_2$ an appropriate material to replace the LTS, especially for JJs and SQUIDs (Superconducting Quantum Interference Devices). The possibility to fabricate thin-film makes MgB$_2$ suitable for THz electronic, such as mixer and hot-electron bolometers, also because a gain bandwidth larger than NbN-based devices, and nanowire fabrication for single-photon detectors [72].

2.2.2 Iron Based Superconductors (IBS)

The first IBS was discovered in 2006 with a T_C of 4 K but, just two years later, a new compound of the same family showed a T_C of 26 K [73]. Since then, many other compounds with the same Fe$_2$X$_2$ planes have been discovered, setting the highest T_C to 55 K for the 1111 family [74]. IBS are characterized by high B$_{C2}$, relatively high J_C, and low anisotropy, but the presence of toxic elements and lack of experience still limit their applications [75]. As MgB$_2$, many efforts are devoted to developing and optimizing samples that may be employed for cable and tape fabrication thanks to their high H_{C2} ad J_C. Nowadays, IBS are not yet used for technological applications.

2.3 High-Temperature Superconductors (HTS)

HTS have been discovered more than 75 years after the first observation of a superconducting transition. Since then, they have received massive attention for theoretical understanding and industrial applications because of their exotic features. They strongly differ from conventional superconductors and present attractive attributes which make them particularly suitable for technological applications. They have exceptional T_C, higher than LN$_2$, J_C of several MA/cm^2, and upper critical fields several times larger than LTS. On the other hand, high anisotropy, chemical complexity, and poor mechanical properties are the primary deficiencies of these compounds [76][77]. They are widely spread in power applications, such as motors, Superconducting Magnetic Energy Storage (SMES) systems, cables, or magnets, in which their outstanding attributes compared to LTS are substantial advantages, such as better removal of Joule heat and more accessible design of joints [78][79][80][81]. Among cuprates, YBa$_2$Cu$_3$O$_7$ (YBCO) and Bi$_2$Sr$_2$CaCu$_2$O$_8$ (Bi2212) are currently the most studied and employed, especially for the fabrication of cables. HTS also find applications in electronics, in which

weak links due to grain boundaries and the short response time are interesting for SQUIDs and for both emitters and detectors in the THz spectrum [82][83].

2.3.1 BSCCO wires and YBCO coated conductors

HTS are extensively used to manufacture cables; BSCCO and Rare-Earth Barium Copper Oxide (REBCO) are widely spread, particularly the compound Bi2223 ($Bi_2Sr_2Ca_2Cu_3O_X$) and the YBCO, because of the high operating temperature and the low longitudinally stress [84]. They are employed differently: the Bi2223 is used for the first-generation tape (1G), while REBCO for the second generation (2G) coated conductors. They differ in shape and material composition (Figure 12), manufacturing process, and quality [85].
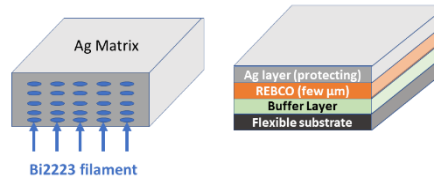
Figure 12: Scheme of 1G Bi2223 and 2G YBCO tape (not in scale)

The fabrication of 1G tape employs the Powder In-Tube (PIT) method using a silver matrix, allowing monocore or multifilament tapes [86]. They have high T_C, higher than 100 K, but limited J_C, lower than Bi2212 one, and length limited to hundreds of meters [87]. The price is high, around 100 €/kA/m, but comparable with other HTS cables [88].

On the other hand, YBCO is manufactured as coated conductor since the PIT technique is not suitable for its fabrication [89]. Despite the initial expectation of low price due to the lower amount of silver, coated conductors are still expensive and can be fabricated for short lengths, below 0.5 km [90]. In addition, they show high J_C, around 2 MA/cm^2 for in-plane direction of the external magnetic field, and good resistance to stresses, if compared with the other HTS cable [91].

HTS cables are employed for power applications in which their excellent critical parameters are significant advantages compared to LTS. Different designs are studied for future transmission lines in both AC and DC, in fusion reactors [92][93], compact SMES and low-weight electrical motors [94][95].

2.4 YBCO films

The peculiar 2D structure of the HTS well adapts to the fabrication of thin films, and therefore, in the last decades, many efforts have been made to optimize deposition techniques and properties of epitaxial films. YBCO films are attractive due to their high crystalline quality, low surface resistance, phase stability, and high flux pinning level. For these reasons, they find applications in coated conductors and electronics. Like other parameters, the coherence length differs if measured in-plane, $\xi_{ab} \approx 1.6\ nm$, and out of plane, $\xi_c \approx 0.3\ nm$. These small values are comparable with the lattice parameters and can be exploited to weaken the superconductivity in the grain boundary and create a "weak-link behavior", useful for JJs and SQUIDs. Other peculiarities are the engineering pinning and the absence of toxic elements.

2.4.1 Crystal structure

All cuprates have a similar crystal structure. They present a quasi-two-dimensional (2D) layer structure containing one or more copper dioxide (CuO_2) planes for unit cells, which are the primary sites for electron conduction. These planes are separated by layers containing a single element that usually acts as a charge reservoir and maintains the structural cohesion and charge neutrality [96].

The crystal unit cell of the YBCO consists of three perovskite cells separated by two CuO_2 planes. The upper and the lower perovskite cells contain a barium atom, while the central one contains an yttrium one. The corner sites are occupied by copper atoms, while the oxygen ones take the middle edge positions. This peculiar structure, shown in Figure 13, gives to the YBCO a strong anisotropy in both superconducting and normal state along the ab-plane (in-plane) and c-plane (out-of-plane). The variation of the oxygen content, described by the "δ" parameter in the chemical formula, is evident in the CuO chain. The addition of oxygen atoms in the chain results in a hole doping in the CuO_2 plane and plays a fundamental role in determining the proprieties and the structure of YBCO. When $\delta=1$, e.g., the material is strongly underdoped, the YBCO cell has a tetragonal structure and acts as an insulator [97]. Varying the oxygen content can bring the YBCO to the superconducting state with a T_C that varies according to stoichiometry. When the superconductor is optimally doped, the b-axis is slightly elongated and the material obtains an orthorhombic crystal structure and the lattice parameters are: $a = 3.82$ Å, $b = 3.89$ Å, and $c = 11.69$ Å, which introduce some additional, but usually negligible, anisotropy in the properties along a- and b-axis [98].
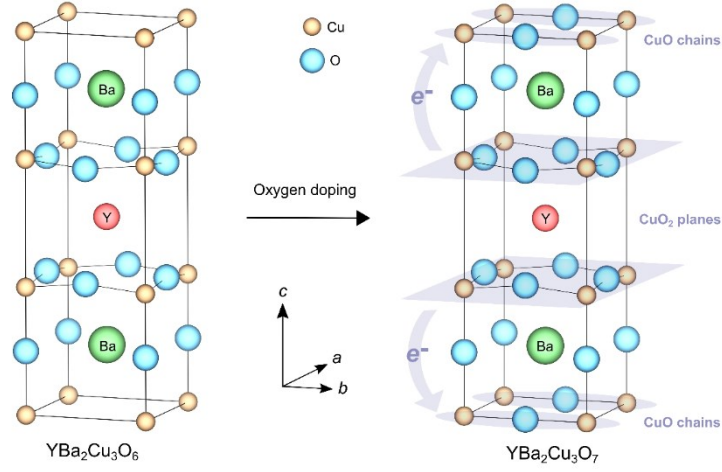
Figure 13: Schematic view of the crystal structure of the YBCO in its tetragonal configuration (left, underdoped) and orthorhombic configuration (right, fully oxygenated)

2.4.2 Phase diagram

In addition to the distinctive geometry, cuprates present a complex phase diagram that varies with temperature and oxygen doping. Although for the scope of this work we will consider only optimally doped YBCO, an overview of the different phases is briefly described below. Figure 14 shows the phase diagram of the YBCO with the main phases: antiferromagnetic, pseudogap, charge density wave, strange metal, Fermi liquid, and superconductivity.

Varying the oxygen content, it is possible to define three main regions: the underdoped, with $p<0.16$, overdoped, when $p>0.16$, and optimally doped, for $p \approx 0.16$ (p represents the hole doping).

The superconducting dome exists from $p=0.05$ to $p=0.27$ and has an inverse parabolic trend, with the maximum around $p=0.16$ and a corresponding $T_C=93\ K$ [99]. The T_C parabolic shape has an imperfection in the underdoped area, around $p=0.12$, where it is strongly suppressed probably because of the competition with the strong charge order present even at low temperatures. The order parameter symmetry in the superconducting state differs from the classical s-wave and has a d-wave ($d_{x^2-y^2}$) symmetry [100] as shown in Figure 15. For this reason, YBCO presents an anisotropic energy gap in the k-space with lobes corresponding to the a and b crystal axes and nodal lines at 45° angles. The poor coupling between CuO_2 planes results in weak superconductivity along the c-axis and a strong anisotropy

in the superconducting properties, with different λ and ξ between in-plane (ab plane) and out-of-plane (c-axis) direction.
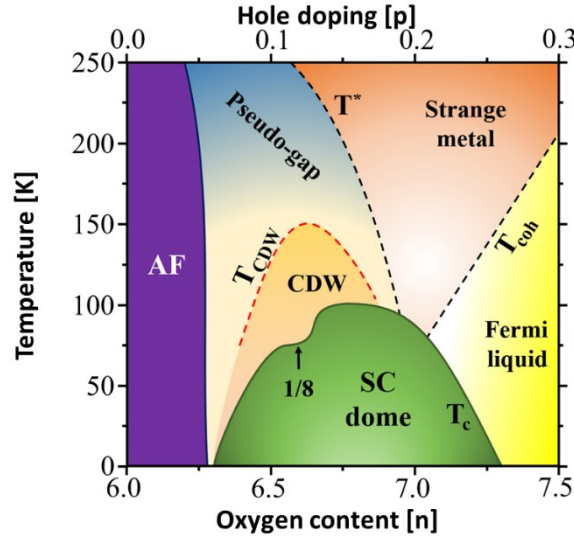
Figure 14: Phase diagram of YBa$_2$Cu$_3$O$_{7-\gamma}$, as a function of hole doping p per planar copper atom and oxygen content n per unit cell
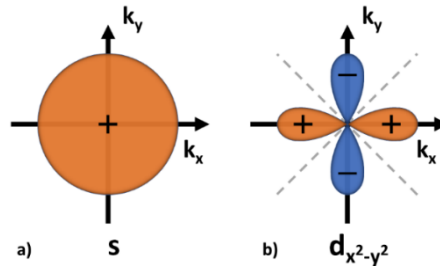
Figure 15: a) Sketch of the pure s-wave order parameter and b) the pure d-wave, $d_{x^2-y^2}$, for YBCO

In addition to the superconducting phase, which is present in a small region of the diagram, six more can be identified:

- Antiferromagnetic (AF): at very low doping, *p<0.05*, YBCO presents AF properties, and it is a Mott insulator [101].
- Pseudo-gap: in the normal state ($T > T_C$), YBCO presents a pseudogap region. Its origin and the connection of this phase with the superconductivity are yet not well understood. It is proposed to either be linked to its precursor, in which case the two phases coexist at low

temperature, or to a competitor, and then the pseudogap is therefore suppressed below T_C [102].

- Charge Density Wave (CDW): in the underdoped regions, this phase is confined between the pseudogap and the superconducting area [103]. The charge modulation is higher at doping *p=0.125*, where the superconductivity is suppressed, and the interaction between those two phases is still under debate [104].
- Strange metal: above T_C in correspondence with the optimally doped region, YBCO presents a linear dependence of the resistance with the temperature (R∝T), extending for hundreds of Kelvins [105]. The trend, which deviates from the metallic one, may be explained by assuming a strangely modified excitation spectrum [106].
- Fermi liquid: the material behaves as a metal with the resistance proportional to T^2.

2.4.3 Films and fabrication processes

Numerous techniques for growing superconducting films have been developed, exploiting both chemical and physical deposition. Each can be divided into the three main steps shown in Figure 16: the creation of the particle, its transport, and its deposition on the substrate.

In thermal co-evaporation, each material is supplied individually, allowing reasonable control in the stoichiometry of the final product. However, rate control and calibration are complicated, mainly because the reactive gas is actively involved in the film fabrication. The particles are extrapolated by heating the source with thermal boats, and the whole process takes place at small pressure. For example, the stoichiometry control for YBCO can reach a precision of 1%, but, for achieving it, the oxygen pressure must be different in the proximity of the substrate from the rest of the chamber [107][108].
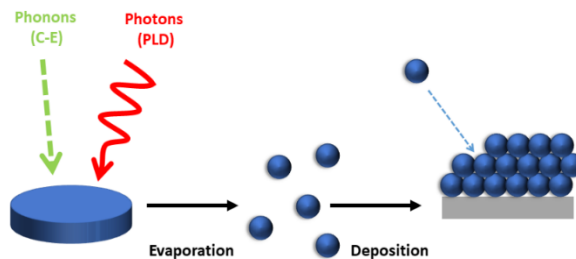
Figure 16: The three steps for a physical deposition

Pulsed Laser Deposition (PLD) is used for a wide range of materials because of its flexibility. A focused laser beam heats the source interacting with free electrons of the material, leading to a local temperature increase and subsequential vaporization. The particle is then transported and deposited on the substrate by means of a plasma plume. In PLD processes, the energy impacting the target is independent by the gas mixture and pressure in the chamber, resulting in high rates, elevated energy densities, and a considerable process flexibility. The main drawback is the common formation of droplets in the sample, usually limited to small areas [109].

Sputtering techniques rely on the discharge of electrons and ions in the atmosphere, and are widely used in industry. It may produce defects due to the high energy of the particle, but the problem is mitigated by increasing the pressure or by particles thermalization. The process is highly reproducible and compatible with oxygen environments, allowing a good deposition of HTS, resulting in good quality films.

Chemical Vapor Deposition (CVD) techniques have the advantage of being cheap, easy to control and scalable, allowing the coating of complex shapes. On the other hand, the growth rate is usually low, and it is difficult to reproduce, mostly because of the stability of the precursor. Metal-Organic Chemical Vapor Deposition (MOCVD) and Chemical Solution Deposition (CSD) have been promising for YBCO, mainly to produce coated conductors [110].

2.4.4 Applications

YBCO films are widely spread, both for tapes (the coated conductors described before) and in cryoelectronic devices such JJs, bolometers, and microwave devices.

In addition to being a valuable tool for studying the properties of superconducting material, JJs are fundamental elements for many devices, such as the SQUID. Because of its extreme sensibility based on magnetic flux quantization, it finds applications in fields such as non-destructive methods, medical diagnostic, and environmental prospecting [111]. In these devices, the YBCO film can be nanostructured, deposited on bi-crystal substrates or with step-edge to create the two required JJs required. Noise Equivalent Power (NEP) below $25 \, fT\sqrt{Hz}$ and modulation voltage around $30 \, \mu V$ have been achieved [112][113] and they can also be used at high temperatures and in large arrays [114]. The great performances at high frequency make YBCO films suitable for Superconducting Quantum

Interference Filters (SQIFs), microwave filters and resonators where the high-quality factor is essential for technological applications and fundamental studies [115][116][117].

YBCO thin films are largely employed also as detectors and mixers, mainly in the THz domain, as detailed in the next chapter. Indeed, YBCO microbolometer detectors show very short response times, in the order of picosecond, with good responsivities, which reach values over 500 V/W also in the THz range [118][119], thanks to the non-thermal response of the superconductor. YBCO JJs coupled with antennas are used as mixers, working at relatively high temperatures with a low pumping power in the order of μW [120][121]. YBCO film devices working as Transition Edge Bolometer (TEB) are used to enhance the coupling with polarized radiation [122] and capture thermal images even at high temperatures [123].

2.4.5 YBCO based detectors

After the discovery of high-temperature superconductors and with the progressive mastering of their manufacturing, YBCO-based TEBs have been acquiring more and more interest in the scientific community [124]. It is mostly because the opportunity to work at a relatively high temperature provides a good trade-off between simplicity and performance. One of the first results is reported in [125] where a YBCO film is deposited over $SrTiO_3$, a substrate which a thermal conductivity around $10\ W/(m \cdot K)$. It results in a very fast bolometer, $\tau \approx 20\ ns$, but limited responsivity and a working temperature well below the LN2. A similar device is proposed in [126]: a YBCO-based microbridge reaches very high responsivity, in the order of 4 kV/W, to the detriment of the time constant, in the order of 0.5 ms. Already these first examples highlight that it is necessary to find a compromise between a fast and a responsive bolometer. This is partially done in [127], where a microbridge and a meander configurations are studied on a $SrTiO_3$ substrate. The first provides a fast response and the second a high responsivity, in the order of 1.6 kV/W. Yttria stabilized zirconia (YSZ) has been extensively used as a substrate for its low thermal conductivity, which allows a high responsivity, and its good match with the YBCO. Responsivities obtained using this substrate are relatively high, from tens to hundreds of Volts per Watt for microbridges detectors. However, due to the intrinsic low thermal conductivity, these devices have a time constant not below tens of microseconds [128][129]. Meander devices, such as reported in [130], have a very high responsivity, up to 4 kV/W for an $I_B = 100\ \mu A$, with a time constant incredibly long, in the order of seconds, $\tau = 25\ s$. YBCO films grown on MgO substrate are investigated in [131][132], where the author was

focusing on the phase response in the frequency domain, and in [133], where the studied device shows a responsivity of 14 V/W and the response time of 20 ns. A comparison between two substrates is carried out in [128]. The device grown on MgO substrate, compared with the YSZ one, shows slightly higher responsivity, 69 V/W, but a noise 100 times bigger. On MgO are also grown highly oriented thin films manufactured as meander, with a responsivity of 10 V/W and a response time of 3,3 s [134], or microbridge with responsivity up to 17 kV/W [135]. Some YBCO-based TEBs are reported in Table 1 for different substrates and sensing elements.

Recently, coupling between microbridges and antennas has been considered in the bolometer design. It optimizes the interaction between the incoming radiation and the material, improving the detection of the signal [136]. In [137], the microbridge was fabricated on YSZ substrate and it presents a response time $\tau \approx 20\ \mu s$ and a responsivity of almost 500 V/W. Better performances are obtained with a substrate made of LaAlO$_3$, [138], where different samples are tested. They have a time constant of $\tau \approx 0.3\ \mu s$ and responsivity up to hundreds of V/W. A further improvement is obtained on an Al$_2$O$_3$ substrate; this detector reaches a similar responsivity, 400 V/W, and a time constant of 20 ns [139]. An even faster device is grown over a sapphire substrate [140], where the responsivity is reported to be 190 V/W, also thanks to an elliptical silicon lens, and the time constant is reduced to 300 ps.

Other devices, which strongly differ from the one presented in this study, are the membrane bolometers. The structures of these detectors, superconductor and substrate, are suspended from the main device to minimize the thermal conductivity and maximize the responsivity. It can be done with conductive wired, as in [141] or through micromachined silicon, as done for the first time in [142].

Table 1: List of YBCO based TEBs

Sensing element	Substrate	Time constant	Responsivity [V/W]	NEP $[W \cdot Hz^{0.5}]$	Ref.
Bare YBCO	SrTO$_3$	20 ns	<<1	10^{-6}	[125]
Microbridge	SrTO$_3$	0.5 ms	4000	$2.5 \cdot 10^{-6}$	[126]
Microbridge	SrTO$_3$	15 ms	250		[127]
Meander	SrTO$_3$	16 s	800	$5 \cdot 10^{-9}$	[127]
Meander	YSZ	1 ms	60	$6 \cdot 10^{-10}$	[128]
Meander	MgO		69	$2 \cdot 10^{-8}$	[128]
Microbridge	YSZ	10 µs	975	$2 \cdot 10^{-12}$	[129]
Meander	YSZ	25 s	5000		[130]
Microbridge	MgO	20 ns	14	$1.2 \cdot 10^{-10}$	[133]
Meander	MgO	3.3 s	10		[134]
Microbridge	MgO		17000	$2.1 \cdot 10^{-14}$	[135]

Another kind of detector vastly used in the infrared range is the hot-electron bolometer (HEB). YBCO-based HEBs are used as a mixer for their fast response and elevated working temperature. A thin superconductive layer is deposited on the substrate, which may vary depending on the device characteristics. Different groups present their work with MgO substrate. In [143][144], different devices are presented with a responsivity which varies from 0.5 to 0.75 V/W. The main difference is the introduction of a logarithmic antenna. Better results are obtained in [145][146], in which the responsivity reaches values from 150 to 780 V/W depending on the LO power powered with a 50 Ω coplanar line feeding a double slot antenna. The use of multilayer HEB is presented in [147], where a very thin film of YBCO is achieved over a MgO substrate thanks to c-axis oriented

$PrBa_2Cu_3O_{7-\delta}$, showing a degradation of the film when the dimension goes below the micrometre. A simple design was used in [148][149], where an antenna is created with a constriction to match the impedance and focus the incoming signal, similarly as described in the following chapter. In [149], a spiral antenna is used for a YBC film grown on a $LaAlO_3$ substate, with a gain of 46 dB. All the devices presented above rely on the fast YBCO thermalization, therefore, they present response times below 3 ns.

In addition to the YBCO based HEB, several other superconductors has been employed for the creation of such devices, as NbN [150], Nb [151] and MgB_2 [152], and different design, such as with spiral antenna [153], bow tie [154] and logarithmic one [155].

3. The THz gap

3.1 Terahertz radiation

The Terahertz (THz) radiation occupies a small part of the electromagnetic spectrum, which includes frequencies from 0.3 THz to 3 THz. Its wavelength varies from 100 μm to 1 mm and its energy from 1.2 meV to 12.4 meV, as reported in Figure 17. Part of the THz range overlaps with the infrared region, particularly the far-infrared (FIR), which ranges from 0.3 to 20 THz.

Nowadays, there is still a lack of appropriate technologies for exploiting the full potential of THz radiation. Indeed, it is so far true the expression "Terahertz gap", which refers to the mismatch between the improved technologies developed in microelectronic and photonics compared to those concerning the Terahertz region [156][157]. This gap may also be filled thanks to superconducting devices, which show promising performance both as sources and detectors [158][159].
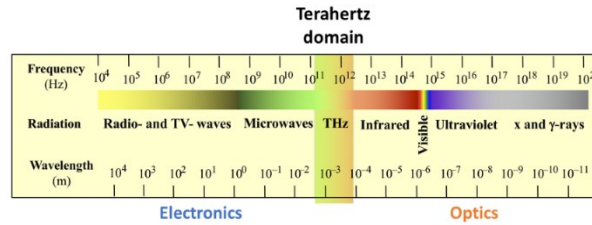
Figure 17: Range of frequency and wavelength of the THz range in the electromagnetic spectrum.

In 2017, the European THz Roadmap put quite an emphasis on the THz region, which was defined as the most important part of the electromagnetic spectrum for science and technology in terms of multidisciplinary use [160]. Much effort has been made since then for the scientific development of novel instrumentations [161].

The interest in the THz range region comes from the numerous advantages compared with higher and lower frequencies, which makes it suitable for several applications, as shown in Figure 18. The energy carried by the radiation is well below the ionizing one, set at 14 eV, and is therefore biologically safe for human

treatment and medical imaging [162][163]. The THz spectrum is a natural supporter of 5G in communication and data transmission because of the high bandwidth and high-speed transmission [164][165]. THz detectors are also extensively used in the astronomy investigation because of the large amount of information in the FIR spectrum and are already widely studied and optimized [166][167]. Another advantage of these frequencies is the good transmission coefficient through materials such as tissue, biological or not, glass, and paper. That makes them very useful in the security area, where THz radiation is already implemented for detecting explosive materials and body scan [168][169], but also for nondestructive testing, to investigate coating and composite material with high resolution [170]. The high absorbance of the THz radiation by organic compounds is used for investigation in the food chain, from agriculture to processing, such in chemical and pharmaceutical industries where is essential to resolute the quantity and quality of impurities [171][172][173].
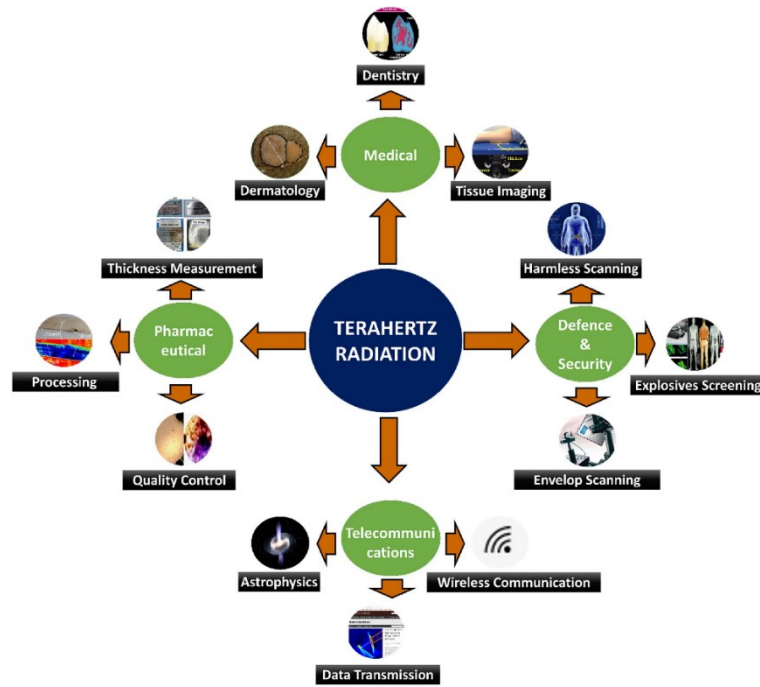
Figure 18: Some applications of the THz radiation [174]

3.2 Infrared detectors

THz detectors have been studied and developed for many decades. The technological advantage allows exploiting more sophisticated physical phenomena to detect the incoming radiation and continue to improve the detector performances,

such as response time, noise or responsivity. Depending on the physical principle at their base, the detector can be classified as a quantum (or photon) detector, a rectification detector, or a thermal detector [175].

Detectors are divided into two big categories: incoherent, or direct, and coherent detectors [177]. Direct detectors detect only the signal amplitude losing the information on the phase. The active component absorbs the incoming signal, which modifies its properties through an electronic excitation or a rectification process or absorption of thermal energy. They usually have a large band, a simpler structure, and allow developing large arrays. On the other hand, coherent heterodyne detectors can resolve both the intensity and the phase of the signal. However, they require a mixer and a local oscillator, increasing the complexity of the detection system; this instrumentation grants down converting the incoming signal to the GHz band, but this corresponds to the detriment of the band resolution and to an increasing of the time constant [178].

Detectors can also be categorized depending on which mechanism is affected by the incoming radiation. The family with the most straightforward principle includes the "thermal" detectors, firs developed ones, in which the incoming signal heats the material and changes its physical properties. They include devices working at room temperature such as Golay cells, pyroelectric devices, and neon tubes, with show low response times (second, millisecond and microsecond respectively) and small detectivities due to the noise associated with the high operating temperature [179][180][181]. Other thermal detectors are the thermocouples, with response times that can reach hundreds of ns [182], and bolometers. The last ones can be made of metals, superconductors, semiconductors, and insulators, with a relatively low response time, of the order of µs, and noise and responsivity, which are connected with the working temperature [183]. Superconductor bolometers require to work at low temperatures while semiconductor ones may also work at room temperature. The firsts have a sharp variation in resistivity in correspondence of the transition temperature while the seconds exploit the exponential decrease of the resistance with temperature due to the promotion of carriers. Both kinds of bolometer can achieve low noise, in the order of tens of $pW/Hz^{0.5}$, and high responsivity, which can vary from a few to thousands of volt per watt [184]. Finally, kinetic inductance detectors have been largely studied, recently, because of their low noise and the capability to be fabricated in arrays [185].

THz radiation can impact the electronic bands to create a collective motion or transition from different states. The first mechanism is at the base of plasmonic detectors, which present fast and significant responses in the order of kV/W [186]. They include a Field-Effect Transistor (FET) made in GaN or graphene, and devices that exploit surface plasmons excitation for incoherent detection [187]. The electronic transition due to the THz radiation is at the bases of devices such as superconductor-insulator-superconductor (SIS) junctions, Schottky barrier diodes, photodetectors, and more recently quantum well and quantum dot detectors. Semiconductor devices have the advantages of working at room temperature and being extremely fast, but, like quantum-based devices, are limited by the band structure, and therefore the bandwidth is often limited [188]. SIS detectors are based on the JJs; they need to work at low temperatures and have the frequency range limited by the energy gap, which is usually higher when HTS are employed, and show large responsivity [189].

3.3 The INFN-TERA Project

The INFN-TERA project ("High field Terahertz Era") [190], founded by the INF CALL 2017, was running from 1/1/2018 to 31/12/2021. It consisted of four work packages, connected between them:

1. The development of a source able to emit intense sub-ps single-cycle coherent THz pulses in the region 0.3-20 THz, with a repetition rate up to 3 kHz and at a high associated electric field (up to 50 MV/cm).
2. The design of novel geometries for THz radiation guideline, for optimizing particles acceleration and investigating electron beam dynamics for different cavities and THz fields [191].
3. The development of a bolometric detector, which can operate at high temperature, above LN_2, with a short response time, in the order of ps, and high dynamic range [192].
4. The development of an efficient device to control and manipulate THz radiation, with a particular attention to its phase and polarization [193].

Among these deliverables, the unit of Politecnico di Torino was responsible of the third one, aiming at optimizing an already fabricated detector and, at the same time, at designing a more efficient one. The new detector will work in the same range of temperature and frequencies but will show a faster response to meet the criterium set by the project. The work of this thesis is mainly framed within the INFN-TERA project.

3.4 Transition edge bolometer

A bolometer is a detector that converts the incoming power of an incident electromagnetic radiation into an electric signal [194]. It is included in the family of the direct detectors. Only the signal amplitude is detected, losing information regarding the radiation phase [195].

The working principle is straightforward: the device directly absorbs the incident radiation, increases its temperature and changes the conductivity. This last variation is associated with a measurable output signal (current or voltage). Choosing the suitable materials is crucial for a bolometer; a strong dependence of the electrical resistivity with the temperature near the working point is essential for achieving good performances. Bolometers can be made of semiconductors, metals, or superconductors [196], each of which has a different RvsT curve, as schematically shown in Figure 19.
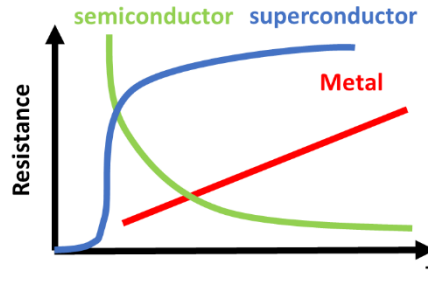
Figure 19: Evolution of the resistance with the temperature for various materials

The resistance variation can be expressed with the temperature coefficient of resistance (TCR) α defined in (3.1), where R is the resistance at the working temperature and dR/dT is the derivative.

$$\alpha = \frac{1}{R}\left(\frac{dR}{dT}\right) \qquad\qquad 3.1$$

Like the resistance, the parameter α varies linearly in metallic materials, exponentially in semiconductors, and highly non-linearly in superconductors.

A schematic view of a bolometer is shown in Figure 20, which represents the incoming signal, the absorber, the thermal link, and the thermal reservoir. The absorber, which has a heat capacity of C, is kept at a constant temperature T_B by

means of a thermometer. When an external radiation heats the absorber, it cools down through a thermal conductance G, which connects the absorber to the heat sink at the set temperature T_S.
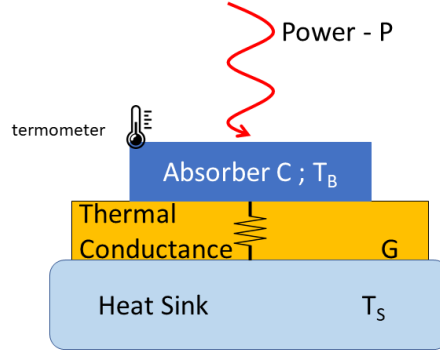
Figure 20: Main component of the bolometer

To maximize the performance of the device, the absorber must present high absorbance in the frequency range of interest and the temperature variation must be limited to a fraction of the operating one.
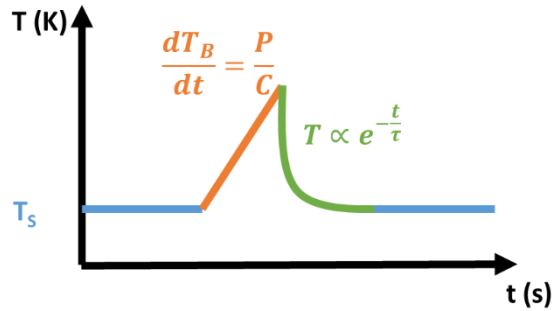
Figure 21: Temperature evolution of a bolometer when a signal is detected

The temperature evolution in a bolometer is schematically represented in Figure 21. This evolution follows the equation (3.2) where C is the absorber heat capacity, $\frac{dT_b}{dt}$ the temperature variation of the bolometer, G the thermal conductance, T_B the temperature of the bolometer, and T_S the heat sink temperature. On the other side, $P(t)$ is the power deposited by the incoming radiation, which causes an increase in the temperature. However, the equation (3.2) is valid only for small temperature variation, therefore $(T - T_S) << T_S$ must be satisfied.

$$C \left(\frac{dT_B}{dt}\right) + G(T_B - T_S) = P(t) \qquad\qquad 3.2$$

In Figure 21, is it possible to identify three different areas according to the temperature evolution:

- Before and long after the signal: the temperature is stable, and the overall power is constant and balanced by the cold finger. It includes Joule heating, ambient radiation and more.
- The signal reaches the bolometer: the temperature increases proportionally to the incoming energy at a rate linked to the power and heat capacity (3.3). The variation in temperature affects the device resistance (3.4), which can be detected as a change in the voltage (3.5). In the equations, ΔE is the total energy deposited by the incoming radiation, R_0 the bolometer's initial resistance, and R_f the resistance reached by the device. V and I are the voltage drop across the bolometer and the bias current.

$$\frac{dT_B}{dt} = \frac{P}{C} \rightarrow T_B = \frac{\Delta E}{C} \qquad\qquad 3.3$$

$$R_f = R_0 \cdot (1 + \alpha\Delta T_B) \rightarrow \Delta R = R_f - R_0 = \alpha\Delta T_B \qquad\qquad 3.4$$

$$V = R \cdot I \rightarrow \Delta V = \Delta R \cdot I \qquad\qquad 3.5$$

- Just after the signal: the bolometer is no longer irradiated, and the temperature returns to the steady one following (3.6) and (3.7). The ratio τ (3.8) is the bolometer response time and determines how fast the bolometer can relax to its equilibrium state.

$$C \left(\frac{dT_B}{dt}\right) + G(T - T_S) = 0 \qquad\qquad 3.6$$

$$T_B(t) = T_S + \frac{P}{G} e^{-\frac{t}{\tau}} \qquad\qquad 3.7$$

$$\tau = \frac{C}{G} \qquad\qquad 3.8$$

The performances of the bolometer are therefore strongly affected by the parameters C, G, and α. A small heat capacity results in a considerable variation in temperature and a fast response time. Similarly, a sizeable thermal conductance allows the device to relax rapidly to the initial temperature, but it affects the response of the bolometer. Finally, a large α results in a significant variation in resistance and, therefore, a great response to the external signal.

3.4.1 Responsivity

The responsivity is defined as the ratio between the detected voltage and the incoming power (3.9). Depending on the device, it can be expressed in ampere or volt per watt. For this study, it is expressed as V/W since the output quantity is a voltage drop.

$$r = \frac{Detected\ voltage}{incoming\ power} = \frac{\Delta V}{\Delta P}\left[\frac{V}{W}\right] \qquad 3.9$$

When the bolometer is used as a direct detector and the relation between the modulation frequency and the time constant is fulfilled (3.10), then the equation (3.2) can be expressed as (3.11). It considers both the power dissipated by the Joule heating in the resistance due to the bias current, I_{BIAS}, and the external radiation, P_{ext}.

$$\omega \ll 1/\tau \qquad 3.10$$

$$(T_B - T_S) = P(t) = I_{BIAS}^2 \cdot (\Delta R) + P_{ext} \qquad 3.11$$

From (3.11) it is possible to obtain the responsivity of the bolometer (3.12) as extensively treated in [197] and [198], which includes μ, the absorption coefficient of the material at the working frequency.

$$r = \frac{\mu\frac{dR}{dT}I_{BIAS}}{G - \frac{dR}{dT}I_{BIAS}^2} = \frac{\mu \cdot I_{BIAS} \cdot \alpha \cdot R}{G - I_{BIAS}^2 \cdot \alpha \cdot R} \qquad 3.12$$

If the relation (3.10) is not valid, the responsivity can be expressed as (3.13) [199].

$$r(\omega) = \frac{r_{(\omega=0)}}{1+i\omega\tau}$$ 3.13

The resistance R is the only parameter that varies considerably with the temperature in the resistivity equation since its variation is the basic principle of the bolometer. The other parameters, such as thermal conductivity and, indirectly, the time constant, are considered constant both with temperature and frequency. Moreover, a current driven bolometer has two other properties linked with the current and its supplier. The generator suppling the bias current has such a big input resistance that can be considered infinite with the respect of the bolometer circuit, and therefore it does not affect the bolometer response. Finally, the bias current is maintained low enough to consider the thermal and electrical time constant equal.

3.4.2 Noise

The noise is a random fluctuation present in every measurement. The sensibility of a detector can be expressed in terms of Noise Equivalent Power (NEP) which has different sources. The NEP is defined as the power required to produce a signal-to-noise ratio (S/N) equal to one at the device output at a certain modulation frequency and effective noise bandwidth. It is expressed in $W/Hz^{0.5}$. The S/N ratio improves linearly with the square root of the integration time, and thus, integrating for a long time, it is possible to reduce the NEP. The main noise contributions in a bolometer are the Johnson noise, the phonon noise, the photon noise, and the low-frequency noise [200][201].

The Johnson noise, also called thermal or Nyquist noise, is correlated to the random thermal motion of the charge carriers, usually electrons, inside the material at the thermal equilibrium. It is directly proportional to the resistance (R) and the temperature (T) but inversely proportional to the square of the responsivity (r) (3.14).

$$NEP_J^2 = \frac{4k_BTR}{r^2}$$ 3.14

The phonon noise, or thermal noise, is linked to the temperature variation of the detector due to thermal fluctuations caused by quantized carried of energy from the bolometer to the heat sink through the thermal conductance G (3.15).

$$NEP_t^2 = 4k_bT^2G$$ 3.15

The photon noise is due to an intrinsic variation of the photon flux reaching the detector. It is particularly important when the other noise sources are close to zero, e.g., at very low temperatures and with almost null electrical resistance. It can be expressed as (3.16), in which Q is the radiant power absorbed, ν the average frequency and μ is the absorbance of the material.

$$NEP_{ph}^2 = 2Q(h\nu + \mu\epsilon k_b T)$$ 3.16

The low-frequency noise, or flicker noise, includes the noise sources correlated to impurities, traps, and the resistance fluctuation. These imperfection results in voltage fluctuation when current is fed, especially noticeable at low frequency at which it is predominant with respect to the white and thermal noise. It is analytically impossible to evaluate because of the numerous sources of which it is composed, so experimental measurements are needed for its estimation. It depends inversely on the frequency, and for this reason, it is also called 1/f noise. The parameters k_f and γ, usually close to one, depend on the device and affect the NEP as reported in 3.17.

$$NEP_{1/f}^2 = \frac{k_f V^2 \cdot f^{-\gamma}}{r^2}$$ 3.17

The total noise, calculated for 1 Hz, is the square sum of the various contributors. Depending on the working condition, such as temperature and resistance for example, some contributions may be more important than others, which can then be neglected (3.18).

$$NEP^2 = NEP_J^2 + NEP_t^2 + NEP_{ph}^2 + NEP_{1/f}^2$$ 3.18

It is possible to express the NEP in a quantity that can be easily compared with the output signal from $W/Hz^{0.5}$ to V using the eq (3.19), considering 1 Hz of bandwidth. Here only the dominant noise terms are reported, in order, the Johnson, the thermal, and the flicker noise, represented as $\langle V_F \rangle$ [202].

$$\langle V_N \rangle = \sqrt{4k_b TR} + \frac{\sqrt{4k_b T^2 G}}{Rw} + \langle V_F \rangle [V]$$ 3.19

3.4.3 Detectivity

The detectivity is the inverse of the NEP (3.18), indicated with D (3.20). To consider the area of the detector, A_d, and the bandwidth, Δf, it is necessary to define a new quantity: the normalized detectivity D^* (3.21). It allows to easily compare various detectors, even if they are different in size and materials.

$$D = \frac{1}{NEP} \qquad\qquad 3.20$$

$$D^* = \frac{\sqrt{A_d \cdot \Delta f}}{NEP} \qquad\qquad 3.21$$

3.4.4 Time constant

Another critical parameter for evaluating the bolometer performance is the time constant. It defines the temperature decay in the device: a short time constant is linked to the capability to react faster to external signals. Indeed, the time constant is the time required for the temperature to decrease to *1/e* of its value when thermal radiation is instantaneously removed. It is proportional to the thermal capacity, defined as *C*, and inversely proportional to the thermal conductivity between the absorber and the heat sink, defined as *G*, as shown in (3.22).

$$\tau = \frac{C}{G} \qquad\qquad 3.22$$

Unfortunately, the time constant must compromise with the other quantities, particularly the responsivity. Indeed, as shown before, a small *G* grants a large responsivity, while a small one a short time constant. It is, therefore, necessary to find a value appropriate to the need of the detector.

4. YBCO based transition-edge bolometer

In the framework of the INFN-TERA project, an YBCO based Transition Edge Bolometer (TEB) has been developed and optimized for working at a temperature higher than LN_2 in a portable cryostat. To achieve better performances, the material had undergone irradiation through high-energy heavy-ions (HEHI). This process varies the RvsT curve tuning the T_C. After the characterization, the whole device has been simulated and optimized using the finite element method (FEM) using the software COMSOL Multiphysics$^®$ both in stationary and transient conditions as reported in chapter 5.

4.1 Device description

4.1.1 Deposition process

The active part of the bolometer under study is an YBCO film deposited over an MgO substrate purchased by Theva Dünnschichttechnik GmbH (THEVA). The detector is obtained with an opportune patterning and subsequential HEHI irradiation of the sample. The thickness of the film is 250 nm, a value near to the maximum critical current density for the YBCO [203], and grants a considerable resistance across the patterned layout. The superconductor is optimally doped, with a T_C higher than 89 K as expected from the phase diagram. Moreover, it does not present cracks or imperfections on the surface, which may impact the manufacturing and the quality of the final device [204]. The YBCO film is deposited by thermal co-evaporation over a 0.5 mm thick MgO substrate with lateral dimensions of 10 mm x 10 mm. This procedure shows a fast growth rate, typical of the PLD and MO-CVD techniques, with the possibility to deposit the superconductor over larger sample areas without imperfections [205].

Among the different substrates such as MgO, $SrTiO_3$ (STO), $LaAlO_3$ (LAO), YSZ, the decision of using the MgO is made considering mechanical, electrical, and thermal reasons. The cubic symmetry of the 001 oriented MgO allows a good epitaxial growth of the YBCO film [206]. The lattice mismatch, calculated as in (4.1), where the in-plane lattice parameters of the MgO and the YBCO are

respectively α_{MgO} and α_{YBCO}, is around 9%, larger than the other substrates ($\delta_{\text{LAO}}^{\text{m}} \approx 0.7\%$ and $\delta_{\text{STO}}^{\text{m}} \approx 2.2\%$), but still reasonably low for growing a good quality film [207][208].

$$\delta^m = \frac{a_{Mgo} - a_{YBCO}}{a_{MgO}} \qquad\qquad 4.1$$

The slight disadvantage due to the crystal mismatching is compensated by the good thermal and electrical properties of the MgO. It is characterized by a low dielectric constant, $\epsilon_r < 10$, and noticeably low microwave losses, with a loss tangent $tan\delta \approx 10^{-5}$ at 90 K and 10 GHz [209]. It also makes MgO suitable for high-frequency applications, such as GHz superconducting resonator [210], and for fast readout, essential for analyzing short signals or pulse trains with small time intervals between pulses. The performances at such frequencies allow defining signal efficiently even with sub microsecond variations, which can be detected by the YBCO device. The MgO thermal expansion coefficient at room temperature is similar to the YBCO one, $\alpha_{MgO} \approx 10^{-5} K^{-1}$ and $\alpha_{YBCO} \approx 1.34 \cdot 10^{-5} K^{-1}$ [211][212], resulting in negligible amount of stress or strain for multiple cooling and heating of the devices. Finally, the high thermal conductance at low temperatures [213] grants an intrinsic short response time of the device, which, combined with the small losses at high frequencies previously mentioned, strengthen the decision of this material as the substrate for a bolometer with a fast response.

4.1.2 Patterning

The pattern was realized with standard photolithography in which the superconducting material is removed through a wet chemical etching. The precision obtained with this procedure is in the order of the μm [214]. The main limit of this procedure is the unpredictability of the over-etching linked with the chemical attack. For this reason, the mask was slightly over-dimensioned. This allowed to completely remove the YBCO film without damaging the structure defined with the optical technique. The procedure, performed at Politecnico di Torino, is briefly described below:

1. A small amount of "AZ5214e" resist covers the sample, then placed on a spinner. It rotates at 4000 rpm for 30 seconds, after which the resist layer reaches a thickness of about 1.4 μm.

2. The mask is placed on the sample with the printed side in contact with the resist to reduce the shadow and increase the lithography resolution. Then it is irradiated with a 350 W mercury lamp for 30 seconds. The wavelength of the radiation which hardens the resist is 365 nm and the total energy deposited during the process is about 25 mJ.
3. The resist is developed in a solution H2O:KOH (3:1 ratio) for 60 seconds. Then, it is hardened by soft backing for one minute.
4. The YBCO is removed by wet etching with an HCl solution below 0.1% vol. The remaining resist is taken away with acetone.
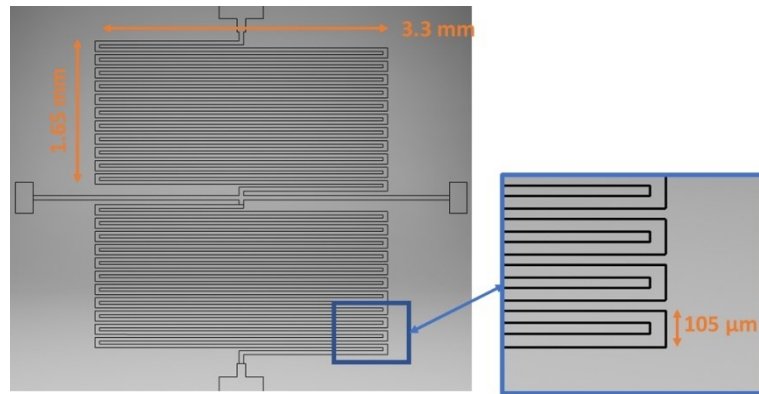
Figure 22: CAD of the mask used for the patterning process

The pattern (Figure 22) presents two identical meanders. Each one is composed of a strip 35 μm in width and 75 mm long. The distance between the strip is the same as the meander, 35 μm, and the lateral sides of the serpentine are 1.65 mm x 3.3 mm. Two pads are provided in order to pick-up a voltage drop across each meander through a differential measurement.

4.1.3 Irradiation process

The sample was irradiated with HEHI at the Laboratori Nazionali di Legnaro (INFN-LNL). Only one meander underwent irradiation with 114 MeV Au$^+$ ions with a fluence of 4.84 10^{11} cm^{-2}, equivalent to a matching field of 10 Tesla, while the other was covered with a 200 μm stainless steel foil for screening the particles. A slight difference is detectable in the height of the meander, the irradiated area is slightly higher, but the appearance remains almost unaltered, as visible in Figure 23 [215].

The custom line at LNL shares a Tandem-XTU type which accelerates Au ions in the oxidation state +15 with an energy of 7.6 MV and collimates the high-energy heavy ions (HEHI) beam to obtain a lateral aperture from 30 to 300 µm.
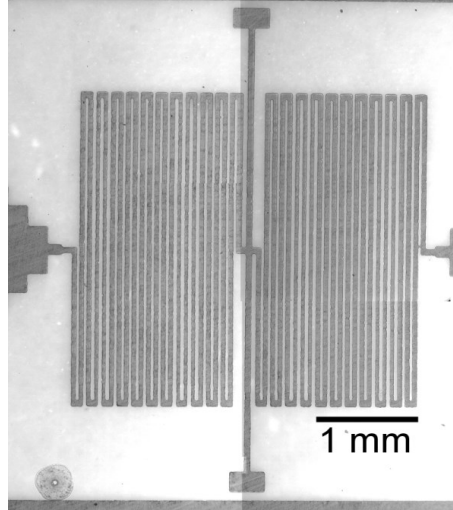
Figure 23: An optical image of the bolometer after the irradiation process

The irradiation with 114 MeV Au$^+$ ions aims to create columnar defects in the YBCO limiting point defects such as vacancies or small cascades. Indeed, the energy released by inelastic scattering with heavy ions is usually associated with columnar defects. The energy threshold for the YBCO to have this kind of defect is around 20 MeV/µm, a level that is amply reached with this process, as shown in Figure 24. The energy released in the YBCO by the inelastic scattering is around 25 MeV/(µm ion) compared with only 0.2 MeV/(µm ion) of the elastic process; this difference promotes Coulomb explosions in the material, which results in columnar defects of about 5 nm of diameter and amorphization in a larger area in which is expected a local reordering of oxygen [216][217].
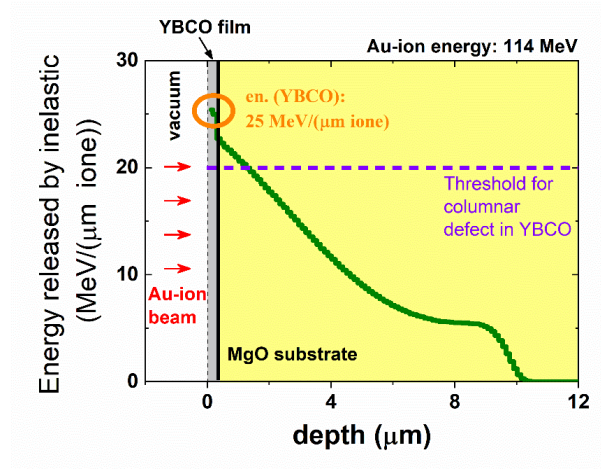
Figure 24: Energy released by inelastic scattering in the sample
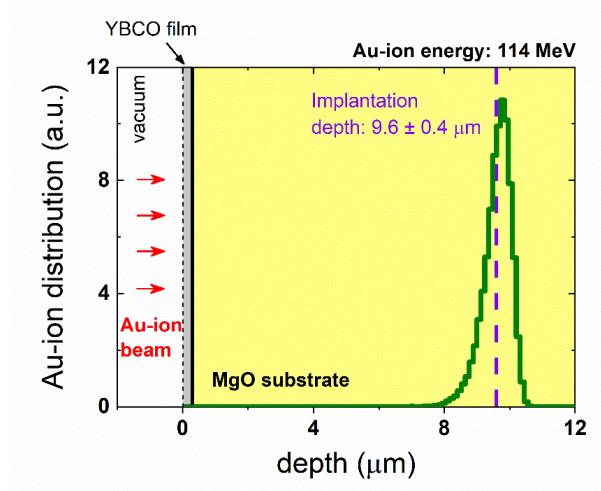
Figure 25: Implantation depth of the Au+ ions. In correspondence with the peak, also the dpa and the energy released by elastic scattering have their maximum

Due to their high energy, the ions pass through the YBCO film got implanted in the substrate at a depth of around 9.6 µm, as shown in Figure 25. At this depth, the energy deposition by elastic scattering exhibits its peak, around 1.2 MeV/(µm ion), such as the overall dpa in the substrate around 10^{-3} for a fluence of $4.84 \cdot 10^{11} cm^{-2}$. The dpa in the YBCO film is around $0.2 \cdot 10^{-4}$ [218]. The changes induced in the substrate is the main cause of the modulation of the superconducting properties, in particular of the strong reduction of T_C and J_C (with HEHI irradiation at the same fluence of bulk YBCO one should expect a much lower reduction of T_C and an enhancement of J_C).

In fact, the irradiated meander shows a substantial difference in the T_C and RvsT curve, for both the resistivity values and its slope across the transition temperature [219], as well as a higher absorbance in the THz spectrum [220]. The other meander, which remains in the as-grown state, does not differ in any properties. This meander stays in the fully superconducting state in the whole transition area of the irradiated one, allowing to correct the electro-thermal effect without impacting the voltage drop and the power dissipation.

The device was measured in the four contacts mode with a generator Keithley current source 224 and a Keithley Nanovoltmeter 2182, in the cryostat filled with LN$_2$. The pristine part has a $T_C=88$ K, while in the irradiated part it is reduced to *83.5 K*. This high disparity gives a wide choice for the working temperature: the difference between the two T_C is larger than the useful range of temperature for employing the film as a bolometer, i.e., the transition area. Moreover, the different T_C allows making a position-dependent detector. The most crucial variation is RvsT first derivative, which has been enhanced by the irradiation process, increasing from 6.0 $k\Omega/K$ to 8.0 $k\Omega/K$ as shown in Figure 26 and Figure 27. Some other advantages of reducing the T_C are the possibility of working at lower temperatures decreasing the heating power required to compensate for the LN$_2$ cooling power and reducing both the thermal noise and the Johnson one (3.14 and 3.15). A larger derivative of the RvsT curve is associated with a higher responsivity of the detector.
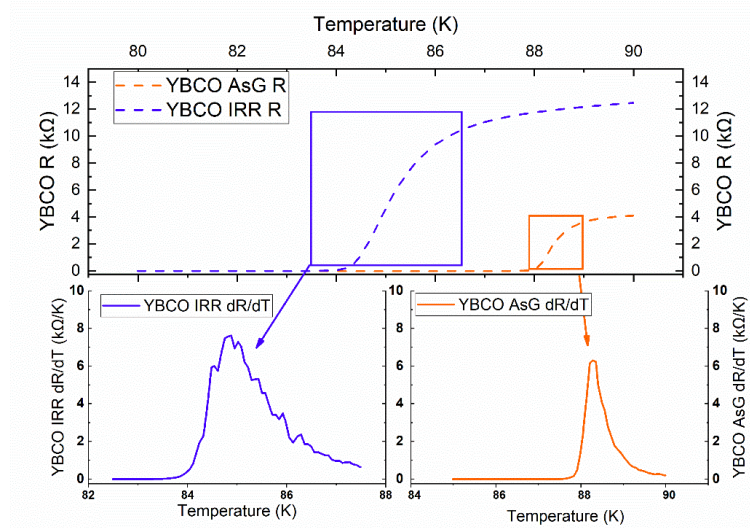
Figure 26: RvsT curve and its derivative of the irradiated (purple) and as grown (orange) meander
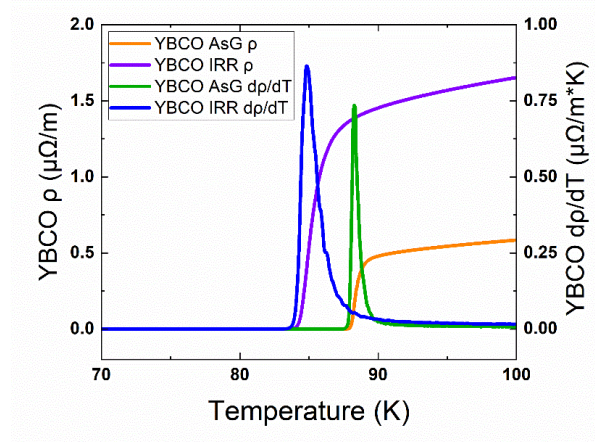
Figure 27: Resistivity versus temperature curve and its derivative for the two meanders

4.1.4 Portable cryostat

The two main advantages of this bolometer are its simplicity and its capacity to work at high temperatures, above the LN_2. The detector is mounted in a custom-wired cryostat produced by Kadel[®] Engineering Corporation shown in Figure 28a, which contains a small dewar that can be filled with LN_2. The LN_2 is in contact with an aluminum base, which is separated by a Teflon[®] foil, from the disk shaped aluminum cold finger. The detector is mounted on the cold finger, whose surface is also cooled by screws in contact with the dewar base. The bolometer can be maintained in a low static vacuum down to 10 mPa, reducing the external heating to the radiation and the noise component linked with the active vacuum pump.

The substrate, over which the YBCO film is deposited, is mounted at the center of an aluminum disk and surrounded by four SMD resistors and one Cernox[®] thermometer, with a precision of 0.1 K. The four resistors are connected in series by a patterned copper film deposited on a Kapton[®] foil glued to the cold finger. Due to the low current required for heating the bolometer and the low resistance of the copper film and the contacts, below 1 Ω, the power dissipated by the film is negligible with respect to the four resistors. The thermometer is employed to maintain the temperature constant, controlling the current in the resistors through a PID temperature controlsystem. The cold finger is anchored with four brass screws; two of them act as a thermal contact between the cold finger and the dewar base, while the others, separated from the holder by insulating material, have a mainly support purpose. This configuration provides a better temperature profile than having all the four screws linked to the heat sink and reduces the current required

to maintain the bolometer at the working temperature. The Teflon® foil, which is inserted between the dewar base and the cold finger, reduces the heat transfer and acts as a thermal decoupler. The incoming radiation, free to pass through an optical window, made by a high-resistivity n-type Si monocrystal. Thanks to the flat transmission above 50% of the silicon in the MID-FIR range, only this radiation can reach the sample, located 5 mm away from the window. This filtering property may be enhanced with a Teflon® foil or Zitex® G110 to block the frequencies above 4 THz [221].

The electrical contacts are made with gold wires of different diameters. Larger wires have been used for feeding the SMD circuit, which requires a higher current, while smaller ones were used for the YBCO and the thermometer. An indium alloy, with a melting point below 200 °C, has been used for soldering the YBCO pads. The relatively low temperature reached during the soldering process does not affect the quality of the film by maintaining unaltered the oxygen content (Figure 28c).
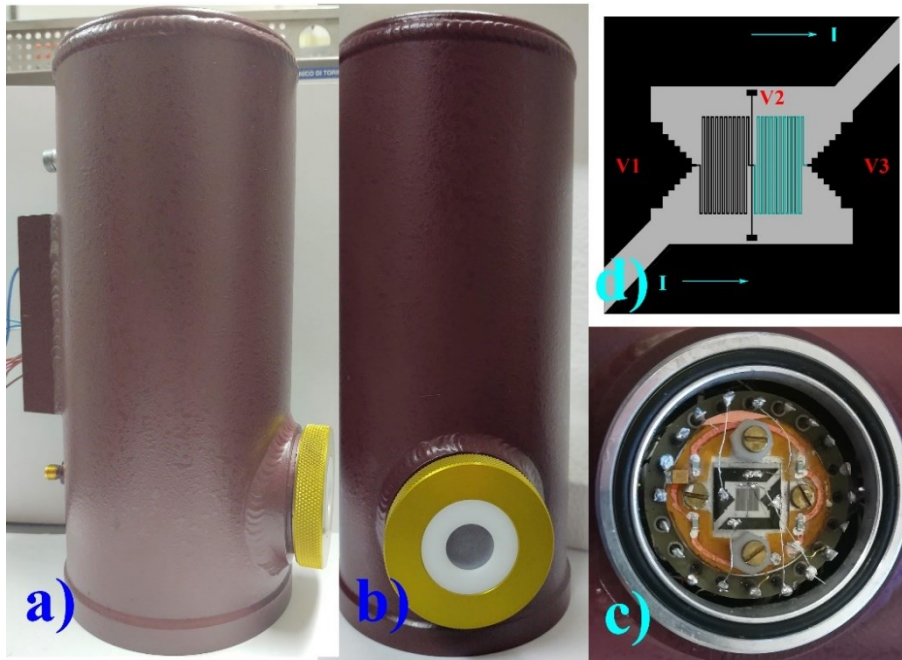
Figure 28: a) Custom-wired cryostat, b) electrical circuit of the bolometer, c) the bolometer mounted on the aluminum holder

4.2 Optimal working point

The performances of the bolometer are strongly affected by the working temperature. A compromise must be found between a high slope in the RvsT curve

and a low resistance. While the first one maximizes the responsivity, the second reduces the Johnson noise. This analysis assumes that the meanders have the same temperature along their entire length and that the variation in the properties of the materials, except for the YBCO resistance, are negligible in the temperature range of operation. These assumptions are confirmed by simulations presented in the following section, which show a temperature gradient below 15 mK on the meander and an increase in temperature during the signal detection in the order of µK.

For a more precise calculation, the measurement is linearly interpolated every 0.01 K from LN_2 boiling point to 100 K. The values outside this range are not helpful for this study. Opportune values of both area and volume of the superconducting film and substrate are inserted to calculate the heat capacity and thermal conductance. Only the volume of the irradiated YBCO is used for the calculations and, since the irradiated YBCO is just a fraction of the entire film, the active area and volume also changes for the substrate. Indeed, the irradiated superconductor covers only an area of 1.65 mm x 3.3 mm with a filling factor of 66%, surface used to analyze the bolometer performances. These assumptions do not affect the qualitative trend of noise and responsivity, but they provide a more precise estimation of the investigated parameters. They directly impact the time constant, linked to the heat capacity of the YBCO and the thermal conductance of the MgO (3.22). The large thermal conductivity of the MgO negatively influences the responsivity but further enhance the main competitive advantage of this device: the small time constant. Using the formula (3.22) and the geometrical value of the bolometer, which are the area, volume and thickness of both the superconducting meander and the substrate, combined with the thermal capacity of the YBCO and the conductivity of the MgO, it is possible to calculate the time constant of the device. The result, compute for just the double meander, considering an overall surface of roughly 3 mm^2, the time constant of the device is around 0.135 µs, which is a good result for a YBCO-based TEB.

The bias current in the film plays a key role since it is directly linked to the responsivity. A high current increases the voltage drop but, at the same time, affects the thermal dissipation and increases the chance of thermal runaways because of the Joule heating. The study aims at finding the maximum current injectable considering both the thermal runaway (4.2) [222] and the Joule heating (4.3). The first one is connected to the thermal conductance G and the derivate of the resistance $\frac{\partial R}{\partial T}$, while the second by the bias current I_{BIAS} and the resistance R. To be

conservative, the electrical losses are set at 5 mW, more than one order of magnitude below the heat transfer from the bolometer and the cryostat.

$$\alpha = \frac{I_{BIAS}^2}{G} \cdot \left(\frac{\partial R}{\partial T}\right) < 1 \rightarrow I_{BIAS} = 27.0 \; mA \qquad 4.2$$

$$P_{EL} = I_{BIAS}^2 \cdot R < 5 \; mW \rightarrow I_{BIAS} = 0.55 \; mA \qquad 4.3$$

The result obtained with these constraints is reported in Figure 29. The thermal runaway, eq (4.2), is the tightest condition, with a current of 27 mA in the point where the RvsT curve has the highest slope, i.e., the worst temperature for the study. The limit sets for the Joule losses determines the lowest bound for the bias current, which decreases with the increase of resistance down to 0.55 mA at 100 K. As a result, the current for studying the optimal working point is conservatively set at 0.5 mA, despite the expected temperature is well below the 100 K.
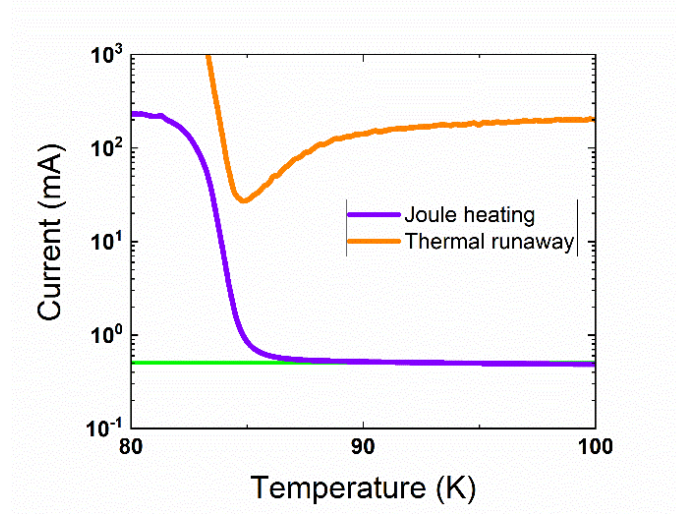
Figure 29: Maximum value of the current considering the Joule heating (purple) and the thermal runaway (orange) in addition to the current chosen highlighted in green

The analysis of the optimal working point is performed assuming the current constant for all temperatures. With this assumption, the Joule heating dictates the lower value. However, a higher margin in the electrical losses may shift the curve in the most critical point, i.e., where the RvsT slope reaches its maximum. Furthermore, it is experimentally easier to set a constant bias current for testing the device at different temperatures, reducing differences between the analytical result and the experimental one.

The optimal operating temperature is chosen for maximizing the responsivity (3.12) and minimizing the total noise (3.18). Figure 30 shows the responsivity and the NEP for temperatures from 80 K to 100 K with a logarithmic scale, the range where the transition takes place. The temperature at which the responsivity has its maximum, 84.83 K, is slightly higher than the corresponding for the minimum NEP, 84.47 K; it is therefore necessary to find another parameter to find the working temperature of the device. It is the ratio between the responsivity and the NEP, shown in the insert in Figure 30. As reported in Table 2, the optimal temperature is a compromise between the maximum responsivity and the minimum NEP. It is set at 84.78 K where the responsivity is 0.448 V/W and the NEP 7.47 $nW \cdot Hz^{0.5}$.
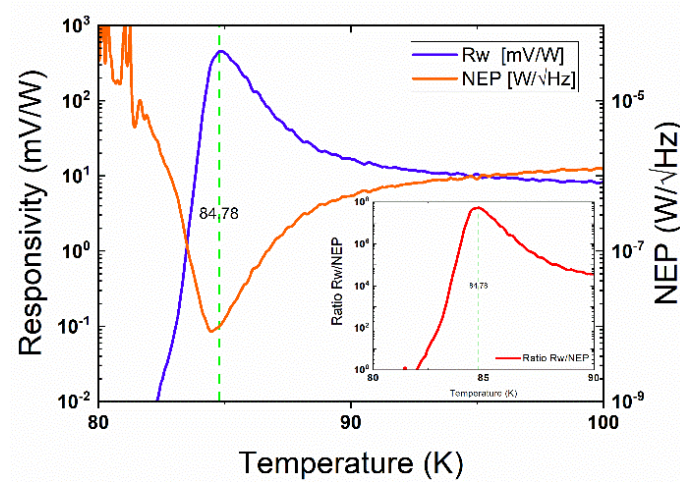
Figure 30: Responsivity and NEP for the bolometer. The insert shows the ratio between the two parameters

Table 2: Performance of the bolometer in correspondence with the best temperature for the responsivity, the NEP and their ratio

Temperature [K]	Responsivity [mV/W]	NEP [$nW \cdot Hz^{0.5}$]	Ratio [$\cdot 10^7$]
84.47	309	**7.35**	4.2
84.78	448	7.74	**5.3**
84.83	**454**	8.86	5.1

5. Finite   Element   Method simulations of the TEB

The Finite Element Method (FEM) is widely used for device design and optimization in many fields. Simulations are surely useful for saving both time and money in the preliminary design phase. Because many physical phenomena are governed by Partially Differential Equation (PDE), which can be solved analytically only for trivial situations, FEM is used to discretize, approximate, and solve them with numerical models. Among different commercially available software for FEM simulations, one of the most powerful is COMSOL Multiphysics®. It allows using some previously implemented sets of equations and introduces personalized ones, constraints, and boundary conditions.

5.1 COMSOL Multiphysics®

COMSOL Multiphysics® is a FEM software used for reproducing many physical phenomena. Released in 1998, version 6.0 came out at the beginning of 2022, replacing the 5.6 one used in this thesis [223]. New physics has been introduced in the years to meet market requirements, such as the *H-formulation* for superconducting materials [224] [225]. Similarly, solvers and interfaces have been continuously improved. Among the various solvers adjusted for each application, such as optimization, eigenfrequency, and frequency study, the ones used in this work are the stationary and the transient ones. They allowed us to find the most suitable materials for critical parts of the apparatus and provide accurate outcomes in terms of the signal response.

5.1.1 CAD model

Due to the complexity of the device and the accuracy required for the simulation, the model was created in an external CAD software, Autodesk Inventor®, which shows good compatibility with the FEM software. It was possible to link the two software for mechanical and structural optimization, but this analysis was neglected because of the negligible mechanical stresses acting on the device. The exploded view of the CAD device and the components are shown in Figure 31. The double meander structure was also created with an external software and then imported in COMSOL, directly on the MgO substrate. Because of its thinness, the

superconducting circuit was imported as a 2D surface and was simulated with appropriate physics dedicated to thin films under both electrical and thermal points of view.
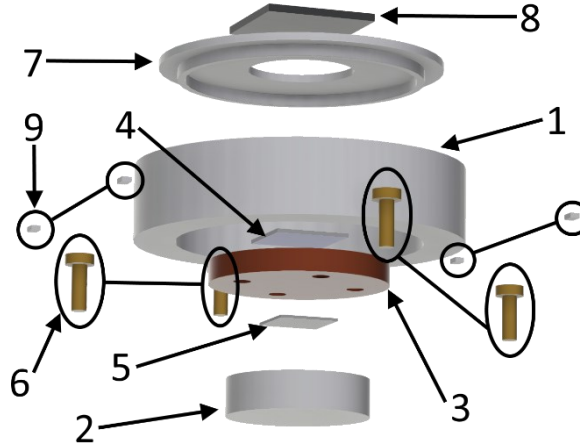
Figure 31: Exploded CAD of the detector. It includes cryostat enclosure (1), aluminum base in contact with LN2 dewar (2), aluminum cold finger (3), MgO substrate and YBCO film (4), Teflon® thermal coupler (5), screws (6), cover with high resistivity silicon optical window (7-8) and SMD resistors (9)

5.1.2 Physics

Electrical and thermal modules are used for a complete device simulation, while the PID (proportional–integral–derivative) temperature control system is implemented using the mathematical module dedicated to ordinary differential equations. The physics are detailed below, together with the equations and the components included.

The *Heat transfer in solids* module uses the Fourier laws in their differential form (5.1 and 5.2) to calculate the diffusion of heat, and is defined thanks to boundary conditions such as fixed temperatures and heat sources. The temperature, which is the dependent variable, is calculated considering the density, ρ, the specific heat, C_p, the heat flux, both conductions, $\boldsymbol{q}$, and radiation $\boldsymbol{q_{rad}}$ and all the additional heat sources, which are included in Q.

$$\rho \cdot C_P \cdot \frac{\partial T}{\partial t} + \nabla \cdot (\boldsymbol{q} + \boldsymbol{q_{rad}}) = Q \qquad 5.1$$

$$\boldsymbol{q} = -k \cdot \nabla T \qquad 5.2$$

A specific set of equations allows studying the temperature evolution in thin layers considering both normal and tangential heat fluxes, which are crucial for the correct reproduction of the thermal diffusion in the YBCO film [226]. A simplified simulation can be obtained considering the temperature constant across the film, but the gradient along its thickness was considered to simulate the bolometer correctly. The evolution of the temperature is governed by Eqs. (5.3 - 5.5) in which the subscripts u and d refer to the upper and lower face of the film, q to the out-of-plane heat flux, d_S to the layer thickness and R is the thermal resistance calculated with the film thickness and conductance.

$$-n_d \cdot q_d = -\frac{1}{2} d_s \rho C_p \frac{\partial T_d}{\partial t} - \frac{T_u - T_d}{R_S} + \frac{1}{2} d_s Q_s \qquad 5.3$$

$$-n_u \cdot q_u = -\frac{1}{2} d_s \rho C_p \frac{\partial T_u}{\partial t} - \frac{T_d - T_u}{R_S} + \frac{1}{2} d_s Q_s \qquad 5.4$$

$$R_S = \frac{d_s}{k} \qquad 5.5$$

The constraints were the fixed temperature at the bottom of the cold finger, below the PTFE thermal coupler, set at 77.6 K (the boiling temperature of the LN2), and the room temperature on the outer part of the shield, set at 300 K. Radiation was included to simulate the effect of the vacuum inside the device. The boiling nitrogen has been neglected since the associated noises, both thermal and mechanical, were considered well decoupled from the detector. This assumption reduced the dimension and complexity of the simulation and will be introduced if the experimental results show low-frequency noise attributable to this phenomenon. Another simplification can be replacing the Joule heating of the resistors with a fixed heat source, but the small computational cost associated with that physics is negligible compared to the whole model. A more significant reduction can be achieved by replacing the incoming radiation with a traditional heat source on the boundary.

The thermal model also includes *Surface-to-Surface Radiation*, which computes the heat transfer by radiation and is limited to the boundary level, i.e., surfaces. It allows defining transparent or opaque mediums, a feature used to reproduce the transparency of the silicon window to wavelengths between 1 μm and 1 mm. With this physics, a point source was included with a blackbody temperature

of 900 K to reproduce an electromagnetic radiation coming from a filtered mercury lamp comparable to the one used for the experiments. The physics is governed by a trivial equation: an additional heat source linked with radiation (5.6) where ε is the surface emissivity, G is the irradiation term, and $e_b(T)$ is the blackbody hemispherical total emissive power. The calculation of the irradiation contribution and the view factor is associated with a high computational cost. Therefore, only the bolometer surface and the optical window were included, reducing the required memory.

$$-\boldsymbol{n} \cdot \boldsymbol{q} = \epsilon(G - e_b(T)) \qquad\qquad 5.6$$

The *AD/DC* module is used for both the heaters and the superconducting film. *Electric current* implements eqs. (5.7 - 5.9), where the current density J, the electric field E, the charge Q_j and the conductivity, σ, allow calculating the electric potential, V, which is the dependent variable. The displacement current has been neglected in the SMD because of the slow time variation, simplifying the model. The PID control system, implemented with differential equations, controls the current supplied individually in each resistor.

$$\nabla \cdot \boldsymbol{J} = Q_{j,v} \qquad\qquad 5.7$$

$$\boldsymbol{J} = \sigma\boldsymbol{E} + \boldsymbol{J_E} \qquad\qquad 5.8$$

$$\boldsymbol{E} = -\nabla V \qquad\qquad 5.9$$

The YBCO film required an appropriate physics: *Electric Currents, Single Layer Shell*, which can be used in boundaries where the skin depth is much larger than the device. The thickness is treated as a multiplicative factor for calculating current and resistance. The accuracy of the simulation is ensured by an extra virtual dimension for the layer.

Finally, the *Global ODEs and DAEs* module reproduces the effect of the PID control system. It compares the average temperature of the irradiated meander with the reference one, the optimal working point, and adjusts the current in the resistors, multiplying the maximum value by "u", defined as (5.10 - 5.13). The subscripts p, i, and d refer to proportional, integral, and differential, respectively. The k-values were chosen for fast temperature recovery when minor variations occur.

$$u_P = k_p \cdot err;$$ 5.10

$$u_i = \int \left(k_p \cdot err \right) dt$$ 5.11

$$u_d = k_d \cdot \frac{\partial err}{\partial t}$$ 5.12

$$u = u_p + u_i + u_d$$ 5.13

Essential is the pairing between the different physics: the Joule heating in both bulk and film material and the heating by radiation from the surface to the bulk. The coupling between the *AC/DC* and the thermal module reproduces the Joule effect with the same equation for the superconductor and the resistors. When applied to the SMD allows thermalizing the surface, while in the YBCO film it was used to study possible runaway and critical values of current and temperature. The coupling of the two thermal physics, i.e. *Heat transfer in solids* and *Surface-to-Surface Radiation* allowed computing the view factor and to evaluating the heat deposited in from the radiation in to the solids. Except in the *Surface-to-Surface Radiation*, the variables have been quadratically discretized to obtain more precise results.

5.1.3 Materials

The definition of the materials properties is essential for obtaining reliable results. It is particularly crucial at low temperatures in which these parameters strongly differ from room temperature one and may vary significantly in a range of few Kelvins.

The electrical parameters were limited to the YBCO film and the four resistors, which acted as heaters. The characterization performed on the superconductor, shown previously, provides the RvsT curve, while the SMD resistors keep their nominal resistance at low temperature.

The thermal properties are well described in the literature because the materials employed are widely used in the cryogenic domain. The YBCO and MgO properties are obtained with the analytical formulations reported in (5.14 - 5.18). The only parameter which does not vary with the temperature T is the out-of-plane YBCO thermal conductivity (5.15). The YBCO in-plane thermal conductivity and the MgO

one (5.14) and (5.17) use analytical parameters from [227] and [230]: a, b and c with the subscript Y and MgO respectively and, for the YBCO. The heat capacity of the YBCO varies linearly with the temperature (5.16), while the MgO one is calculated with the Debye formula (5.17), which consider the Avogadro number, N_{Av}, and the Debye temperature of MgO, θ_{MgO}.

$$k_{inYBCO} = \frac{\kappa_N}{2} \left(\frac{T}{T_C} + \sqrt{a_Y^2 + \left(\frac{T}{T_C} - b_Y \right)^2} - \sqrt{a_Y^2 + b_Y^2} \right) \cdot$$
$$\exp\left[-c_Y \cdot \left(\frac{T}{T_C} - 1 - b_Y \right) \right] \text{ [227]}$$
(5.14)

$$k_{outYBCO} = 2 \text{ [228]}$$
(5.15)

$$C_{pYBCO} = \theta_Y \cdot T \text{ [229]}$$
(5.16)

$$k_{MgO} = 150 + \left(\frac{a_{MgO}}{T} + b_{MgO} \cdot T^{c_{MgO}} \right) \text{ [230]}$$
(5.17)

$$C_{pMgO} = \left(\frac{12}{5} \pi^4 N_{Av} * k_B \left(\frac{T}{\theta_{MgO}} \right)^3 \right) \text{ [231]}$$
(5.18)

The other materials are inserted as logarithmic and exponential expressions obtained from data interpolation. The data range from a few Kelvin to room temperature, with specific errors in a few percent. The only property not included in the NIST database [232] is the heat capacity of the brass, which is imported in the software as linear interpolation. Table 3 reports the data sources together with the density used in the model. Unlike the other properties, this last one is maintained constant in the whole temperature range. The material properties are reported in Figure 32 for all the materials used in a temperature range between 25 and 100 K.

Table 3: Thermal properties and density of the material under study

Materials	Thermal conductivity	Heat Capacity	Density [kg/m³]
Aluminum [234]	NIST data interpolation	NIST data interpolation	2700
Brass [235]	NIST data interpolation	Linear interpolation	8550
Copper [232]	NIST data interpolation	NIST data interpolation	9000
Teflon® [234]	NIST data interpolation	NIST data interpolation	2200

a)   b)
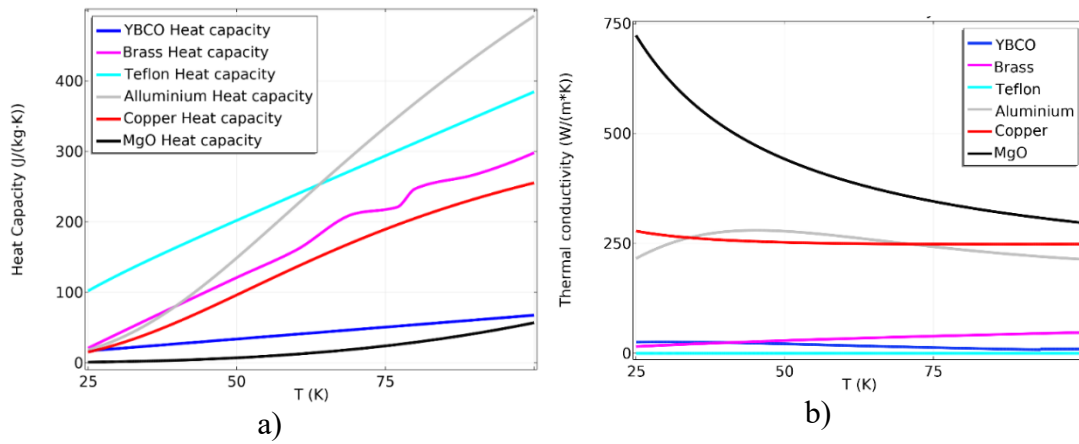
Figure 32: a) Heat capacity and b) thermal conductivity of the materials of interest in the range between 25 and 100 K

5.1.4 Mesh

The meshing procedure follows a precise order: since the domain already meshed impacts the element of the adjacent ones, it is necessary to start from the most important one. The YBCO film is the first part which was meshed; a fine triangular mesh is built because of its 2D nature and the high accuracy required in the simulations. Then, the MgO substrate was meshed in the whole 3D domain,

starting from the fine elements of the YBCO surface and slightly coursing them when reaching the boundary with the other components. The elements of these two domains already count almost 30% of the total. The sensor holder and the screws are meshed next, concluding with the remaining parts.

The final mesh counts around 110000 elements with an average quality of 0.60 and a minimum of 0.05. The mesh and the histogram of its skewness quality are shown in Figure 33a and Figure 33b. Some elements of relatively low-quality are present in the silicon window, which acts as the filter and does not require an high-quality. The bolometer, which is prioritized in the meshing process and present many elements, shows mainly high-quality elements. All elements are triangular or tetrahedral shaped to improve the convergence.

a)   b)
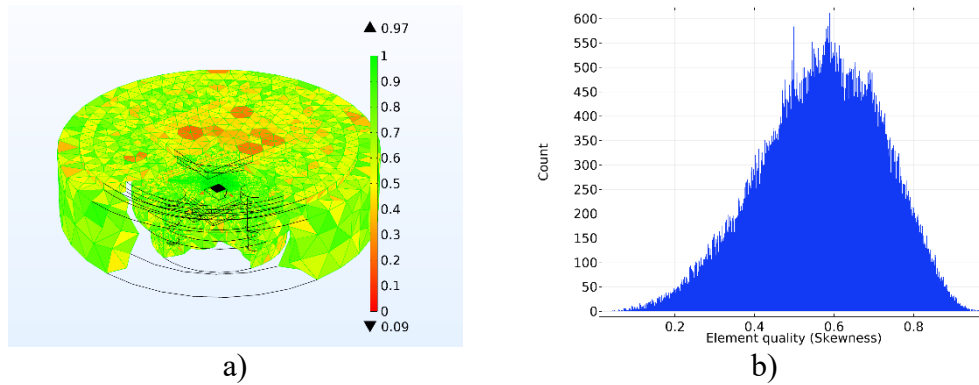
Figure 33: a) Cut view of the bolometer with the mesh quality factor and b) histogram of the element quality in the mesh

5.2 Simulations

The device is simulated to check both the stationary and transient performances. The first study defines the most suitable material for the sensor holder and the screws, components easy to replace and which strongly affect the temperature profile and its evolution during transients. Then the YBCO temperature and the voltage drop across the meander are studied and compared with analytical results. Signals of different lengths are simulated to study the device response to delta and train pulses, both electrically and thermally, looking at the time constants of the superconductor and its substrate. Finally, other bolometer patterns and materials are analyzed.

5.2.1 Material selection

Four different materials are investigated for the screws and two for the sensor holder to find the best materials combination for the bolometer. The screws are simulated with aluminum, copper, brass, and Teflon®, while the sensor holder is modelled only with the first two elements, as reported in Table 4. The simulations aim at analyzing when the working temperature is reached in the irradiated meander. Due to the potentially infinite precision of the simulation, the limit is set on the heating current: the simulation ends when the current reaches a precision of 1 µA. Nevertheless, it represents a good result that can also be achieved experimentally, such as the associated temperature distribution.

Table 4: Combinations of materials under study

Sensor Holder	Screws			
Aluminum	Aluminum	Brass	Copper	Teflon®
Copper	Aluminum	Brass	Copper	Teflon®

Figure 34 and Figure 35 report the thermal profiles obtained on the YBCO and MgO surface expressed as the difference from the working temperature. In these figures, the aluminum is colored in grey, the brass in orange, the copper in red, and the Teflon® in cyan. Due to the high difference between the high conductive materials, copper and aluminum, and the more insulating ones, brass and Teflon®, the temperature range has been limited to 40 mK. Therefore, every section which differentiates more than 20 mK from the working temperature, 84.78 K, is maintained at the same color: blue for temperatures below 84.76 K and red for temperatures higher than 84.80 K. The distribution symmetry confirms that the dissipation in the irradiated meander is negligible. Higher currents would impact the thermal distribution because of the Joule heating, with possible consequential creation of hotspots or thermal runaways during the signal detection. The profiles are similar for the two holders, and significant differences are introduced by the screws materials, particularly between metallic and plastic ones.
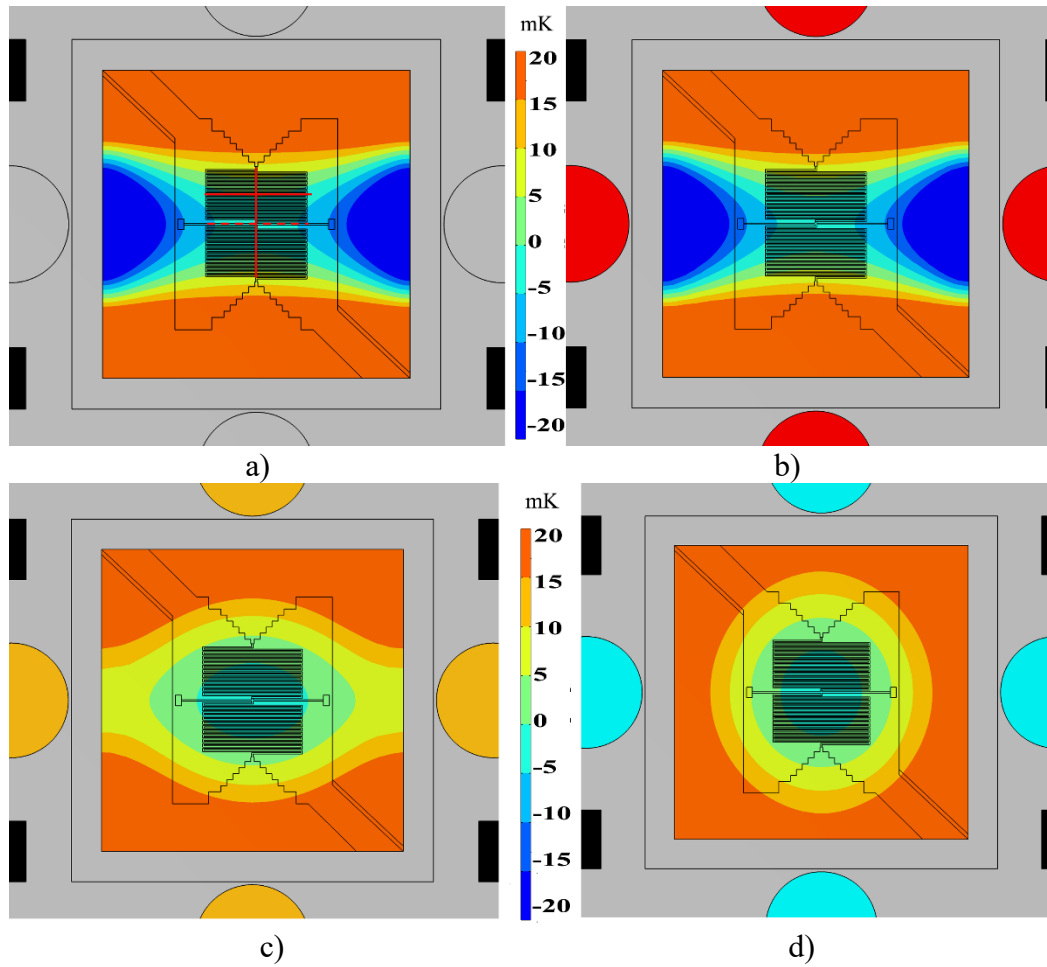
Figure 34: Differences from the working temperature (84.78 K) distribution for the various combination of screws on the aluminum (grey) holder: a) aluminum, b) copper, c) brass, d) Teflon®. On a) the lines (red, straight and dashed) indicate where the linear profiles of the temperature are extrapolated
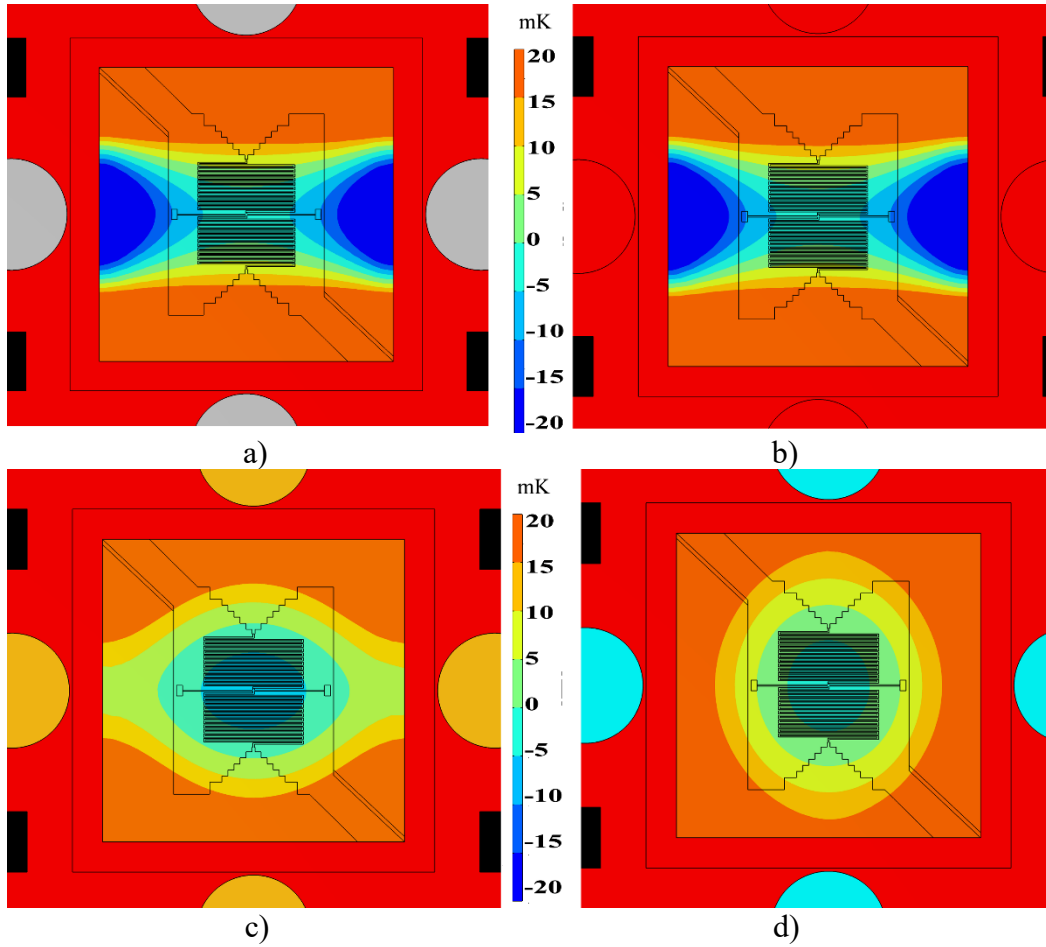
Figure 35: Differences from the working temperature (84.78 K) distribution for the various combination of screws on the copper (red) holder: a) aluminum, b) copper, c) brass, d) Teflon®

The temperature is extrapolated along perpendicular lines passing through the center of the irradiated meander, solid lines in Figure 35a, to empathize the temperature differences in the various combinations. The temperature is also measured at the center of the device, dashed line, and reported in the same graph for comparison. Figure 36 shows the temperature profile as the difference from the reference one, 84.78 K. Along the x-direction, the temperature is reported both for the irradiated meander, solid line, and the center of the bolometer, dashed line. Again, the similarity between the two sensor holders is evident, while the better performance with brass and Teflon® screws in all the configurations is appreciable. The profiles show a symmetry in the temperature distribution of the bolometer and the excessive mismatch of the cooling effect of the copper and aluminum screws.
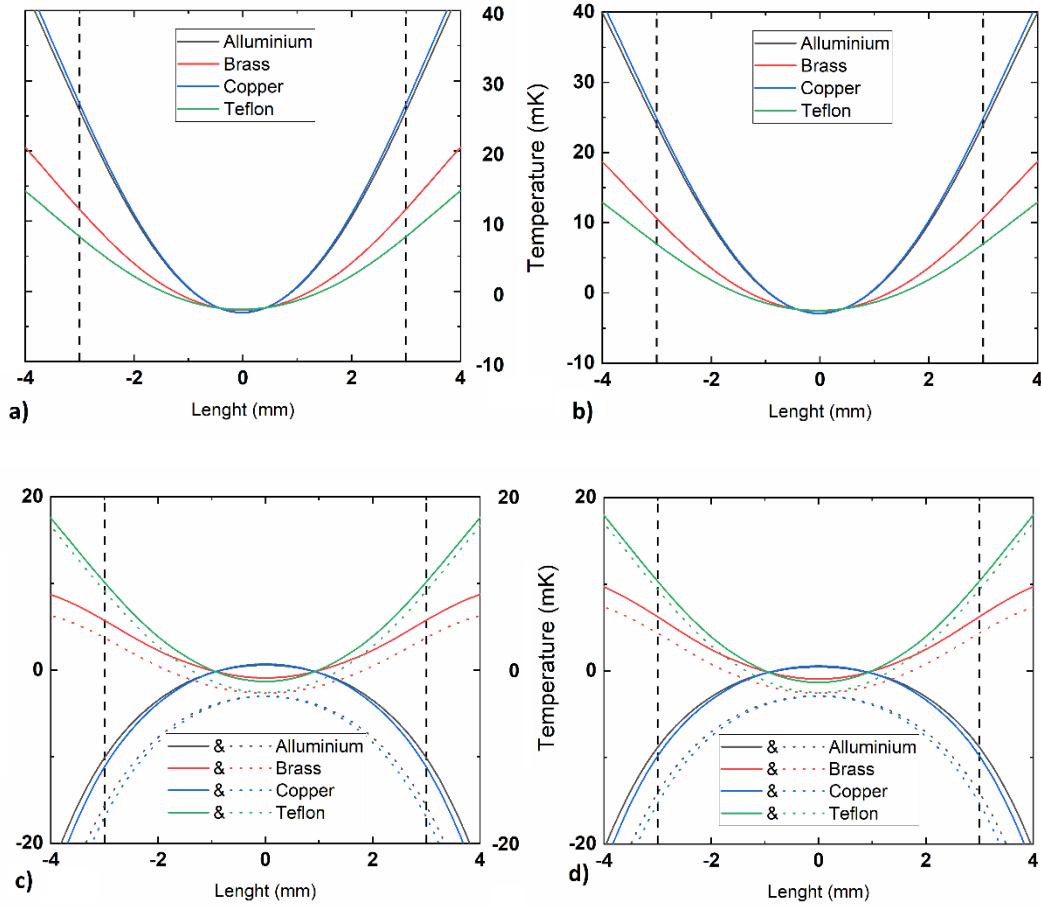
Figure 36: Linear profiles along horizontal lines for the various screws kinds and a) aluminum and b) copper sensor holder and along vertical lines for the same screws kinds and c) aluminum and d) copper sensor holder. The dashed line in c and d refer to the line passing through the center of the bolometer.

Table 5 states the maximum and minimum temperature in irradiated meander, their difference, the current and the power required to maintain the temperature profile.

The thermal distributions prove that the sample holder material produces just slight variations while a large diversity occurs by changing the screws materials. Aluminum and copper have high thermal conductivities and generate a large temperature gradient across the bolometer, especially in the x-direction, where it reaches a mismatch of 25 mK. The moderate conductivity of the brass limits the heat absorption from the side of the substrate and produces a more homogeneous distribution around the meanders. The small thermal conductivity of the Teflon®, used as an example of insulating materials, produces an entirely different pattern in

the 2D distribution. The screws thermal link with the cold finger is strongly suppressed and the cooling process through the center of the bolometer, passing by the Teflon® foil, becomes more important, generating a minimum at the center of the bolometer.

Table 5: Current and power required to maintain the bolometer at the working temperature and maximum and minimum temperature on the irradiated meander and their difference for the studied configuration

Holder	Screws	Current (mA)	Power (W)	Max T (K)	Min T (K)	ΔT (mK)
Al	Al	104.372	2.179	84.789	84.774	15.8
Al	Cu	107.117	2.295	84.790	84.773	16.6
Al	**Brass**	49.739	0.495	84.785	84.777	8.0
Al	**Teflon®**	12.991	0.034	84.785	84.777	7.5
Cu	Al	107.175	2.297	84.789	84.774	14.6
Cu	Cu	109.860	2.414	84.789	84.774	15.3
Cu	Brass	54.705	0.599	84.785	84.777	7.7
Cu	Teflon®	26.568	0.141	84.785	84.777	7.3

As a preliminary result of the stationary study, Teflon® and brass are the two elements that better fit the requirements of the screws. The decision on the sensor holder is not so obvious since the differences in thermal distributions and the maximum and minimum temperature difference are almost negligible. The aluminum holder was chosen considering the importance of low power dissipation: it is 10% lower for the brass screws and almost half for the Teflon® screws compared to the copper holder. A similar discussion cannot determine which material is better for the screws due to the completely different nature between the brass, metal with good thermal conductivity, and the Teflon®, plastic and thermal insulator. Despite the lower power dissipated by the Teflon® screws, a transient

simulation is performed to analyze the bolometer response to external signals to find the best candidate.

The transient simulation lasts for almost three minutes, during which two main events happen. At the beginning of the study, there is a sudden change in the PID current, and, after 100 seconds, an electromagnetic signal impacts the detector. The current in the resistors is switched off for less than 0.1 seconds, and it is set in correspondence of the beginning of the time axis, Figure 37. The incoming signal, impacting 100 seconds later, has a duration of 1 ms and a power of 30 mW.

Figure 37 shows the average temperature evolution of the irradiated meander for the whole transient as the difference from the working temperature. The insert focuses on the response of the bolometer after the signal, with an enlarged scale in the y-axis to better appreciate the oscillations, not visible in the larger graph. The two configurations respond differently to the sudden current variation. The brass screws have more considerable oscillations, almost five times bigger than the other configuration, but recover the working temperature faster. Contrariwise, the minor fluctuations associated with the Teflon® screws protract a longer time, impacting the detection of the signal. Indeed, even after 100 seconds, the temperature with the Teflon® screws still oscillates around the working point. This masks the incoming signal, which cannot be distinguished from the prolonged fluctuations. It is not the case for the brass screws, in which the signal is evident and stands out from the random thermal fluctuations around the operating temperature.

For these reasons, as also reported in [236], the best materials selection for this apparatus consists of a holder of aluminum, which reduces the current and power required for maintaining the temperature constant, and brass screws, which provide an excellent thermal distribution and fast responses to external events.
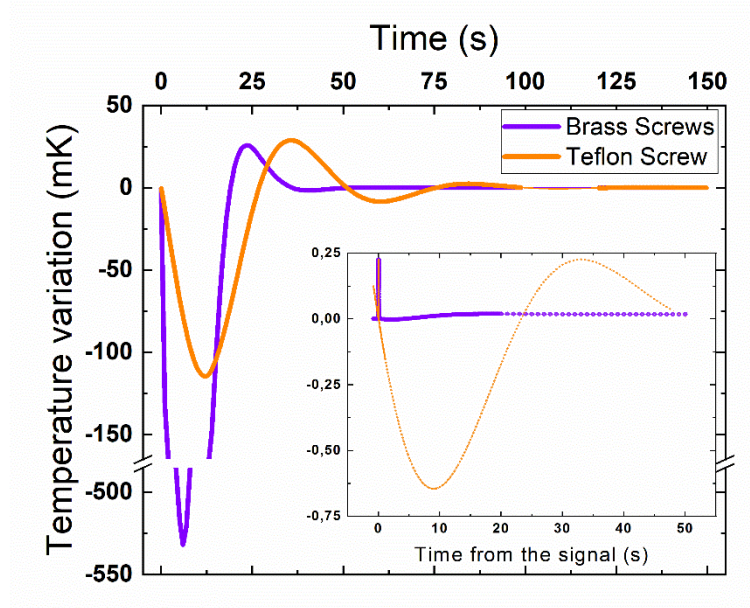
Figure 37: Evolution of the YBCO average temperature in response to a switch-off of the current in the resistors, focus on the effect of the temperature oscillation in the signal detection after 100 seconds. In the insert, the time is set at 0 in correspondence to the signal detection

5.2.2 Response to the signal

The response to an external signal has been studied after the optimal material has been chosen, i.e., brass screws and aluminum holder. Employing the FEM software, it is possible to study variation in voltage and temperature at the limit of the experimental results, with an arbitrary time resolution.

The first study focuses on a very short pulse, chosen to reproduce a Dirac delta, to examine the temperature evolution of the materials, particularly the YBCO and the MgO. With a 10 ps pulse that releases an overall energy of 1.5 pJ, this analysis intent to extrapolate the thermal time constant of the materials. The outcomes aim at validating the model, as preliminary done in [237].

Figure 38 shows the evolution of the YBCO temperature and the voltage drop across the irradiated meander. They follow the same trend since the thermal coefficient α connects them as the multiplication factor. Their increases are almost instantaneous because of the low thermal capacity of the YBCO film of only 250 nm of thickness. The exponential fitting well traces the decreasing of the temperature in both the short and long term, as highlighted in the insert in Figure 38. The temperature increase and the voltage drop across the irradiated YBCO

obtained using the FEM software are respectively 2.3 µK and 7.1 µV, in the same order as the calculated ones, which are 5.5 µK and 20.0 µV. The approximations used in the analytical calculation by considering the system wholly isolated and the process instantaneous may be responsible for the discrepancy between the two methods. The FEM software considers multiple time steps during the detection of the transient in which the heat can be transferred in the substrate through conduction and in the surrounding by radiation.
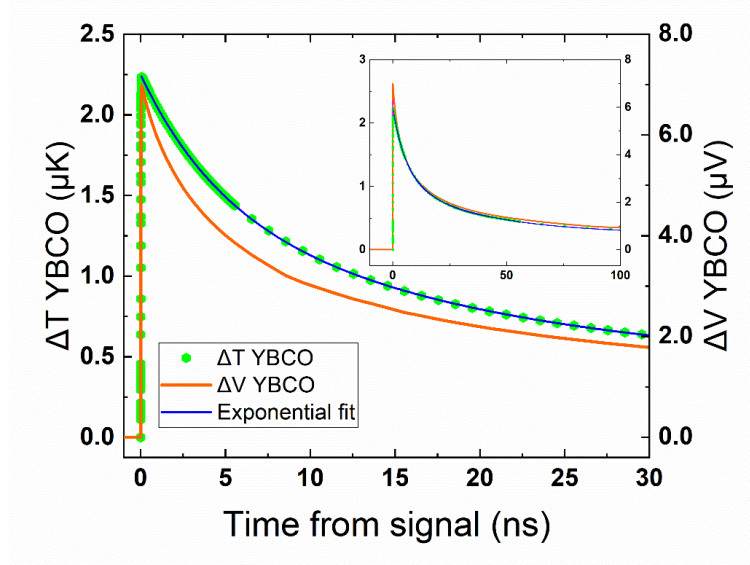
Figure 38: Bolometer response to a infrared pulse of 10 ps. Temperature and its exponential fit are reported together with the voltage drop. The insert shows the evolution on a longer time scale

A similar analysis is performed for the MgO substrate, the only part which undergoes a detectable temperature variation after such a weak signal. Due to the larger size, the temperature is collected at the central point of the substrate instead of averaging over the whole volume. Figure 39 reports the temperature variation for the MgO and the curve obtained with the exponential fitting. Unlike the YBCO film, the MgO requires an extended amount of time to reach its maximum temperature and this value is almost 100 times smaller than in the superconductor. This is mostly due to the larger specific heat capacity of the substrate, directly connected with the volume, and partially to the film above the material, which partially screens the signal.
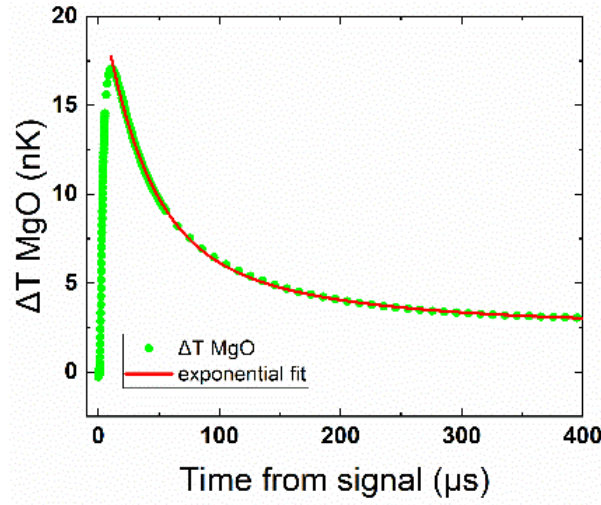
Figure 39: Temperature evolution at the center of the MgO substrate and its exponential fit

The time constants are calculated analytically with the formula (3.22), which considers the heat capacity and the thermal conductance. The whole volume of the substrate is considered for the MgO, while only the irradiated meander for the YBCO. The results are then compared with the exponential fitting of the data obtained through FEM simulations. The fitted values go from the maximum temperature to the time at which this decrease of 75%, considering only the exponential part of the transient. The time constant of the YBCO obtained through simulation is 9.6 ns, comparable with the analytical one, which is 4.6 ns. The value for the MgO is 51 µs, roughly half of the one found analytically, which is 90 µs. The obtained results are reported in Table 6.

Table 6: Comparison between results obtained thought calculation and simulation

Results	Analytical	From exponential fit
ΔT YBCO [µK]	5.5	2.3
ΔV YBCO [µV]	20.0	7.1
τ YBCO [ns]	4.6	9.6
τ MgO [µs]	90	51

This study has been limited to the two main components because higher incoming power that would have reached the underlying material would have negatively impacted the thermal and electrical analysis of the YBCO and MgO. Indeed, the temperature variation in the deeper components does not show a recognizable trend, such as a defined peak and an exponential decrease, and therefore is not useful for further analysis. In the central point of the aluminum holder there is a slight temperature increase, even smaller than in the MgO, which arise hundreds of μs after the peak in the YBCO temperature appears. In the Teflon®, the variation is even smaller, comparable to the random thermal fluctuation, and it is difficult to understand if it is due to the signal or the heating of the resistor during the recovery of the temperature.

Further tests are performed through FEM simulations, such as the response to a short and fast series of pulses and the capability to return in the equilibrium condition. In the INFN-TERA project, a parallel work package aimed at developing a THz spectroscopy with the new generation radiation sources. For this purpose, a mode-locked femtosecond laser (FemtoFiberNIRpro, Toptica) at 780 nm, with an 80 MHz repetition rate, is used [238], the same which will be employed to test the bolometer under study. Several transient simulations are made for validating the time constants found above. In order to study the evolution of the temperature in the YBCO film, four sub sequential pulses are simulated, as reported in Figure 40a-c. The time intervals between the pulses are 4 ns, 15 ns and 7.5 ns, respectively smaller, bigger and in between the two time constants previously found. Each pulse is maintained with a length of 10 ns and a power of 10 mW.

Looking at Figure 40a, it is possible to see that a distance of 4 ns between two separate peaks does not allow distinguishing the signal. Indeed, there is a variation of less than 15% from the peak of the pulse and the baseline of the following one, making them very difficult to distinguish. In the second case, in Figure 40b, with a distance of 7.5 ns, it is easier to define the various pulses. Indeed, for two subsequential signals, the peak value, and the base of the following one, have a difference of around 25% with respect to the maximum reached when the signal is switched off. For the final simulation, Figure 40c, when 15 ns separate the pulses, the temperature at the beginning of the pulse is at 60% of the peak one. In this latter case, the separation between the pulses grants a good definition, especially for the first two, when the bolometer does not have residual heat from the previous pulses yet.

a)

b)

c)
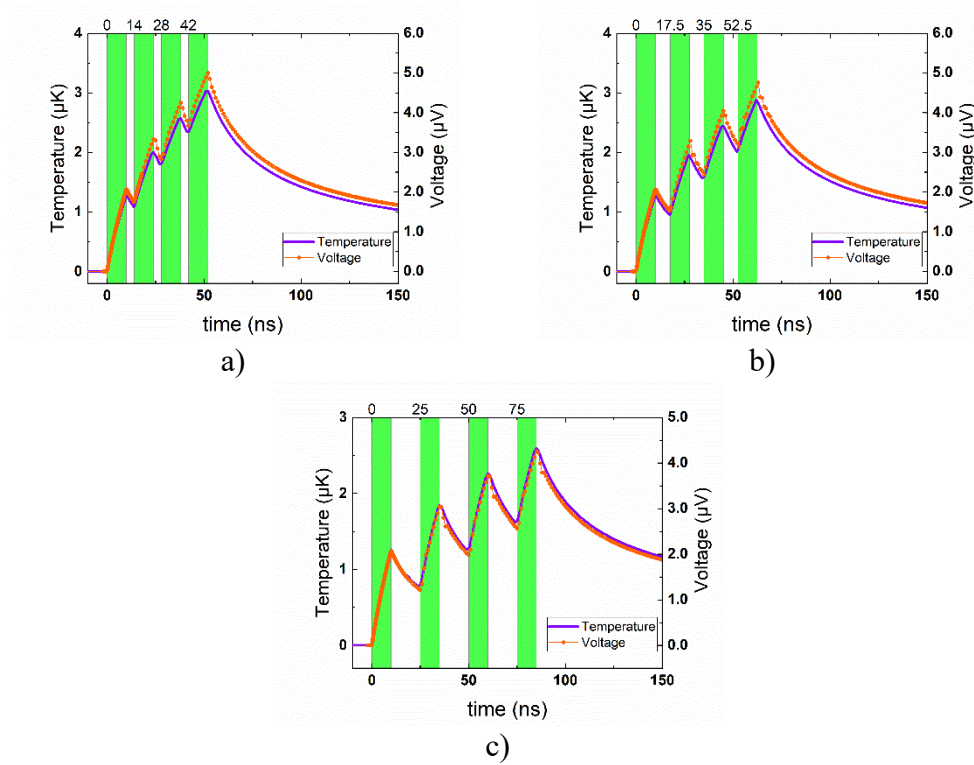
Figure 40: Response of the bolometer, the average temperature of the film and voltage drop, to four pulses of length 10 ns and power 1 mW separated by a) 4 ns, b) 7 ns and c) 15 ns

As expected, the temperature reached at the peak of the last pulse is higher for the shorter time interval between the pulses. The heat is not completely removed by the substrate, despite the high thermal conductivity. A less conductive substrate would result in a higher responsivity, but a less reactive device.

To check the evolution of the substrate, similar simulations are performed, taking into account the larger time constant of the MgO. Due to the longer time required by the MgO to come back at its temperature, only two pulses are simulated. They have a duration of 1 µs, a power of 3 mW, and are separated by 50 µs and 100 µs, respectively, as reported in Figure 41

As expected, the influence of the previous peak is minimal on the second one for both simulations. When the interval between the two signals is 50 µs, the temperature is dropped by almost 95%, while for the second case, it goes down by 96.3%. The not complete recovery may also be attributable to a trend in the simulation, for which the temperature is still slightly oscillating on a longer time scale. Indeed, the simulation well reproduces the thermal fluctuation due to the PID

control system and the incoming radiation, with the result that the temperature slightly oscillates around the working temperature.
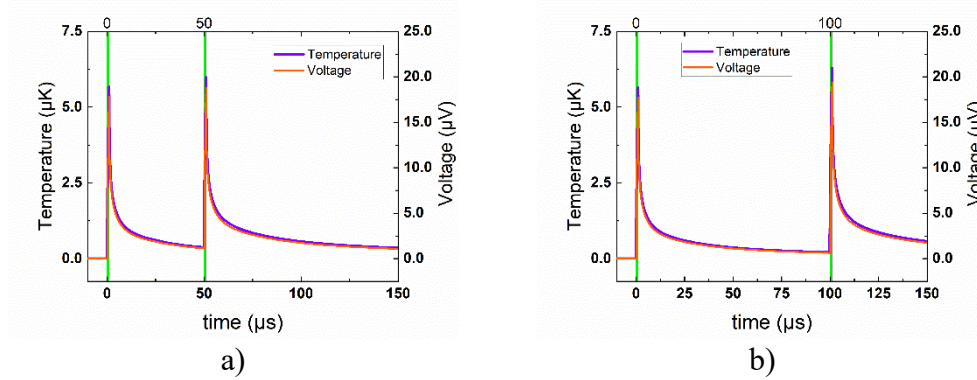

Figure 41: Response of the bolometer, the average temperature of the film and voltage drop, to two four pulses of length 1 µs and power 3 mW separated by a) 50µs and b) 100 µs

This analysis shows that the time required for the system to recover the initial temperature is longer than the time constant of the YBCO, despite already at 15 ns of distance is possible to distinguish two subsequential peaks. Regarding the temperature evolution connected with the substrate, after 50 µs the recovered value is within 6% of the previous temperature, and decreases to 4% if the time interval is doubled to 100 µs.

5.2.3 Other layout

As mentioned before, one advantage of FEM simulations is the possibility of reproducing experimental situations in fast and inexpensive ways. For this reason, the FEM simulation is exploited to study a refined bolometer that can improve detectivity and spatial resolution. The new design presents a more complex geometry and a higher filling factor of around 95%, compared with 66% of the previous structure, as shown in Figure 42. Instead of two wide and broad meanders, this new structure presents four sectors with a thinner serpentine design to improve its performance. The four-meanders layout presents a longer and thinner pattern, resulting in a larger resistance and, consequently, its derivative, positively impacting the responsivity. Furthermore, compared with the two meanders geometry, it can be employed for obtaining a position dependent detection of the incoming radiation, useful for ray calibration, without losing the electro-thermal effect connected with the pristine meanders.
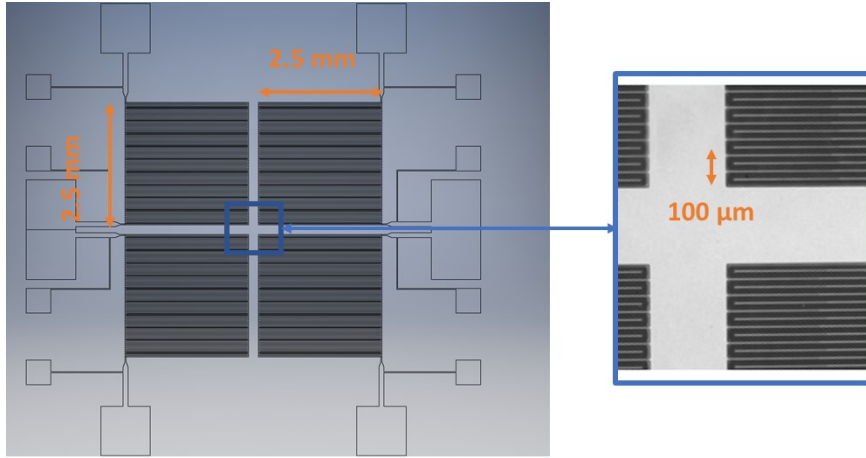
Figure 42: CAD and optical measurement of the four-meanders design

In addition to the distinct geometry, simulations easily allow reproducing the response of the bolometer with different RvsT curves for the different sectors, i.e., different T_C. However, to compare the two geometries, the same material of the simpler bolometer is assumed in the new layout. It means that the same substrate and a superconducting material, with the same thermal properties and ρvsT are used in the simulations. Two of the four meanders are left as grown and the other irradiated, placed in the opposite position, as shown in Figure 43.
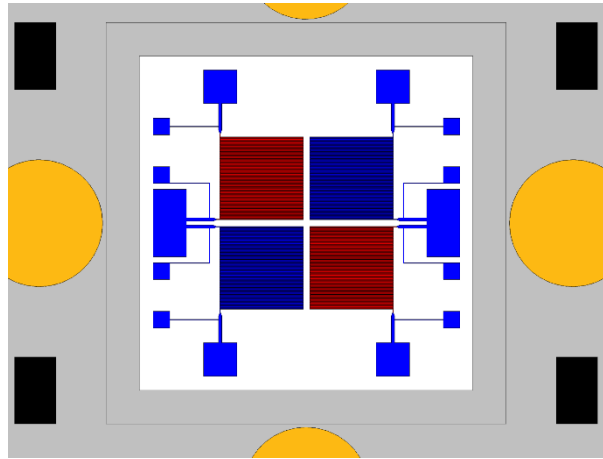
Figure 43: The four-meanders geometry. The different colors for the YBCO film reflect different RvsT curves; pristine, blue, and irradiated, red

The trimmer features of the four-meanders design are a challenge for both the manufacturing and the simulation. The smaller meanders and the thinner distance between them are at the limits of the optical resolution in the photolithography

process performed at Politecnico di Torino, while it was extensively respected in the previous design. On the other hand, the FEM model faces different problems, such as the mesh and the number of degrees of freedom (DOF).

Only the superconducting film counts 233555 triangular elements, increasing to 1.2 million when the substrate has meshed. The final number of elements, which have an average quality of 0.53, is 1.43 million, over ten times the ones in the previous bolometer. The meshing process is optimized to maintain the quadratic discretization for all the modules. Implementing the various physics, the irradiation process is substituted with a constant heat source on the bolometer surface, and the signal is included in the *Heat transfer in solids* as a temporary heat source on the surface of the bolometer. Also, the geometry is simplified by eliminating the external cover, considering the external temperature fixed at 300 K. These simplifications allow simulating in a reasonable amount of time, without losing the accuracy of the process.

As previously done for the two-meanders configuration, a preliminary analysis is performed on the device, considering the new geometrical factor, in particular the equivalent thermal conductivity of the substrate. This study permits to find out the maximum bias current and the optimal working temperature of the device. The considerable resistance of the new geometry strongly impacts the electrical current. Again, the restricting parameter is the Joule heating, limiting the bias current to 0.15 mA, less than one-third of the previous layout, as shown in Figure 44a. The optimal working point is mainly affected by the RvsT curve; since the ρvsT is the same as the preceding device, the temperature results unchanged despite the different areas of the substrate, which impacts the thermal relaxation of the bolometer. The temperature which optimizes the ratio responsivity over NEP is 84.78 K, as shown in Figure 44b.

The first study aims at checking the thermal distribution when the working temperature is reached, using the combination of materials resulting from the previous optimization: the aluminum holder and the brass screws. As expected, the overall distribution on the bolometer is similar to the one presented in Figure 34c, and is shown here in Figure 45. Most of the active part is within 5 mK from the working temperature, with the highest temperature mainly in the pads for the current and the voltage, where the YBCO is pristine and therefore in the fully superconducting state. Again, the configuration of the portable cryostat ensures a symmetric configuration with a more significant gradient along the Y-axis.

However, due to the two lines of symmetry of the new geometry, it affects equally the whole pattern.

a)

b)
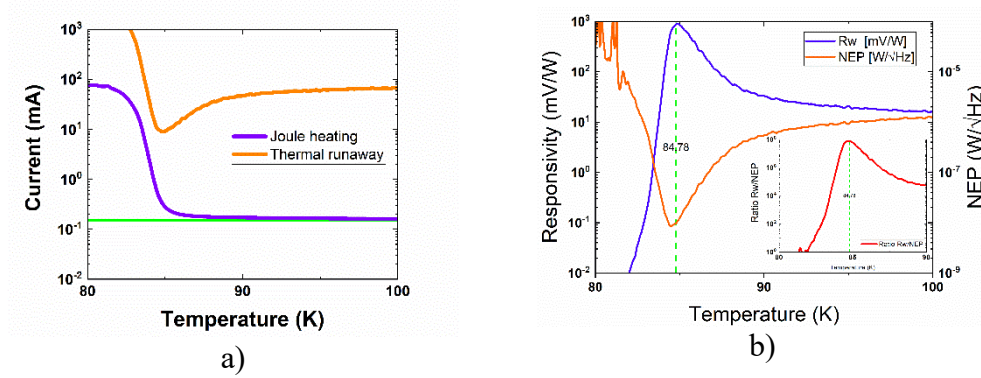
Figure 44: a) The study of bias current for the four-meanders configuration with the green line highlighting the chosen current, 0.15 mA and b) the study of the optimal working point with the responsivity (purple), the noise (orange) and their ratio (red)

The symmetry of the temperature is highlighted by its linear profile extrapolated at the center of an irradiated meander and of the whole bolometer, as reported in Figure 45. Once more, the temperature on the line passing through the center is lower than the one crossing the irradiated meander, as shown in Figure 46. From the border of the irradiated sector, reported as black dashed vertical lines in Figure 46, the difference is higher in the y-direction, 15 mK, and shallower along the x-axis, around 5 mK. A more considerable difference is present along the diagonal of the meander, with a variation in temperature of almost 20 mK.
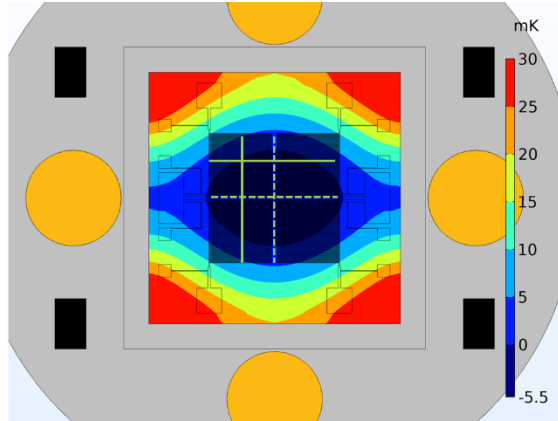
Figure 45: Temperature distribution at the equilibrium for the four-meanders layout. The green lines indicate where the linear profile of the temperature is extrapolated
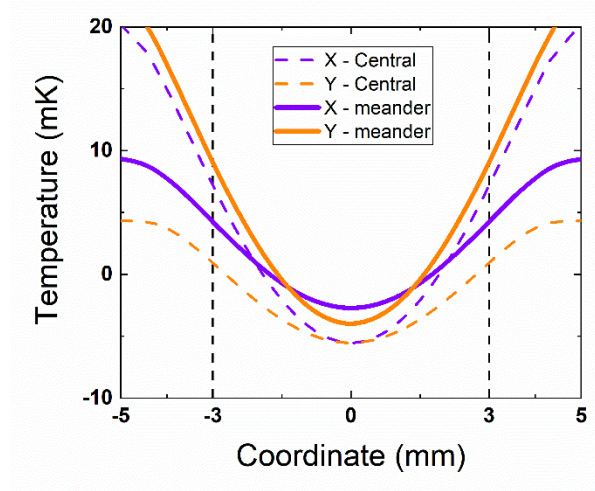
Figure 46: Linear profile for the line passing through the center of an irradiated meander (continue) and the center of the bolometer (dotted)

Once verified that the temperature distribution is still homogeneous in this new configuration, it is possible to employ COMSOL Multiphysics® to investigate the different responses to an external signal for the two layouts. As a result of the previous calculation, the working temperature is the same for both bolometers, 84.78 K, but the bias current is different because of the different resistance. The simulation reproduces an incoming signal with 1 µs duration and 1 mW of power. Figure 47 shows the result obtained for the two proposed patterns.
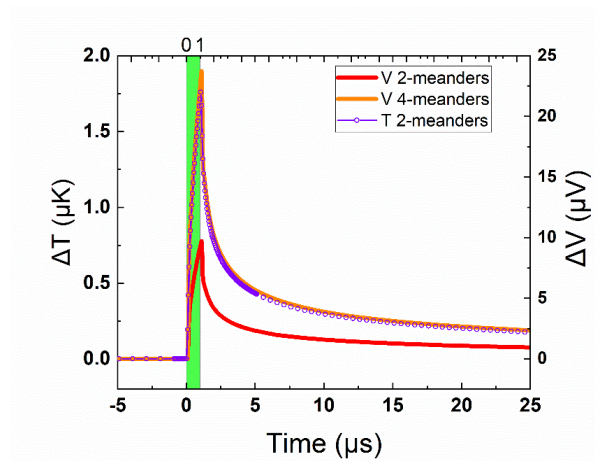
Figure 47: Response of the two bolometers, two and four meanders to a 1 µs signal

Despite the different areas of the active component, the resulting temperature variation is the same for both configurations, with differences well below the scale

of the graph. A more detailed analysis is required for the output voltage. As expected, the higher dR/dT associated with the four meanders layout provides a more significant signal, but is limited by the bias current, which is only 30% of the value used for the bolometer with two meanders. It results in a peak in the voltage 2.5 times bigger than the previous layout with the advantage of a low current flowing in the detector. The time constant of the four-meanders design is very similar to the previous configuration. The only variation is the meander area, roughly two times larger if only the irradiated meander is considered. For this reason, the difference is not readily appreciable in the timescale presented in Figure 47. A more significant difference will probably appear in detecting shorter signals when faster devices, such as HEBs, may be needed.

6. Design of YBCO based Hot Electron Bolometer

This chapter describes the design and the optimization of a YBCO HEB together with the realization of the prototype at the Chalmers University of Technology laboratory. The main idea is to use a microbridge with narrow dimensions to obtain a sub-nanosecond response of the device. Additional features, such as antenna and nanofabrication, have been simulated and preliminarily tested to maximize the matching with incoming signal in the range of THz and the electrical response of the detector. As a result, the future device should show a short response time and a higher sensitivity and to be frequency independent [239][240][241].

6.1 Superconducting HEB theory

The superconducting HEB has gained considerable interest since 1980 in the field of non-equilibrium superconductivity [242]. Indeed, the term "hot electron" refers to a state of non-equilibrium in which electrons in the bolometer are thermally decoupled from the phonon lattice and therefore have a different temperature. This is possible when phonons are well coupled with the substrate but weakly with the electrons [243]. In a superconducting HEB, both electrons and Cooper pairs can absorb a photon which impacts the film. When the photon is absorbed, highly energetic electrons are created by direct absorption or by the breaking of Cooper pairs. The resulting particles lose energy in the electron subsystem, interacting with other electrons and eventually breaking other Cooper pairs in an avalanche effect. This thermalization process happens faster than the interaction between electrons and phonons, and it leads to an increase in the electron temperature (T_e), which differs from the phonon one (T_{ph}) [244].

6.1.1 Thermalization process

The thermalization scheme of an HEB is shown in Figure 48, together with the interaction time of the subsystem. T_e and T_{ph} are the temperatures, C_e and C_{ph} are the heat capacities of the electron and phonon subsystem, respectively, while τ_{e-ph} and τ_{ph-e} are the characteristic time constant at which the heat exchange occurs

between electrons and phonons and vice versa. The thermalization time between electrons is τ_{therm}, which is usually so short compared to the other characteristic times that the process can be assumed instantaneous. τ_{esc} represents the escape time of phonons from the film to the substrate, the mechanism that definitively removes the heat from the system. The decoupling between electrons and phonons is assured by the fact that the energy transfer time constant from the phonon to the electron subsystem is greater than the escape time of phonons to the substrate [245].
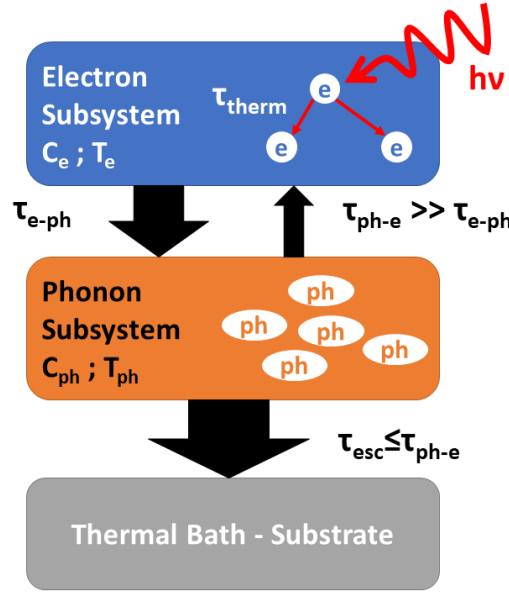
Figure 48: Thermalization process in an HEB. The electron (blue) and phonon (orange) subsystems are represented with the relative time constant

The energy backflow from the phonon lattice to the electron subsystem depends on the heat capacity ratio in (6.1). Since the phonon heat capacity below Debye temperature goes as $C_p \propto T^{-3}$, while the electron one is only inversely proportional to the temperature ($C_e \propto T^{-1}$) the condition $\tau_{ph-e} \gg \tau_{e-ph}$ is usually satisfied and hence the backflow of energy is negligible.

The thermalization of electrons is obtained with electron-electron interaction. It is boosted by the disorder of the crystal lattice and by temperature, for which scattering processes are enhanced [246].

$$\tau_{ph-e} = \tau_{e-ph} \frac{C_p}{C_e} \qquad\qquad 6.1$$

$$\tau_{e-ph} \propto T^{-m} \qquad\qquad 6.2$$

On the other hand, [247] reports that the interaction between electron and phonon follows the relation (6.2), in which the parameter *m* varies from 1 to 3. Therefore, it is convenient to work at high temperatures to achieve a fast response of the HEB.

For a YBCO film at 90 K, the phonon specific heat C_p is $0.65 \, J \, K^{-1} \, cm^{-3}$ and the electron specific heat C_e is $0.025 \, J \, K^{-1} \, cm^{-3}$ [248] and therefore $\tau_{ph-e} \approx 25 \, \tau_{e-ph}$.

It is also important to mention the electrothermal feedback, which was solved for the previous device with the double meander structure. This effect is due to the bolometer feeding current, which can impact and contribute to the power absorption, as described in [249][250], and therefore varies the resistance of the device. Its consequence will be analyzed during the characterization of the device, in which analytical correction can be applied.

6.1.2 The cooling process of the HEB

Depending on the major cooling process of the "hot-electron", HEBs can be distinguished in diffusion-cooled and phonon-cooled [251]. The diffusion mechanism is dominant when the length of the detector is smaller than the thermal diffusion length (L_{diff}), which is connected to the electronic diffusion constant of the material (*D*) as (6.3).

$$L_{diff} = \sqrt{D \cdot \tau_{e-ph}} \qquad\qquad 6.3$$

If a bolometer has dimensions comparable with L_{diff}, then it is thermalized mostly by metallic pads connected to the film [252]. L_{diff} is usually large in metals and ordered material such as niobium [253], while it is limited to hundreds of nanometers for cuprates, which is negligible compared to the other mechanism. From [248], the resulting L_{diff} for a YBCO film is in the order of 30 nm, and therefore a YBCO based HEB can be easily considered phonon cooled.

A bolometer is considered phonon cooled when the thermalization takes place mainly through the substrate, which acts as the absorber and the heat sink. In the case of thin films, it is possible to estimate the escape time of the phonon as in (6.4), where *d* is the thickness of the film, α is the transmission coefficient of the phonon from the superconductor to the substrate, and *u* is the speed of sound in the film

[254]. For example, considering a 100 nm YBCO film, the phonon escape time is around 5 ns, orders of magnitude larger than other thermalization time, which is in the order of picoseconds [255][245].

$$\tau_{esc} = \frac{4d}{\alpha u} \qquad\qquad 6.4$$

To reduce the response time of the HEB, it is worthwhile having a thin superconducting film and a good matching between the superconductor and the substrate phonon spectra.

6.1.3 Two-temperature model

The non-equilibrium state in a HEB can be described with the so-called two-temperature (2T) model [256]. This model can be applied when the working temperature is close to the T_C. The phonons and the electrons can then be described by a normal state distribution with two different temperatures established evenly and instantaneously in the whole subsystem. The energy gap is strongly suppressed in proximity to the T_C, such as the Cooper pair concentration, and the specific heat of electrons varies more significantly than in the normal state. These assumptions, together with, $\tau_{ph-e} \gg \tau_{e-ph}$, allow describing the HEB with the linear equations (6.5) and (6.6) for the electron and phonon subsystems, respectively.

$$\frac{dT_e}{dt} = \frac{W(t)}{C_e} - \frac{T_e - T_{ph}}{\tau_{e-ph}} \qquad\qquad 6.5$$

$$\frac{dT_{ph}}{dt} = \frac{T_e - T_{ph}}{\tau_{ph-e}} - \frac{T_{ph} - T_b}{\tau_{esc}} \qquad\qquad 6.6$$

The external perturbation *W(t)* is assumed absorbed only by the electron subsystem. This model works only for pulses with duration in the order of τ_{ph-e}, approximately 50 ps for YBCO [257], and it does not consider the power dissipated by the bias current.

The hot-spot model was developed to consider larger signals and describes the bolometer as a 1-dimension system for which the electron temperature varies along the bridge. It is assumed that the power of the local oscillator is absorbed uniformly in the whole bridge, while the joule heating is dissipated only in a small hot spot region at the center of the bridge [258]. Furthermore, the phonon thermalization between the film and the substrate is considered instantaneous ($\tau_{esc} = 0$). Under

these conditions, the system can be described inside the hot-spot by (6.7) and outside by (6.8). Here K is the thermal conductivity of the film, j is the bias current density in the bridge, ρ the resistivity in the normal state and P_{RF} the power absorbed per unit volume. Despite the simple model, the two equations well reproduce experimental I-V curves and results obtained with more accurate models [259].

$$-K\frac{d^2 T_e}{dx^2} + \frac{C_e}{\tau_{e-ph}}(T_e - T_b) = j^2\rho + P_{RF} \qquad\qquad 6.7$$

$$-\frac{Kd^2 T_e}{dx^2} + \frac{C_e}{\tau_{e-ph}}(T_e - T_b) = P_{RF} \qquad\qquad 6.8$$

The time of the YBCO photoresponse has been investigated for a long time and several experiments confirm the fast evolution of the measured voltage as presented in [260]or more recently in more complex structures as in [261][262].

6.1.4 RT model

When the HEB works at a temperature well below T_C, the 2T model is not valid anymore. It is necessary to use the RT model, from its developer Rothwarf and Taylor [260], to describe the non-equilibrium process of breaking and recombination of Cooper pairs. In this model, most electrons are combined into Cooper pairs and obtain energy slightly above the superconducting energy gap during the thermalization. Therefore, it is more beneficial to use a number density rather than a non-equilibrium energy distribution function. The new equations consider the excess of quasiparticles (Δn_q) and of 2Δphonons, (Δn_p). The 2Δphonon represents the phonons emitted by the recombination of Cooper pairs, which have a minimum energy of 2Δ and, hence, can break another couple. τ_{Br} represents the time between the creation of a 2Δphonon and a pair destruction and τ_R is the quasiparticle recombination time. The thermalization is considered instantaneous in the quasiparticle and the phonon subsystem.

$$\frac{d}{dt}\Delta n_q = -\frac{\Delta n_q}{\tau_R} + \frac{2\Delta n_p}{\tau_{Br}} \qquad\qquad 6.9$$

$$\frac{d}{dt}\Delta n_p = -\frac{\Delta n_p}{\tau_{Br}} - \frac{\Delta n_p}{\tau_{es}} + \frac{\Delta n_q}{2\tau_R} \qquad\qquad 6.10$$

Eqs. 6.10 and 6.11 describe the evolution of the quasiparticle excess Δn_q when a photon with an energy larger than 2Δ is absorbed by a film maintained well below T_C. When the Cooper pairs are destroyed, the number of electrons increases, resulting in a variation of the kinetic inductance as described in (6.11) and (6.12). Here F_{sc} is the fraction of superconducting electrons, n_0 is the total concentration of quasiparticles, $n_q(0)$ and n_q are respectively their equilibrium and instantaneous concentration [263]. The variation of F_{sc} can be calculated through 6.11 by the variation of kinetic inductance $L_{kin}(t)$, linked to the equilibrium value of kinetic inductance L_0.

$$L_{kin}(t) = \frac{L_{kin}(0)}{F_{sc}} \; ; \; L_{kin}(0) = \frac{\mu_0(\lambda_L^2)}{d} \qquad\qquad 6.11$$

$$F_{sc} = \frac{(n_0 - n_q)}{n_0} \; ; \; n_q = n_q(0) + \Delta n_q(t) \qquad\qquad 6.12$$

Since the bias current must remain the same, when a certain amount of Cooper pairs has been destroyed, the remaining fraction accelerates to maintain the current constant. Due to their inertia, the variation of kinetic inductance generates a voltage drop across the film as in (6.13), which can be directly detected.

$$V_{kin} = I \cdot \frac{dL_{kin}}{dt} \qquad\qquad 6.13$$

6.2 Design optimization

The design of the HEB is developed from a similar sample used for the TEB: a MgO substrate with dimension 10 mm x 10 mm x 0.5 mm over which is deposited a 100 nm thick YBCO film. The smaller thickness of the film brings two main benefits: a lower heat capacity and, especially, a larger resistance. The idea is to have a coplanar guideline (CPW) to feed the microbridge at its center, which acts as the HEB. This configuration limits the electromagnetic interactions between the ground and the microbridge and allows a fast readout with controlled losses.

The HEB is expected to have a response time in the order of ps and the sudden change in the output signal can only be adequately read if there is a good impedance matching with the measurement equipment. For this reason, the scattering parameters are studied for frequencies ranging from 0 to 10 GHz to match the 50 Ω

of characteristic impedance (Z0). The evaluation started from analytical calculations on simple geometry and was then refined with the SONNET® software.

Preliminary sizing of the coplanar waveguide is performed with a simple tool [264] which estimates both the Z0 and the effective dielectric constant (ϵ_{Eff}) for simple CPW as reported in Figure 49.

For obtaining the input impedance and the effective dielectric constant, in the tools are inserted the relative permittivity of the substrate ϵ_R, set as 9.6, and its thickness *h*, set at 0.5 mm, together with trace width (*W*) and the ground plane spacing (*S*) of the CPW. The metallic plate is considered a perfect conductor with a negligible thickness. To reduce the influence of the sensor holder on the electromagnetic field distribution on the superconductor, the relation *h=2S* has been respected [265]. The preliminary results are a trace width of 0.5 mm and a ground plane spacing of 0.25 mm, resulting in a Z0 of around 55.5 Ω and an ϵ_{Eff} of 4.7. From this starting point, more sophisticated simulations are run with the introduction of the microbridge and some possible geometries acting as antennas.
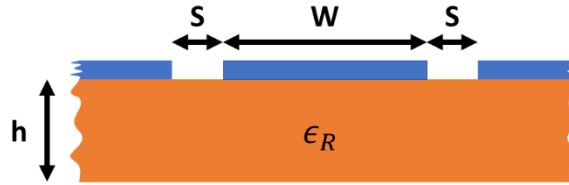
Figure 49: Preliminary geometry and relative parameters

6.2.1 Calculation with SONNET®

To obtain a good characterization of the device, the software SONNET® is used for more complex simulations. SONNET®, distributed for the first time in 1983, is used for analyzing high-frequency planar circuits employing the Method of Moments based on Maxwell's Equations [266]. SONNET® works on multiple layers, metals or dielectric, and finds the voltage employing the Fast Fourier Transform (FFT) on the current on each layer. This operation is done simultaneously on each mesh element while setting the voltage drop to zero everywhere in the metal. The geometries implemented in SONNET®, thin conductive layer over bulk dielectric, well suit the HEB structure. The bolometer can be reproduced through a 2D conductive metal layer over a massive insulating substrate, employing the surface impedance to define the metal losses. This specific geometry, with dimension 10 mm x 10 mm, is drawn over a larger square to reduce

the influence of the wall in the resonance peak, and includes input and output ports connected through feedlines and to limit possible artefacts in the extrapolation of the results.

The HEB is reproduced using different dielectric layers and only one metallic material (modelling the YBCO). From top to bottom, as shown in Figure 50, they are air, YBCO, MgO and Kerafol CT800. Above and below, the free space and aluminum, set as a ground, are defined. The thickness, the conductivity, the dielectric constant and the tangent loss are reported in Table 7 for the dielectric layers [267][268]. The thickness of the air is set to 3 cm, enough to avoid any interactions within the upper components. Therefore, it is possible to define the free space without impacting the accuracy of the simulation. Similarly, the Kerafol CT800 is inserted to replicate the vacuum grease below the MgO substrate, which further isolate the superconducting layer from the aluminum ground.

Figure 50: Schematic view of the layers in SONNET®

Table 7: Properties of the dielectric layers

Material	Air	MgO	Kerafol CT800
Thickness [mm]	30	0.5	0.1
Conductivity [S/m]	0	0	0
ε	1	9.6	5.3
Tanδ	0	$5 \cdot 10^{-5}$	$8 \cdot 10^{-3}$

The YBCO is the only metallic layer and it is placed above the MgO substrate. The trivial approach of defining it as a perfect conductor is avoided; the high operation temperature, close to T_C, the effect of kinetic inductance and the relatively small dimension of the circuit required a more complex definition. The HEB will work in correspondence with the T_C to maximize the responsivity, therefore the assumption of null electrical resistance and surface inductance is not fully valid anymore. Similarly, the London penetration depth at these temperatures is not negligible anymore if compared with the smallest dimension of the circuit. For these reasons, the film is defined as a general metallic layer, which includes in its properties the resistivity at low frequencies (R_{DC}), the losses at high frequency (R_{RF}), the surface reactance (X_{DC}) and the surface inductance (L_S). R_{DC} is taken from literature for frequencies and temperatures comparable with the operating one [269], while R_{RF} and L_S are calculated with the formulas (6.14) and (6.15) [270]. The numerical values are reported in Table 8.

$$R_{RF} = \frac{1}{2}\omega^2\mu_0^2\lambda_L(T)^3\sigma_N \cdot \left(\frac{\mu_n}{\mu_n+\mu_s}\right) \qquad\qquad 6.14$$

$$L_S = \mu_0 \cdot \lambda_L(T) \qquad\qquad 6.15$$

Above, ω is the frequency, $\lambda_L(T)$ is the London penetration depth for the YBCO, set as 150 nm, σ_N is the conductivity in the normal and the last term represents the fraction of normal carrier for temperature nearby T_C [271].

Table 8: Properties of the YBCO as a metallic layer

YBCO superconductor

R_{DC}	$10^{-4}\Omega/sq$
R_{RF}	$1.35 \cdot 10^{-26} \cdot f^2\frac{\Omega}{sq} Hz^{0.5}$
X_{DC}	0
L_S	$\mu_0 \cdot \lambda(T) = 0.19\,pH/sq$

6.2.2 Coplanar waveguide optimization

The preliminary study aims at finding the scattering matrix for a CPW for different parameters of W and S. An adaptive sweep over 200 target frequencies in the range 0-10 GHz is used for all the simulations limiting the computational time but still providing accurate results. The major constrain is the ground pacing dimension, which must be kept lower than the substrate thickness. Various combinations of S and W are investigated, with S varying between 0.05 mm to 0.25 mm with 0.05 mm step and W varies from 0.1 mm to 1.0 mm with steps of 0.1 mm. The input impedance, module, real and imaginary parts, are reported for the best configuration in Figure 51 and the final configuration in Figure 52. A resonance peak, probably due to the square configuration, is present around 5.5 GHz, but it does not affect the overall performance of the CPW.
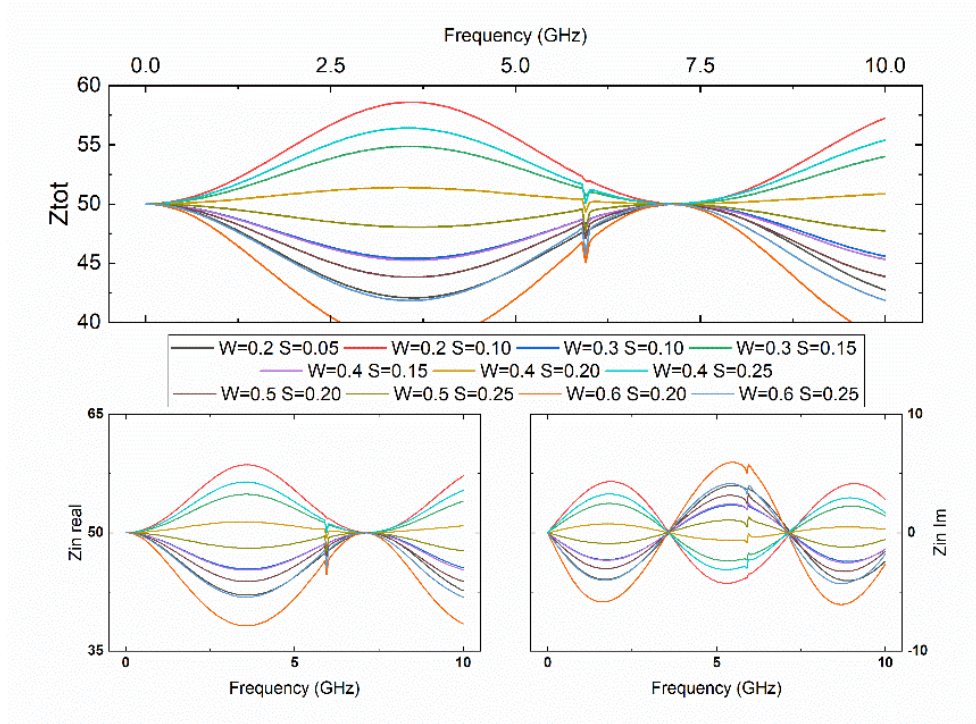
Figure 51: Input impedance for some configurations of the CPW optimization study
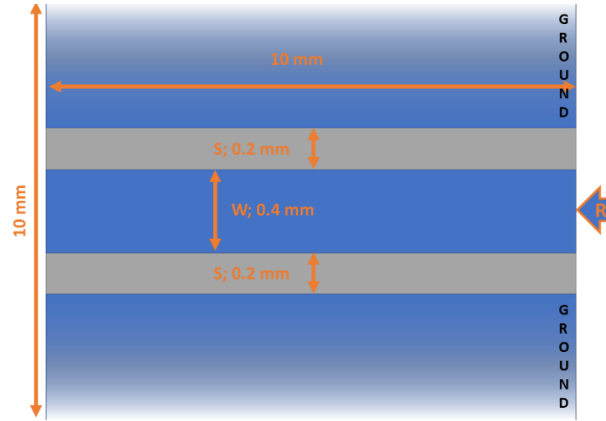
Figure 52: Schematic view of the CPW with the chosen values of W and S (not in scale). The substrate, MgO, is colored in grey, while the superconductor, YBCO, in blue

The best result presents a trace width which is double the plane spacing (W=2S). Two configurations, the one with S=0.2 and W=0.4 mm and the other S=0.25 mm and W=0.50, present the most homogenous Z. Between them, the configuration W=0.4 mm and S=0.20 mm has been chosen to reduce the chance of electromagnetic interference with the HEB through the reduction of the ground spacing.

6.2.3 Microbridge design

After defining the dimension for the CPW, the microbridge at its center is designed. The structure has a dimension of 5 µm x 10 µm; thus a reduction from 400 µm to 5 µm is necessary for the trace width. Different configurations have been simulated to find the one that has the minimum impact on the Z0. In this analysis, the tapering length varies from 0.2 mm to 9.0 mm, as shown in Figure 53.
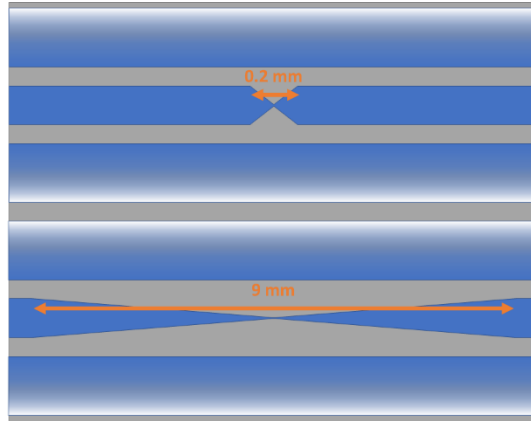
Figure 53: The two extreme configurations, 0.2mm above and 9.0 mm below, for the study of the tapering of the CPW (not in scale)
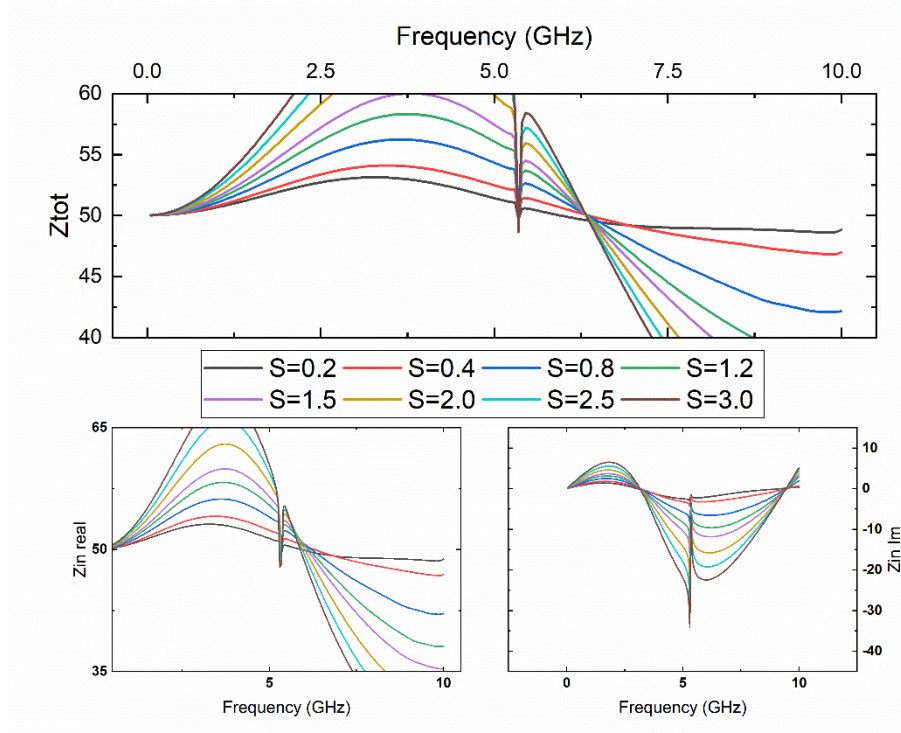
Figure 54: Input impedances for tapering length of the CPW from 0.2 mm to 3.0 mm

The results are presented in Figure 54 only for lengths up to 3.0 mm because of the evident trend: the best options are the ones with the shorter tapering. The resonance peak previously noticed is slightly shifted at a lower frequency, around 5.25 GHz, but still, it does not impact the performance of the microbridge. The

length of 0.4 mm has been chosen to have a more symmetrical structure: the tapering length is equal to the trace width.
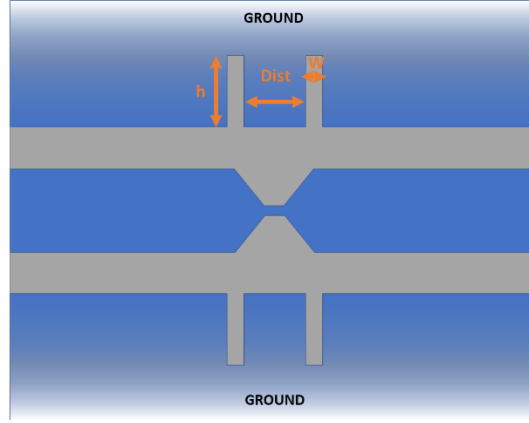
Figure 55: Structure of the double slot antenna with its parameters under study: the height (h), the distance between antennas (Dist), and the width (W) (not in scale)
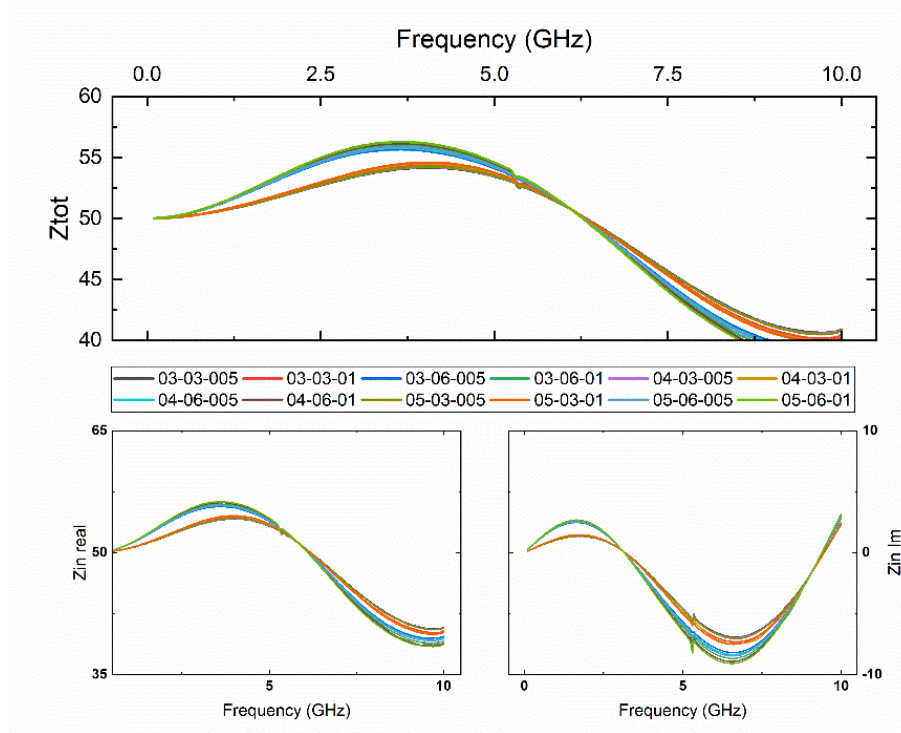
Figure 56: Input impedance for the studied configurations. The values represent the distance (Dist), the height (h), and the width (W)

The effect of a double slot antenna has been studied for different geometrical parameters shown in Figure 55. This structure aims at focusing the THz radiation

in the microbridge and, ideally, to select polarized waves. Figure 56 shows the effect of the antenna for different slots distances (Dist), heights (h) and width (W). The structures, located on the ground plane of the original CPW, have a minimum effect on the input impedance, although this effect is more substantial for the longer antennas (larger h).

6.2.4 Electromagnetic Interaction with THz radiation

The study of the input impedance performed with SONNET® gives good results for the readout of the microbridge, but the software does not provide any information on the interaction between an incoming wave and the detector. Therefore, a preliminary analysis is implemented with COMSOL Multiphysics® using the *Electromagnetic Waves, Frequency Domain* module.

The physics calculates the scattered field produced by an incoming wave using 6.16 and 6.17. Here are present the relative permeability, μ_r, the wavenumber of free space, k_0, and the relative permittivity σ in the first equation, and the electric field is defined in the second one as the sum of the scattered and the incoming one in at the boundary of the simulated domain.

$$\nabla \times \mu_r^{-1}(\nabla \times \boldsymbol{E}) - k_0^2 \left(\epsilon_r - \frac{j\sigma}{\omega \epsilon_0} \right) \boldsymbol{E} = 0 \qquad 6.16$$

$$\boldsymbol{E} = \boldsymbol{E}_{SC} e^{-jk(\boldsymbol{n} \cdot \boldsymbol{r})} + \boldsymbol{E}_0 e^{-jk(\boldsymbol{k} \cdot \boldsymbol{r})} \qquad 6.17$$

Different kinds of waves can be selected for the study: Gaussian beam, linearly polarized and user-defined. Among them, the linearly polarized one is used to see the effect of the polarization along the x and y-axis on the distribution over the device. The maximum background electric field amplitude is set at 1 V/m for every simulation. The boundaries are transparent for scattered and incoming plane waves, removing the effect of scattered artificial components. Unlike the previous simulation, the YBCO film is treated as a perfect conductor, clearly simplifying the simulation but without introducing substantial discrepancy from an excellent conductor.

The simulations consider a simplified geometry of the bolometer and only a limited number of discrete frequencies. The main limitation in these models is the

enormous number of elements required to well define the interaction between the device and the incoming wave. Indeed, to obtain a reliable result, the mesh size needs to be a fraction of the wavelength; in particular, to resolve the wave correctly, at least five second-order elements per wavelength are necessary. Since the THz radiation has a submillimeter wavelength in the vacuum and in the order of micrometers in the MgO and YBCO, the overall device must be limited in size to be discretized and analyzed. Instead of simulating the whole volume of the device, 10 mm x 10 mm x 0.5 mm, the simulation is limited over a surface of 2 mm x 2 mm and considers a substrate that is only 0.25 mm thick. To further reduce the number of elements, the space above and below the bolometer is equal to ten wavelengths: it limits the surrounding domain and the number of elements associated, and grants that the device is hit by the wave at its maximum for each frequency, making the result comparable between them.

Because of the size and the time required by the simulation, only three frequencies are analyzed: 0.5, 1.0 and 1.5 THz. Higher frequencies, kinked with smaller mesh, are not feasible because of the computational cost due to the number of mesh element. To obtain comparable results, the mesh element is maintained constant for all the simulations with the size corresponding to the more stringent requirement, i.e., 1.5 THz.
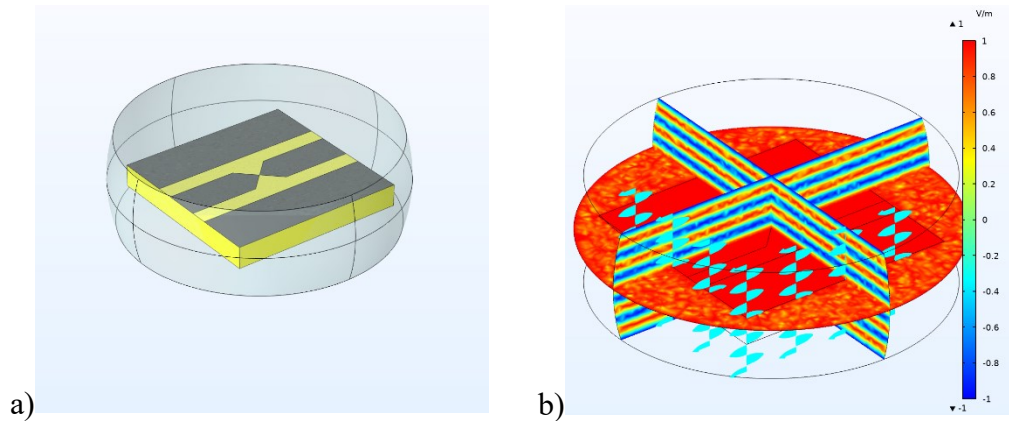
Figure 57: a) Reduced geometry used for the electromagnetic study; the MgO substrate is yellow, the YBCO film black and the surrounding air in grey. b) A background incoming wave, linearly polarized along x; the plane corresponding to the bolometer surface is at the maximum of the incoming wave.

The analyzed layouts are the microbridges with and without antennas. The geometry is shown in Figure 57a, and an example of an incoming wave is shown in

Figure 57b. The whole surface is on the peak of the electric field of the wave and the cyan waves represent the polarization of the wave, in this case along x.

The result, summarized in Figure 58, shows the effect of the antenna on focusing the wave and obtaining a selective matching with the polarization. The images show the norm of the electric field on the surface of the detector. The first row (Figure 58a-c) shows the effect of an incoming wave polarized along x, parallel to the guidelines, for the geometry without antennas, for frequencies of 0.5, 1.0, and 1.5 THz. The second row (Figure 58d-f) presents the same wave interacting with the layout, including the antennas. The last two rows show the wave in the y polarization for the geometry without (Figure 58g-i) and with antenna (Figure 58j-l) for the same frequencies, i.e., 0.5, 1.0, and 1.5 THz. For all the surfaces, the scale of the electric field is kept constant to highlight the differences between them.

In these studies, a pattern is visible in any structure. It shows a periodicity that decreases with the frequency, and it is probably connected with the substrate dimension and geometry. Therefore, it will be necessary to perform the simulations in a more powerful machine that allows considering the whole dimension of the detector before confirming the obtained results. This preliminary analysis proves that the electric field is confined in the superconductor, and it is concentrated in the microbridge thanks to the bow-tie structure created by the CPW tapering. Similar configurations are present for the same frequencies and polarizations: at 500 GHz, the focusing is higher with polarization along x, while for higher frequencies is better for polarization along y. The frequency strongly affects the electric field distribution while the antennas play a minor role. It does not affect the focusing of the incoming radiation with an effect just barely visible for the y polarized wave.
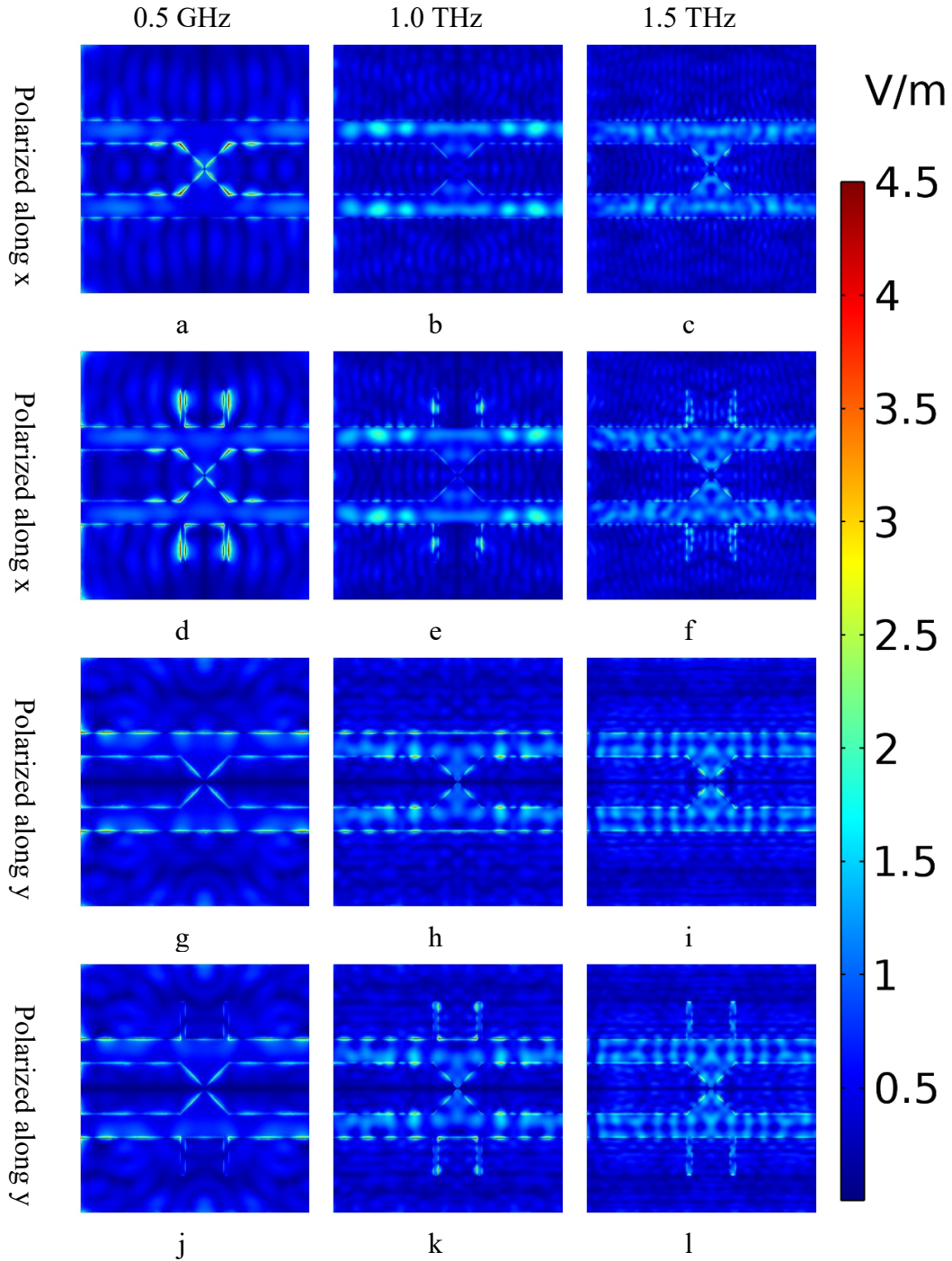
Figure 58: Module of the electric field for the layout with and without antenna for three frequencies: 500 GHz (a, d, g, and j), 1.0 THz (b, c, h, and k), and 1.5 THz (c, f, i, and j). The first two rows show a linearly polarized wave along x, while the last two along y.

Concluding, the bow-tie antenna structure created from the tapering of the coplanar guideline provides a good focus of the incoming radiation and is weakly

affected by the polarization. The frequencies strongly impact the distribution while the antennas show negligible effects, mainly concentrated on the structure and not on the microbridge.

6.3 Physical device

Different structures have been fabricated on the basis of the obtained results of the previous simulations. The prototypes are based on the 5 μm x 10 μm microbridge with some nanofabrication, which aims to improve the detectivity of the device. The value of 100 nm used in the previous studies, in which any dimension could have been implemented, is dictated mainly by the manufacturing process. Thinner samples are more difficult to realize and are more subject to surface modification which would influence the overall sample. A good trade-off between easy manufacturing and a suitable value for a large resistance is found at 100 nm, also the thickness of the THEVA sample, which was available in addition to the one fabricated at Chalmers. The comparison between the two samples highlights the great achievement obtained during the deposition through pulsed laser deposition, for which the characterization gives better results. Finally, the desired time constant of the new device is based on the HEB phenomenon; hence, the advantage of reducing the thickness for achieving a shorter time constant does not compensate for the manufacturing and the stability of the sample with more YBCO. Microbridge mask

The manufacturing of the devices is based on the fabrication procedure developed at the Chalmers University of Technology. Here, Electron Beam Lithography (EBL) is used to define the etching mask, then used to transfer the pattern to the YBCO film during Ar ion milling. While EBL allows minimum features of c.a. 20 nm, the process is limited by the ion milling combined with the thickness of the films. Features, e.g., trenches and holes, with dimensions comparable to the film thickness are not entirely etched during the ion milling. Therefore, the major limiting factor is the thickness of the YBCO film, which must be lower than the minimum feature to ensure a correct etching of the superconductor. The ratio between the feature and the thickness should thus be higher than 2. Also, long and thin pits may result in an incomplete YBCO removal at their end, impacting the quality of the device [272]. Figure 59 shows the geometries realized and characterized at Chalmers with the process described in the following chapter.

The manufacturing process dictated the main constraint in the fabrication of the serpentine. Indeed, the space between two meanders of YBCO is twice as large as the thickness of the superconducting film. This strongly limits the risk of uncomplete etching of the cuprate, especially near the end of the gap, which would result in a performance loss of the device. Once the minimum distance between the meander of the serpentine, the two analyzed devices has been chosen to maximize the detectivity (Figure 59b) and the responsivity (Figure 59c). The large serpentine has a larger area exposed to the radiation, therefore, the detectivity, directly proportional to the square root of the area, is increased. However, this decision is deleterious for the responsivity, since it is proportional to the resistance related to the section and the film length. To obtain a device that maximizes the responsivity, a smaller serpentine is chosen, 100 nm of width, resulting in a larger resistance combined with a suitable fabrication process.
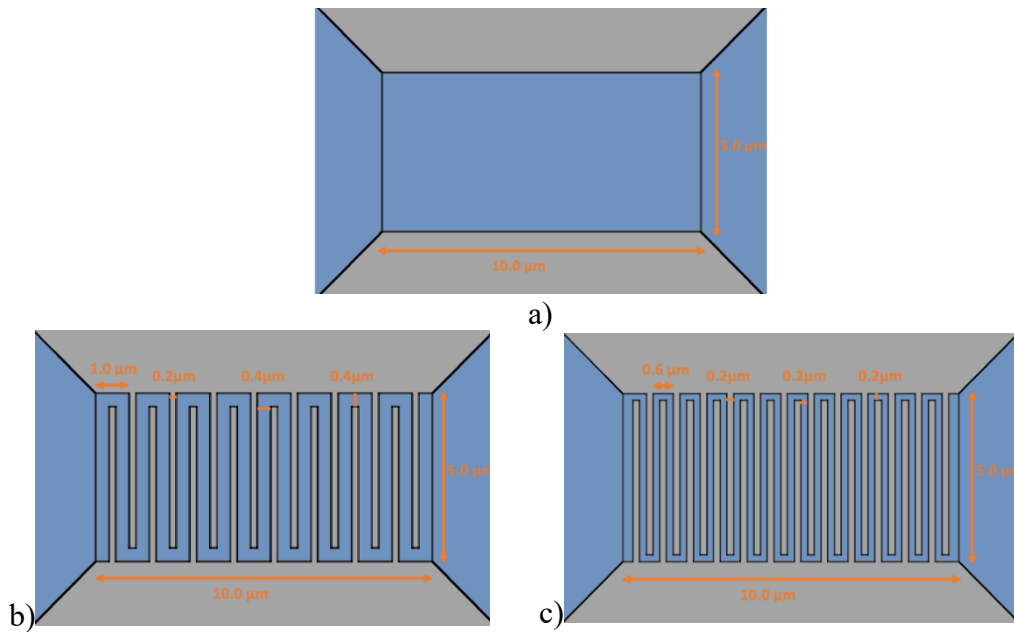
Figure 59: Layout of the microbridge (a) large serpentine (b) and tiny serpentine (c) and relative quote

6.3.1 Fabrication

The process has two main steps: the deposition of the YBCO film and its patterning through lithography. Figure 60 schematically shows the overall process: the deposition of the YBCO, thin film and the gold strips (1), and the carbon film (2), then the mask definition by mean of EBL and the subsequent chromium evaporation (3-4), which allows transferring the pattern to the carbon mask with

reactive ion etching in O_2 (5). Finally, the etching of the uncovered YBCO (6) and the removal of the remaining carbon (7). All the steps are detailed below.
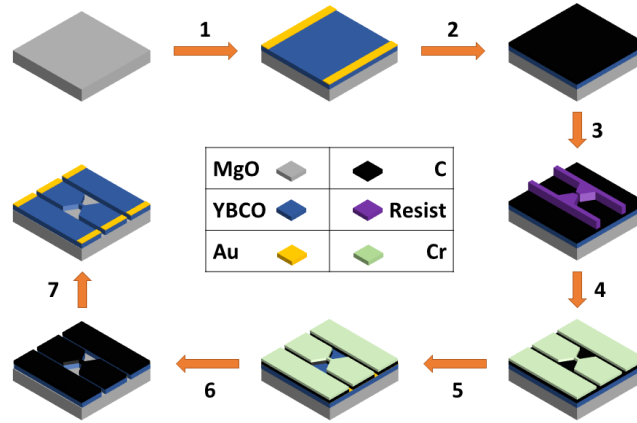
Figure 60: The process of deposition and lithography of a YBCO film

The YBCO is grown by Pulsed Laser Deposition (PLD) on a MgO substrate, usually 5 mm x 5 mm x 0.5 mm, [110] oriented. These dimensions allow a homogenous deposition of the YBCO and the crystal orientation grants epitaxial growth of the superconductor. The parameter presented below permits slightly overdoped material, resulting in a slightly lower T_C but a more stable film during fabrication.

PLD is used to depose of the YBCO thin film, step 1. As shown in Figure 61, a pulsed laser ablates a YBCO target and the released particles are deposited on the substrate. Before the YBCO deposition, the substrate is cleaned chemically, using Isopropyl Alcohol (IPA), and physically, with ultrasound vibration. The deposition takes place at 760 °C in an O_2 atmosphere at 0.6 mbar for a time that varies with the required thickness. The temperature helps the epitaxial growth of the YBCO while the oxygen environment is required to reach the desired doping. The energy of the laser is measured just before entering the chamber, and it is set at 55 mJ (spot size of 4 mm^2) with a rate of 6 Hz. It allows a homogenous deposition on the substrate, which is located at a precise distance from the precursor. Once the deposition is finished, the sample remains in the O_2 atmosphere at 650 °C to stabilize the oxygen content in the YBCO. To reduce the parasitic contact resistance and obtain better measurements, two 1 mm wide strips of 40 nm thick gold are deposited at two opposite borders of the sample through magnetron sputtering.
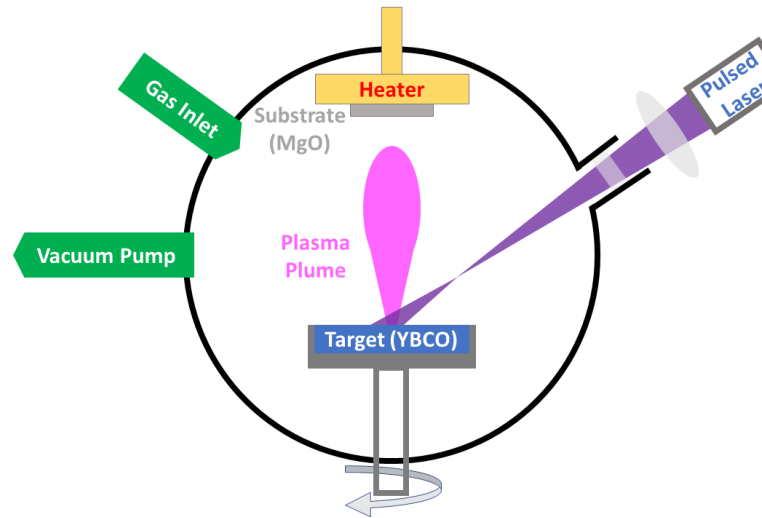
Figure 61: Pulsed Laser deposition process for deposition of YBCO films

The second step is to deposit a carbon layer with a thickness comparable to the YBCO film to protect the superconductor during the lithography process and act as a physical mask during Ar ion milling. The deposition takes place in another PLD machine at room temperature and high vacuum with high laser energy in the order of 100 mJ. A different PLD system is required to reduce the contamination inside the PLD chamber dedicated to the YBCO due to the small carbon particles that are difficult to remove.

Afterwards, two negative photoresists are deposited on the sample by spinning. The bottom one is made with MMA8.5 MAA EL4, while the upper is a combination of ARP6200 and IPA with a 1:3 ratio. Both the resists are applied on the sample and spun at 6000 rpm before being baked at 95 °C for 5 minutes. This double layer improves the result of the lift-off thanks to the undercut formed during development.

The EBL process, performed with the JEOL JBX 9300FS machine (100 kV), is used to expose the resists. The mask, previously created with a CAD software, is converted in instruction for the system. This ensures no open features and calculates the correct exposure, i.e., proximity effect correction. Since electrons scatter in the resist, the dose (charge per unit area) differs from the boundary to the center; this is considered when calculating the resulting dose in the whole geometry. Also, different areas are defined depending on the feature: smaller ones are exposed with a low current beam, with a beam spot of 4 nm allowing minimum features of 30 nm, while the rest is exposed with a beam spot of 40 nm corresponding to high

current beam, i.e., a larger aperture. Each area is excited separately and the matching between them is achieved by a pre-alignment of the sample.

The development of the resist defines the final structure of the device; it is done using first Oxylene 96% and then MIBK:IPA 1:3, both for 35 seconds each at room temperature, step 3. Then, 12 nm of chromium are deposited on the sample and the remaining resist through Physical Vapor Deposition (PVD). Finally, the remaining resist and the chromium deposited by lift off on it is removed in a bath of developer 1165 for 10 minutes at 75 °C, followed by 2 minutes of ultrasonication, step 4.

The chromium mask is transferred to the carbon layer, step 5, by O2 plasma Reactive Ion Etching (RIE). To remove the carbon without damaging the YBCO film, RIE works with a power of 50 W in an O_2 environment at a pressure of 100 mTorr. Finally, profiling is done to check the result of the etching, which shows a slightly thinner layer of carbon and chromium, i.e., around 100 and 10 nm, respectively.

Then, the sample is etched with Ar^+ ion milling at room temperature with a beam current density of 30 $\mu A/cm^2$. During the procedure, the chromium layer is etched completely, as well as the YBCO not protected by the carbon mask, step 6. This step is improved with a neutralizer that avoids charging effects in the substrate. The final stage, step 7, consists of removing the remaining carbon layer through RIE.

6.3.2 XRD characterization

The X-ray diffraction (XRD) of a THEVA film is performed at Chalmers University of Technology. It is performed on a 100 nm film already patterned with gold stripes at the border. Although these conditions are not optimal for XRD, the results allow determining the oxygen content of the film. Figure 62 shows the results of the XRD with the peaks of the plane (00n) in which n varies from 0 to 7. These values permit to extrapolate the average length of the c-axis by mean of the Bragg law and, from it, the oxygen doping of the film.
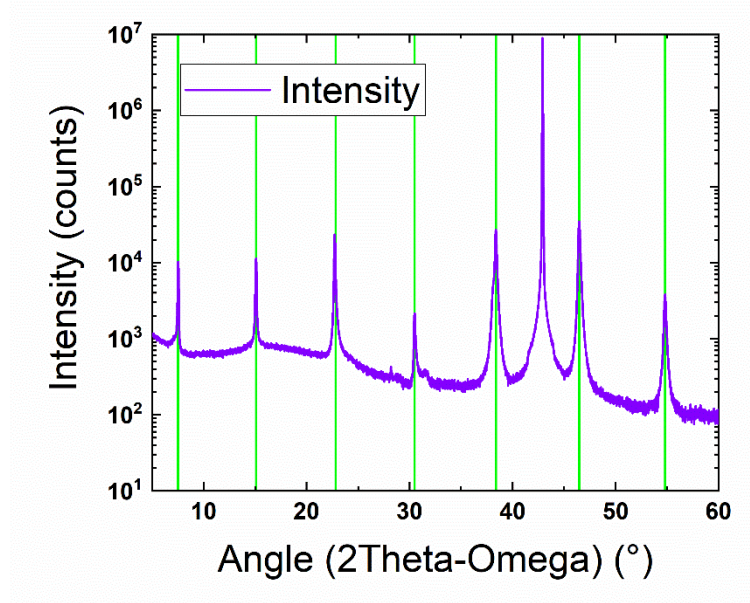
Figure 62: XRD for the THEVA sample, 100 nm YBCO film on MgO. The peaks are highlighted in green

The length of the c-axis is 11.716 Å, corresponding to a doping level (7-δ) of around 6.64 [273].

6.3.3 Sample imaging, optical and SEM

The structures shown in Figure 59 are fabricated with the EBL technique. Depending on the dimension, they are characterized through an optical or a Scanning Electron Microscope (SEM). The simple microbridge has been fabricated with the double antenna, shown in Figure 63 with the relative dimensions. The antennas have the height and the distance of 300 μm and a width of 50 μm. The measures differ by around 1% from the nominal values, except for the microbridge. Here, the mismatch reaches 4%, which can be attributed to the difficulty operating with the optical microscope at this magnification.
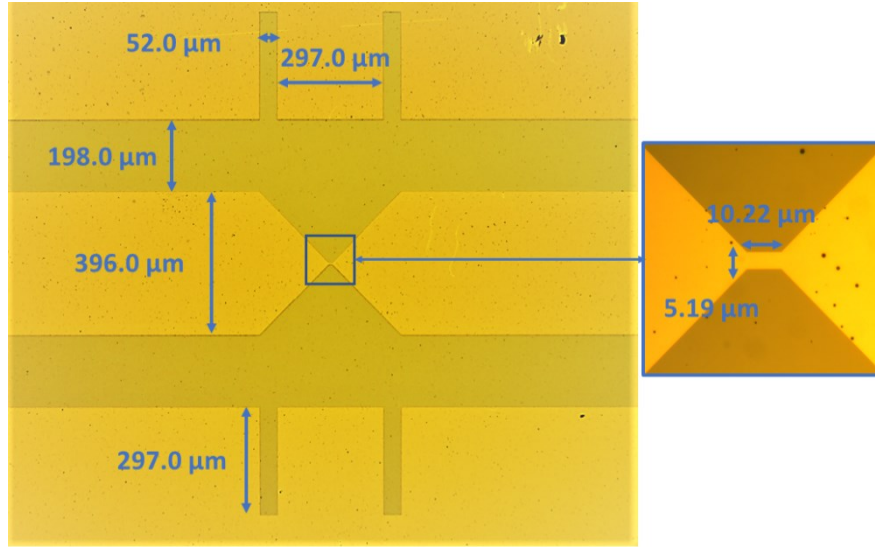
Figure 63: Optical image with quotes of the microbridge and its antennas

Due to the small features of the two nanofabricated serpentines, they are examined with the SEM. With a width of 400 nm, the larger serpentine has been fabricated on a 50 nm thick film and analyzed before the Ar ion milling, Figure 64a, while the thinner one has been fabricated on a THEVA film with a thickness of 100 nm and visualized after the etching Figure 64b. A difference between the two figures can be observed. Before the etching, when the chromium mask is still on the sample, the contrast is higher, and the corners are sharper. After the physical etching, the corners are rounder, especially inside the dip, and the dirtiness is more evident because of the lesser contrast between the MgO and the YBCO film.
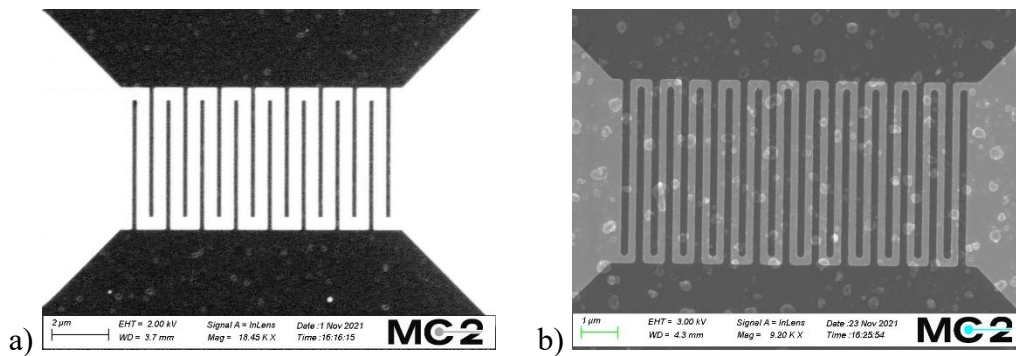
Figure 64: SEM image of a) the large serpentine on 50 nm thick film and b) the tiny serpentine on the THEVA film

6.3.4   RvsT characterization

The RvsT curve of the devices is measured in a dipstick setup plunged in liquid nitrogen. The device is mounted on a chip carrier and connected to the measurement setup as shown in Figure 65 to measure its resistance R. The temperature T is simultaneously measured near the device with a calibrated diode, which is also mounted on the same chip carrier.
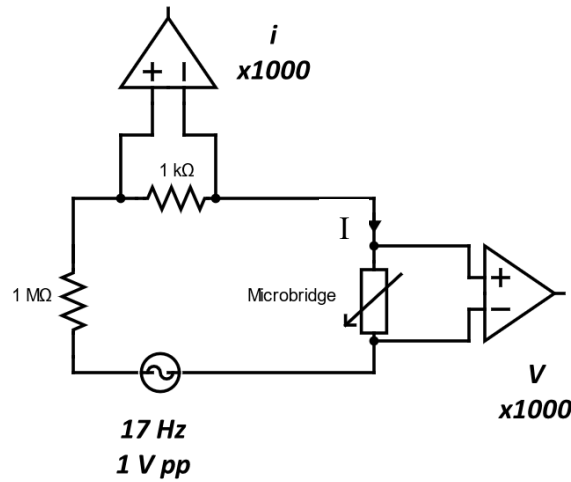
Figure 65: Measurement circuit for the microbridge

The Waveform Generator is a KEYSIGHT 33500 B series which provides a triangular waveform with a frequency of 17 Hz and a value of 1 Vpp. The resistance placed in series with the generator is much higher than the sample resistance and thus determines the current flowing in the circuit. For the microbridge measurement, it is set at 1 MΩ to obtain a current of around 1 µA. Of the two low noise amplifiers STANFORD Model SR560, one enhances the signal over the sample resistance to measure the current (I), the other the voltage drop over the sample (V), obtaining the resistance as *R= V/I*. The data are acquired using a NI USB 6251 with a sampling rate of 85 kHz, collecting and averaging 5000 values every waveform cycle. Figure 66 shows the RvsT curve and Figure 67 shows the resistivity of the single microbridge and the large serpentine.

The T_C of both devices is higher than 87.5 K, which confirms the excellent quality of the films. As expected, the microbridge, shown in Figure 66a, presents a smaller resistance due to both the large thickness and the simple geometry. The nanopatterning done on the other sample, which already has a halved thickness,

strongly affects the overall resistance. Halving the thickness result in doubling the resistance but, looking at Figure 66b, it is possible to assess that the meander structure almost decuples the resistance, although slightly affecting the T_C.

a)   b)
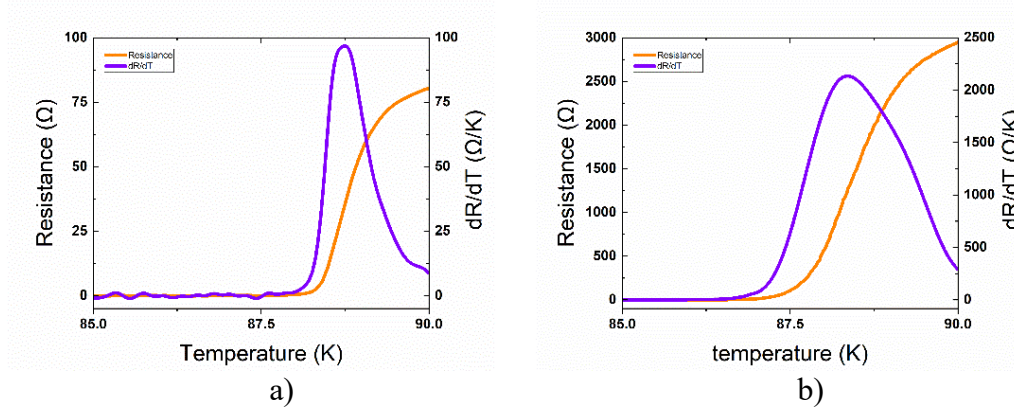
Figure 66: RvsT curve of the a) microbridge and b) the large serpentine
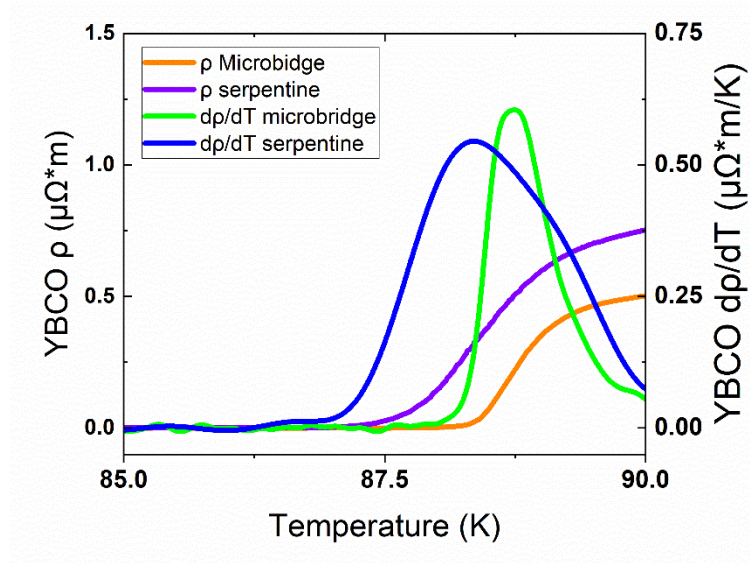
Figure 67: ρvsT curve of the microbridge and the large serpentine

From the *RvsT* curve and the geometrical parameter of the curve it is possible to obtain the ρvsT curve, which gives more information regarding the quality of the sample. Indeed, Figure 67 shows the two resistivities and their derivatives. Looking at Figure 67 it is possible to have a qualitative comparison of the film quality. In addition to a slightly lower T_C, the serpentine structure presents a broader transition, probably because of the nanofabrication process, which marginally damages the film.

6.3.5 HEB performances

From the RvsT curve, Figure 66, it is possible to analytically extrapolate the responsivity and the noise of the detector, as done previously with the TEB. For this first analysis, the microstructure is still considered as a TEB; therefore, the results are used only for a preliminary comparison between the bolometers. Because of the different phenomena behind the response time of the HEB, the time constant is not calculated since it would strongly depart from the actual value. Indeed, if the novel detector had been treated as a TEB, some qualitative calculations can be made. The smaller area and thickness of the device strongly reduce the time constant, which, considering an active area of the substrate for the heat transfer 10 times larger than the microbridge itself, results to be around 6 ns. It is a conservative result obtained for the microbridge, which may be lower considering the serpentine with even a smaller heat capacity. Table 9 presents the most critical parameters for the microstructure devices, compared with the performance of the double meander geometry. The results are obtained after the study of the optimal working point.

Table 9: performance for the three bolometers

	Double meander	Microbridge	Large serpentine
Working temperature [K]	84.78	88.62	88.34
Responsivity [V/W]	0.448	2.14	50.76
NEP $[pW/Hz^{0.5}]$	7742	171	81
Response time (τ)	0.134 μs	<1 ns (expected)	<1 ns (expected)

For the microbridge and serpentine study, the thermal conductivity of the substrate is calculated using an effective area of 125 μm x 125 μm, considerably larger than the YBCO one acting as a detector. This value, with is conservative for the responsivity, results in a smaller time constant which reaches values in the order of 0.1 ns. However, in order to be conservative, the data inserted in Table 9 considers the worst-case scenario. In addition, the bias current is limited to 0.5 mA,

although the novel detectors may work with higher currents because of the lower resistance. Nevertheless, these assumptions provide conservative results, which are already significantly better than the responsivity calculated for the double meander structure.

The total noise is calculated as the sum of the Johnson, thermal, and photon one. Unlike the previous layout, in which the predominant contribution is always the Johnson noise, for these structures, the thermal noise plays an important role, and, for some temperatures, it becomes more significant than the Nyquist one, due to the high responsivity.

A classical study of the HEB already shows great improvement with respect to the previous TEB; the smaller dimension and the higher slope of the RvsT curve results in a responsivity up to two orders of magnitude than the double meander. Similarly, the noise is extremely reduced, almost 100 times, reaching values in the order of tens of $pW/Hz^{0.5}$. The response time is expected to be reduced to a sub-nanosecond scale because of the small volume of the active part linked to a small heat capacity. The time constant would be even shorter if the 2T model is considered. Therefore, the predicted performances for the new design of the YBCO based bolometer are comparable with the modern bolometer working at high temperature and definitively better than the one obtained with the previous double meander TEB.

7. Conclusion

This thesis presents two possible detectors for THz radiation and the approach used for their optimization and design. The new devices here presented fulfil reaching the milestones of the INFN-TERA project for reducing the THz gap through the employment of efficient YBCO based detectors.

The outstanding performance of the YBCO in terms of T_C, J_C and H_{C2} can be used in electronics and power applications. Because of its technological capability to produce high-quality thin films, it is particularly suitable for detectors working at relatively high temperature. Indeed, the YBCO based devices, particularly bolometers, can be optimized to overcome the lack of THz detectors, unlocking the potentiality of the THz technology in industries and scientific research. Here, two families were analyzed: transition-edge bolometer and hot-electron bolometer.

The first TEB device, composed of a YBCO film with a double meander serpentine layout, partially modified by high-energy heavy-ion irradiation, was analyzed and the optimal working temperature was found to be 84.78 K. This value is a compromise between the one ensuring the higher responsivity and the one corresponding to the lower NEP, where the ratio between them is the highest. The performances are enhanced by the HEHI, which sharpens the RvsT curve and reduces the working temperature, resulting in higher responsivity, lower power dissipation and minor thermal noise, resulting in responsivity of values of 0.488 V/W, NEP of 7.7 $nW/Hz^{0.5}$ at a working temperature of 84.78 K. The high conductivity of the substrate, which negatively impacts the responsivity, grants a response time of around 0.13 μs.

The device was simulated through the FEM software COMSOL Multiphysics®, allowing the designing and optimizing the sensor housing, especially for what concerns the temperature distribution. It is found out that, among the studied materials, the choice of the sensor holder material just slightly affects the thermal distribution while the selection of the material of the screws strongly influences it. Therefore, it is necessary to find a good compromise between low thermal conductance, which provides a slow response to change in temperature, and high one, which does not provide a homogeneous temperature profile. The best combination is made of an aluminum holder and brass screws.

Other simulations, aiming at reproducing the response of the bolometer to external signals, show a good agreement between theoretical estimation and previously published experimental data, in terms of increase in temperature, output signal and response time. The bolometer shows a good response for train pulse signals with distances down to 7 ns, less than the time constant found from the simulated data. For intervals in the order of the substrate time constant, the bolometer completely recovers the working temperature. The FEM analysis was suitable also for more complex geometries, such as the four-meander layout, which presents a higher filling factor and a position dependent detection. The results were compared with the original design, showing that a higher output voltage is obtained for the same signal at the same working point.

A different design is explored for the HEB detector. The study, performed with SONNET®, aims at matching the input impedance, moving from a straight CPW to a microbridge. The final dimension showed a good matching impedance with the trace width of 0.4 mm, the ground plane spacing of 0.2 mm and a tapering reaching the bolometer of 0.4 mm. the structure acting as the antenna does not impact the overall matching to the 50 Ω. COMSOL Multiphysics® was used again to analyze the focusing of incoming waves for different polarizations and layouts, showing that the double slot antennas do not concentrate on the signal while the bow-tie configuration of the tapering does it.

Two different layouts, a simple microbridge and a nanopatterned serpentine, were fabricated at the Chalmers University of Technology by means of Electron Beam Lithography, obtaining precision in the nanometer order. They were then characterized and, from the RvsT curve, preliminary analysis on the performance is extrapolated. With respect to the previous TEB, the responsivity is improved by a factor of ten and one hundred, for the microbridge and the serpentine, respectively, while the NEP is reduced by the same factor. The time constant is expected to be below the nanosecond, compared with the μs of the TEB. Therefore, the new devices, which must be experimentally tested, are expected to be far better than the previous design.

References

[1] Kamerlingh Onnes, H. "The resistance of pure mercury at helium temperatures." *Commun. Phys. Lab. Univ. Leiden, b* 120 (1911).

[2] Seidel, Paul, ed. *Applied superconductivity: handbook on devices and applications*. John Wiley & Sons, 2015.

[3] London, Fritz, and Heinz London. "The electromagnetic equations of the supraconductor." *Proceedings of the Royal Society of London. Series A-Mathematical and Physical Sciences* 149.866 (1935): 71-88.

[4] Landau, Lev Davidovich, and Vitaly Lazarevich Ginzburg. "On the theory of superconductivity." *Zh. Eksp. Teor. Fiz.* 20 (1950): 1064.

[5] Bardeen, John, Leon N. Cooper, and John Robert Schrieffer. "Theory of superconductivity." *Physical review* 108.5 (1957): 1175.

[6] Webb, G. W., F. Marsiglio, and J. E. Hirsch. "Superconductivity in the elements, alloys and simple compounds." *Physica C: Superconductivity and its applications* 514 (2015): 17-27.

[7] Selvamanickam, V., et al. "Progress in second-generation HTS wire development and manufacturing." *Physica C: Superconductivity* 468.15-20 (2008): 1504-1509.

[8] Talantsev, E. F., et al. "Critical current anisotropy for second generation HTS wires." *Current Applied Physics* 8.3-4 (2008): 388-390.

[9] Bednorz, J. George, and K. Alex Müller. "Possible high Tc superconductivity in the Ba−La−Cu−O system." *Zeitschrift für Physik B Condensed Matter* 64.2 (1986): 189-193.

[10] Kamihara, Yoichi, et al. "Iron-based layered superconductor: LaOFeP." *Journal of the American Chemical Society* 128.31 (2006): 10012-10013.

[11] Kamihara, Yoichi, et al. "Iron-based layered superconductor La [$O_{1-x}F_x$]FeAs (x=0.05−0.12) with Tc=26 K." *Journal of the American Chemical Society* 130.11 (2008): 3296-3297.

[12] Meissner, Walther, and Robert Ochsenfeld. "Ein neuer effekt bei eintritt der supraleitfähigkeit." *Naturwissenschaften* 21.44 (1933): 787-788.

[13] Junod, A., et al. "Specific heat of the superconductor $YBa_2Cu_4O_8$ from 1.5 to 330 K." *Physica C: Superconductivity* 168.1-2 (1990): 47-56.

[14]   Shiffman, C. A., J. F. Cochran, and M. Garber. "The specific heat jump in superconducting lead." *Journal of Physics and Chemistry of Solids* 24.11 (1963): 1369-1373.

[15]   Brandt, Ernst Helmut, and Mukunda P. Das. "Attractive vortex interaction and the intermediate-mixed state of superconductors." *Journal of superconductivity and novel magnetism* 24.1-2 (2011): 57-67.

[16]   Grissonnanche, G., et al. "Direct measurement of the upper critical field in cuprate superconductors." *Nature communications* 5.1 (2014): 1-8.

[17]   Fetter, Alexander L., and Pierre C. Hohenberg. "Theory of type II superconductors." *Superconductivity*. Routledge, 2018. 817-923.

[18]   Bean, C. P., and J. D. Livingston. "Surface barrier in type-II superconductors." *Physical Review Letters* 12.1 (1964): 14.

[19]   Neumann, L., and L. Tewordt. "The structure of a vortex line and the lower critical field in superconducting alloys." *Zeitschrift für Physik* 189.1 (1966): 55-66.

[20]   Clem, John R. "Simple model for the vortex core in a type II superconductor." *Journal of low temperature physics* 18.5 (1975): 427-434.

[21]   Matsuda, Tsuyoshi, et al. "Magnetic field observation of a single flux quantum by electron-holographic interferometry." *Physical review letters* 62.21 (1989): 2519.

[22]   Kosterlitz, John Michael, and David James Thouless. "Ordering, metastability and phase transitions in two-dimensional systems." *Journal of Physics C: Solid State Physics* 6.7 (1973): 1181.

[23]   Essmann, U., and H. Träuble. "The direct observation of individual flux lines in type II superconductors." *Physics letters A* 24.10 (1967): 526-527.

[24]   Abrikosov, Aleksej A. "Nobel Lecture: Type-II superconductors and the vortex lattice." *Reviews of modern physics* 76.3 (2004): 975.

[25]   Alloul, H., et al. "Defects in correlated metals and superconductors." *Reviews of Modern Physics* 81.1 (2009): 45.

[26]   Song, Can-Li, et al. "Suppression of superconductivity by twin boundaries in FeSe." *Physical review letters* 109.13 (2012): 137004.

[27]   Scanlan, R. M., W. A. Fietz, and E. F. Koch. "Flux pinning centers in superconducting Nb_3Sn." *Journal of Applied Physics* 46.5 (1975): 2244-2249.

[28]   Lee, Patrick A., Naoto Nagaosa, and Xiao-Gang Wen. "Doping a Mott insulator: Physics of high-temperature superconductivity." *Reviews of modern physics* 78.1 (2006): 17.

[29]   Klein, Thierry, et al. "A Bragg glass phase in the vortex lattice of a type II superconductor." *Nature* 413.6854 (2001): 404-406.

[30]   Toft-Petersen, Rasmus, et al. "Decomposing the Bragg glass and the peak effect in a Type-II superconductor." *Nature communications* 9.1 (2018): 1-12.

[31]   Gaitonde, D. M., and T. V. Ramakrishnan. "Inertial mass of a vortex in cuprate superconductors." *Physical Review B* 56.18 (1997): 11951.

[32]   Kim, Y. B., and M. J. Stephen. "Superconductivity ed RD Parks." (1969).

[33]   Kes, P. H., et al. "Thermally assisted flux flow at small driving forces." *Superconductor Science and Technology* 1.5 (1989): 242.

[34]   Sommerfeld, Arnold. "Zur elektronentheorie der metalle." *Naturwissenschaften* 15.41 (1927): 825-832.

[35]   Abrikosov, Ai A., and L. Pr Gor'kov. "Contribution to the theory of superconducting alloys with paramagnetic impurities." *Zhur. Eksptl'. i Teoret. Fiz.* 39 (1960).

[36]   Cooper, Leon N. "Bound electron pairs in a degenerate Fermi gas." *Physical Review* 104.4 (1956): 1189.

[37]   Giaever, Ivar. "Energy gap in superconductors measured by electron tunneling." *Physical Review Letters* 5.4 (1960): 147.

[38]   Josephson, Brian David. "Possible new effects in superconductive tunnelling." *Physics letters* 1.7 (1962): 251-253.

[39]   Marsiglio, F., and J. P. Carbotte. "Superconductivity: Conventional and Unconventional Superconductors." (2008): 73-162.

[40]   Hassenzahl, W., et al. "A superconducting DC cable." *EPRI report* 1020458 (2009).

[41]   Umemoto, K., et al. "Development of 1 MW-class HTS motor for podded ship propulsion system." *Journal of Physics: Conference Series*. Vol. 234. No. 3. IOP Publishing, 2010.

[42]   https://test-emfleu.grenoble.cnrs.fr/category/tech-highlights/ (accesses December 2021)

[43]   Nishijima, Shigehiro, et al. "Superconductivity and the environment: A roadmap." *Superconductor Science and Technology* 26.11 (2013): 113001.

[44]   Alonso, Jose R., and Timothy A. Antaya. "Superconductivity in medicine." *Reviews of Accelerator Science and Technology* 5 (2012): 227-263.

[45]   Kresin, Vladimir Z., and Stuart A. Wolf. *Fundamentals of superconductivity*. Springer Science & Business Media, 2013.

[46] Ray, Pia Jensen. *Structural Investigation of La(2-x)Sr(x)CuO(4+ y): Following a Staging as a Function of Temperature*. Niels Bohr Institute, Copenhagen University, 2015.

[47] Charifoulline, Z. "Residual resistivity ratio (RRR) measurements of LHC superconducting NbTi cable strands." *IEEE transactions on applied superconductivity* 16.2 (2006): 1188-1191.

[48] Bottura, Luca. "A practical fit for the critical surface of NbTi." *IEEE transactions on applied superconductivity* 10.1 (2000): 1054-1057.

[49] Cooley, Lance, Peter Lee, and David Larbalestier. "Conductor processing of low Tc materials: the alloy Nb-Ti." (2003).

[50] Zhang, Pingxiang, et al. "NbTi superconducting wires and applications." *Titanium for Consumer Applications*. Elsevier, 2019. 279-296.

[51] Cave, J., et al. "Calculation of AC losses in ultra fine filamentary NbTi wires." *IEEE transactions on magnetics* 23.2 (1987): 1732-1735.

[52] Salunin, N., et al. "The *Jc(B,T)* Characterization of Commercial NbTi Strands for ITER PF 1&6 Coils." *IEEE transactions on applied superconductivity* 22.3 (2011): 4804604-4804604.

[53] Motowidlo, L. R., et al. "Multifilamentary NbTi with artificial pinning centers: the effect of alloy, pin material, and geometry on the superconducting properties." *IEEE transactions on applied superconductivity* 3.1 (1993): 1366-1369.

[54] Takahata, K., et al. "Coupling losses in cable-in-conduit conductors for LHD poloidal coils." *Fusion Engineering and Design* 65.1 (2003): 39-45.

[55] Zhang, WeiJun, et al. "NbN superconducting nanowire single photon detector with efficiency over 90% at 1550 nm wavelength operational at compact cryocooler temperature." *Science China Physics, Mechanics & Astronomy* 60.12 (2017): 1-10.

[56] Zhang, Lu, et al. "Hotspot relaxation time in disordered niobium nitride films." *Applied Physics Letters* 115.13 (2019): 132602.

[57] Yan, Rusen, et al. "GaN/NbN epitaxial semiconductor/superconductor heterostructures. " *Nature* 555.7695 (2018): 183-189.

[58] Ilin, K., et al. "Critical current of Nb, NbN, and TaN thin-film bridges with and without geometrical nonuniformities in a magnetic field." *Physical Review B* 89.18 (2014): 184511.

[59] Finnemore, D. K., T. F. Stromberg, and C. A. Swenson. "Superconducting properties of high-purity niobium." *Physical Review* 149.1 (1966): 231.

[60] Valente-Feliciano, Anne-Marie. "Superconducting RF materials other than bulk niobium: a review." *Superconductor Science and Technology* 29.11 (2016): 113002.

[61] Morohashi, Shin'ichi, et al. "High quality $Nb/Al-AlO_x/Nb$ Josephson junction." *Applied physics letters* 46.12 (1985): 1179-1181.

[62] Inderbitzin, Kevin, et al. "An ultra-fast superconducting Nb nanowire single-photon detector for soft x-rays." *Applied Physics Letters* 101.16 (2012): 162601.

[63] Hardy, George F., and John K. Hulm. "The superconductivity of some transition metal compounds." *Physical Review* 93.5 (1954): 1004.

[64] Testardi, L. R., J. H. Wernick, and W. A. Royer. "Superconductivity with onset above 23K in Nb_3Ge sputtered films." *Solid State Communications* 15.1 (1974): 1-4.

[65] Stewart, Greygory R. "Superconductivity in the A15 structure." *Physica C: Superconductivity and its Applications* 514 (2015): 28-35.

[66] Matthias, B. T., et al. "Superconductivity of Nb_3Sn." *Physical Review* 95.6 (1954): 1435.

[67] Xu, Xingchen. "A review and prospects for Nb_3Sn superconductor development." *Superconductor Science and Technology* 30.9 (2017): 093001.

[68] Nagamatsu, Jun, et al. "Superconductivity at 39 K in magnesium diboride." *nature* 410.6824 (2001): 63-64.

[69] Xu, Y., et al. "Time-Resolved Photoexcitation of the Superconducting Two-Gap State in MgB_2 Thin Films." *Physical review letters* 91.19 (2003): 197004.

[70] Tomsic, Michael, et al. "Overview of MgB_2 superconductor applications." *International journal of applied ceramic technology* 4.3 (2007): 250-259.

[71] Giunchi, G., et al. "High performance new MgB_2 superconducting hollow wires." *Superconductor Science and Technology* 16.2 (2003): 285.

[72] Shibata, Hiroyuki, Tatsushi Akazaki, and Yasuhiro Tokura. "Fabrication of MgB_2 nanowire single-photon detector with meander structure." *Applied Physics Express* 6.2 (2013): 023101.

[73] Kamihara, Yoichi, et al. "Iron-based layered superconductor La [$O_{1-x} F_x$] FeAs $_{(x=\ 0.05-\ 0.12)}$ with Tc= 26 K." *Journal of the American Chemical Society* 130.11 (2008): 3296-3297.

[74] Paglione, Johnpierre, and Richard L. Greene. "High-temperature superconductivity in iron-based materials." *Nature physics* 6.9 (2010): 645-658.

[75]   Hosono, Hideo, et al. "Recent advances in iron-based superconductors toward applications." *Materials today* 21.3 (2018): 278-302.

[76]   Larbalestier, David, et al. "High-Tc superconducting materials for electric power applications." *Materials For Sustainable Energy: A Collection of Peer-Reviewed Research and Review Articles from Nature Publishing Group* (2011): 311-320.

[77]   Wesche, Rainer. *Physical properties of high-temperature superconductors*. John Wiley & Sons, 2015.

[78]   Sytnikov, V. E., et al. "HTS DC cable line project: On-going activities in Russia." *IEEE transactions on applied superconductivity* 23.3 (2013): 5401904-5401904.

[79]   Shikimachi, Koji, et al. "System coordination of 2 GJ class YBCO SMES for power system control." *IEEE Transactions on Applied Superconductivity* 19.3 (2009): 2012-2018.

[80]   Terai, Motoaki, et al. "The R&D project of HTS magnets for the superconducting maglev." *IEEE transactions on applied superconductivity* 16.2 (2006): 1124-1129.

[81]   Nick, Wolfgang, Joern Grundmann, and Joachim Frauenhofer. "Test results from Siemens low-speed, high-torque HTS machine and description of further steps towards commercialisation of HTS machines." *Physica C: Superconductivity and its Applications* 482 (2012): 105-110.

[82]   Trabaldo, E., et al. "Grooved Dayem nanobridges as building blocks of high-performance $YBa_2Cu_3O_{7−δ}$ SQUID magnetometers." *Nano letters* 19.3 (2019): 1902-1907.

[83]   Chu, Hao, et al. "Phase-resolved Higgs response in superconducting cuprates." *Nature communications* 11.1 (2020): 1-6.

[84]   Miao, H., et al. "Development of Bi-2212 Conductors for Magnet Applications." *AIP Conference Proceedings*. Vol. 711. No. 1. American Institute of Physics, 2004.

[85]   Sytnikov, V. E., et al. "1G versus 2G-comparison from the practical standpoint for HTS power cables use." *Journal of Physics: Conference Series*. Vol. 97. No. 1. IOP Publishing, 2008.

[86]   Masur, L. J., et al. "Industrial HTS conductors: Status and applications." *Proc. EUCAS 2003* (2003): 15-18.

[87]   Nakashima, T., et al. "Overview of the recent performance of DI-BSCCO wire." *Cryogenics* 52.12 (2012): 713-718.

[88]   Cooley, L. D., A. K. Ghosh, and R. M. Scanlan. "Costs of high-field superconducting strands for particle accelerator magnets. " *Superconductor Science and Technology* 18.4 (2005): R51.

[89]   Iijima, Yasuhiro, and Kaname Matsumoto. "High-temperature-superconductor coated conductors: technical progress in Japan." *Superconductor Science and Technology* 13.1 (2000): 68.

[90]   Uglietti, Davide. "A review of commercial high temperature superconducting materials for large magnets: from wires and tapes to cables and conductors." *Superconductor Science and Technology* 32.5 (2019): 053001.

[91]   Tsuchiya, K., et al. "Critical current measurement of commercial REBCO conductors at 4.2 K." *Cryogenics* 85 (2017): 1-7.

[92]   Lee, Seok Ju, et al. "Recent status and progress on HTS cables for AC and DC power transmission in Korea." *IEEE Transactions on Applied Superconductivity* 28.4 (2018): 1-5.

[93]   Corato, V., et al. "Progress in the design of the superconducting magnets for the EU DEMO." *Fusion engineering and design* 136 (2018): 1597-1604.

[94]   Grilli, Francesco, et al. "Superconducting motors for aircraft propulsion: the Advanced Superconducting Motor Experimental Demonstrator project." *Journal of Physics: Conference Series*. Vol. 1590. No. 1. IOP Publishing, 2020.

[95]   Ciceron, Jeremie, et al. "Design considerations for high-energy density SMES." *IEEE Transactions on Applied Superconductivity* 27.4 (2017): 1-5.3

[96]   Tokura, Yoshinori, and Takahisa Arima. "New classification method for layered copper oxide compounds and its application to design of new high Tc superconductors." *Japanese journal of applied physics* 29.11R (1990): 2388.

[97]   Pickett, Warren E. "Electronic structure of the high-temperature oxide superconductors." *Reviews of Modern Physics* 61.2 (1989): 433.

[98]   Jorgensen, J. D., et al. "Structural properties of oxygen-deficient $YBa_2Cu_3O_{7-\delta}$." *Physical Review B* 41.4 (1990): 1863.

[99]   Chakravarty, Sudip, Hae-Young Kee, and Klaus Völker. "An explanation for a universality of transition temperatures in families of copper oxide superconductors." *Nature* 428.6978 (2004): 53-55.

[100] Van Harlingen, Dale J. "Phase-sensitive tests of the symmetry of the pairing state in the high-temperature superconductors—Evidence for d_{x2-y2} symmetry." *Reviews of Modern Physics* 67.2 (1995): 515.

[101] Tranquada, J. M., et al. "Neutron-Diffraction Determination of Antiferromagnetic Structure of Cu Ions in $YBa_2Cu_3O_{6+x}$ with x= 0.0 and 0.15." *Physical review letters* 60.2 (1988): 156.

[102] Timusk, Tom, and Bryan Statt. "The pseudogap in high-temperature superconductors: an experimental survey." *Reports on Progress in Physics* 62.1 (1999): 61.

[103] Caprara, Sergio, et al. "Dynamical charge density waves rule the phase diagram of cuprates." *Physical Review B* 95.22 (2017): 224511.

[104] Emery, V. J., and S. A. Kivelson. "Importance of phase fluctuations in superconductors with small superfluid density." *Nature* 374.6521 (1995): 434-437.

[105] Legros, A., et al. "Universal T-linear resistivity and Planckian dissipation in overdoped cuprates." *Nature Physics* 15.2 (2019): 142-147.

[106] Varma, C. M., et al. "Phenomenology of the normal state of Cu-O high-temperature superconductors." *Physical Review Letters* 63.18 (1989): 1996.

[107] Gilioli, E., et al. "Progress in the Continuous Depostition of YBCO Coated Conductors by Thermal Co-Evaporation." *Advances in Science and Technology*. Vol. 47. Trans Tech Publications Ltd, 2006.

[108] Kinder, H., et al. "YBCO film deposition on very large areas up to 20×20 cm2." *Physica C: Superconductivity* 282 (1997): 107-110.

[109] Wördenweber, R. "Growth of high-Tc thin films." *Superconductor Science and Technology* 12.6 (1999): R86.

[110] Obradors, Xavier, et al. "Progress towards all-chemical superconducting $YBa_2Cu_3O_7$ coated conductors." *Superconductor Science and Technology* 19.3 (2006): S13.

[111] Faley, M. I., et al. "High-Tc SQUID biomagnetometers." *Superconductor science and technology* 30.8 (2017): 083001.

[112] Trabaldo, E., et al. "Transport and noise properties of YBCO nanowire based nanoSQUIDs." *Superconductor Science and Technology* 32.7 (2019): 073001.

[113] Ruffieux, S., et al. "The role of kinetic inductance on the performance of YBCO SQUID magnetometers." *Superconductor Science and Technology* 33.2 (2020): 025007.

[114] Du, J., et al. "Fabrication and characterisation of series YBCO step-edge Josephson junction arrays." *Superconductor Science and Technology* 27.9 (2014): 095005.

[115] Aghabagheri, S., et al. "High temperature superconducting YBCO microwave filters." *Physica C: Superconductivity and its Applications* 549 (2018): 22-26.

[116] Snigirev, Oleg V., et al. "Superconducting quantum interference filters as RF amplifiers." *IEEE transactions on applied superconductivity* 17.2 (2007): 718-721.

[117] Medema, A. R., G. Ghigo, and S. K. Remillard. "Influence of columnar defects on magnetic relaxation of microwave nonlinearity in superconducting YBCO resonator devices." *Physica C: Superconductivity and its Applications* 583 (2021): 1353849.

[118] Thoma, Petra, et al. "Highly responsive Y–Ba–Cu–O thin film THz detectors with picosecond time resolution." *IEEE transactions on applied superconductivity* 23.3 (2012): 2400206-2400206.

[119] Probst, Petra, et al. "Nonthermal response of $YBa_2Cu_3O_{7-\delta}$ thin films to picosecond THz pulses." *Physical Review B* 85.17 (2012): 174511.

[120] Gao, Xiang, et al. "A wideband terahertz high-Tc superconducting Josephson-junction mixer: electromagnetic design, analysis and characterization." *Superconductor Science and Technology* 30.9 (2017): 095011.

[121] Malnou, M., et al. "High-Tc superconducting Josephson mixers for terahertz heterodyne detection." *Journal of Applied Physics* 116.7 (2014): 074505.

[122] Nazifi, Rana, et al. "Millimeter-Wave Response of All Metal-Organic Deposited YBCO Transition Edge Bolometer." *IEEE Transactions on Applied Superconductivity* 31.1 (2020): 1-5.

[123] Moahjeri, Roya, et al. "Demonstration of Thermal Images Captured by a Backside Illuminated Transition Edge Bolometer." *arXiv preprint arXiv:2108.10154* (2021).

[124] Kraus, H. "Superconductive bolometers and calorimeters." Superconductor Science and Technology 9.10 (1996): 827.

[125] Leung, M., et al. "Optical detection in thin granular films of Y-Ba-Cu-O at temperatures between 4.2 and 100 K." Applied physics letters 51.24 (1987): 2046-2047.

[126] Forrester, M. G_, et al. "Optical response of epitaxial and granular films of $YBa_2Cu_3O_{7-\delta}$ at temperatures from 25 K to 100 K." IEEE Transactions on Magnetics 25.2 (1989): 1327-1330.

[127] Dwir, B., and D. Pavuna. "A sensitive YBaCuO thin film bolometer with ultrawide wavelength response." Journal of applied physics 72.9 (1992): 3855-3861.

[128] Tong, F. M., et al. "High Tc $YBa_2Cu_3O_{7-\delta}$ superconducting transition-edge microbolometers." Infrared physics & technology 36.7 (1995): 1053-1058.

[129] Li, Kin, Joseph E. Johnson, and Bruce W. Aker. High responsivity YBa$_2$Cu$_3$O$_{7-x}$ microbolometers with fast response times. Journal of applied physics 73.3 (1993) 1531-1533.

[130] Janik, D., et al. "High-T$_C$ transition-edge bolometer for detecting guided millimeter waves." IEEE transactions on applied superconductivity 3.1 (1993): 2148-2151.

[131] Fardmanesh, Mehdi. "Analytic thermal modeling for dc-to-midrange modulation frequency responses of thin-film high-Tc superconductive edge-transition bolometers." Applied optics 40.7 (2001): 1080-1088.

[132] Nazifi, Rana, et al. "Millimeter-wave response of all metal-organic deposited YBCO transition edge bolometer." IEEE Transactions on Applied Superconductivity 31.1 (2020): 1-5.

[133] Robbes, D., et al. "YBCO microbolometer operating below T$_C$: a modelization based on critical current-temperature dependence." IEEE transactions on applied superconductivity 3.1 (1993): 2120-2123.

[134] Eidelloth, W. "Optical response of highly oriented YBCO thin films." IEEE transactions on magnetics 27.2 (1991): 2828-2831.

[135] Kakehi, Yoshiharu, et al. Infrared radiation detector with YBa$_2$Cu$_3$O$_X$ thin film. Japanese journal of applied physics 37.9R (1998) 4774.

[136] Khrebtov, I. A. "Noise properties of high temperature superconducting bolometers." Fluctuation and Noise Letters 2.02 (2002): R51-R70.

[137] Nahum, M., et al. "Fabrication and measurement of high T$_C$ superconducting microbolometers." IEEE Transactions on magnetics 27.2 (1991): 3081-3084.

[138] Karmanenko, S. F., et al. "Fabrication process and noise properties of antenna-coupled microbolometers based on superconducting YBCO films." Superconductor Science and Technology 13.3 (2000): 273.

[139] Leonov, V. N., and I. A. Khrebtov. "Stability and noise of fast YBaCuO antenna microbolometers on sapphire substrates." Technical Physics Letters 20.12 (1994): 951-953

[140] Hammar, Arvid, et al. "Terahertz Direct Detection in YBa$_2$CuO$_7$ Microbolometers." IEEE Transactions on Terahertz Science and Technology 1.2 (2011): 390-394.

[141] Lakew, B., et al. "High-Tc superconducting bolometer on chemically-etched 7 μm thick sapphire." Physica C: Superconductivity 329.2 (2000): 69-74.

[142] Stratton, T. G., et al. "High-temperature superconducting microbolometer." Applied physics letters 57.1 (1990): 99-100.

[143] Péroz, Christophe, et al. "Fabrication and characterization of ultrathin PBCO/YBCO/PBCO constrictions for hot electron bolometer THz mixing application." IEEE transactions on applied superconductivity 17.2 (2007): 637-640.

[144] Kreisler, Alain J., et al. "New Trend in THz Detection: High Tc Superconducting Hot Electron Bolometer Technology May Exhibit Advantage vs Low Tc Devices." 2007 IEEE/MTT-S International Microwave Symposium. IEEE, 2007.

[145] Li, C-T., et al. Low power submillimeter-wave mixing and responsivity properties of $YBa_2Cu_3O_7$ hot-electron bolometers. Applied physics letters 71.11 (1997) 1558-1560.

[146] Lee, Mark, et al. "Nonlinear THz mixing in YBaCuO thin film hot electron bolometers." Superconducting and Related Oxides: Physics and Nanoengineering III. Vol. 3481. SPIE, 1998.

[147] Villegier, Jean-Claude, et al. Fabrication of high-Tc superconducting hot electron bolometers for terahertz mixer applications. Terahertz and Gigahertz Electronics and Photonics IV. Vol. 5727. SPIE, 2005.

[148] Ladret, Romain G., Alain J. Kreisler, and Annick F. Dégardin. "YBCO-constriction hot spot modeling: DC and RF descriptions for HEB THz mixer noise temperature and conversion gain." IEEE Transactions on Applied Superconductivity 25.3 (2014): 1-5.

[149] Cherednichenko, S., et al. "$YBa_2Cu_3O_{7-\delta}$ hot-electron bolometer mixer at 0.6 THz." Proc. 11th Int. Symp. Space Terahertz Technol. 2000.

[150] Gol'Tsman, Gregory N. "Hot electron bolometric mixers: new terahertz technology." Infrared physics & technology 40.3 (1999): 199-206.

[151] Focardi, Paolo, William R. McGrath, and Andrea Neto. "Design guidelines for terahertz mixers and detectors." IEEE Transactions on microwave theory and techniques 53.5 (2005): 1653-1661.

[152] Novoselov, Evgenii, et al. "Noise measurements of the low Tc MgB_2 HEB mixer at 1.6 THz and 2.6 THz." Proc. ISSTT conference. 2015.

[153] Shurakov, Alexander, et al. "Input bandwidth of hot electron bolometer with spiral antenna." Ieee transactions on terahertz science and technology 2.4 (2012): 400-405.

[154] Rönnung, Fredrik, et al. A nanoscale YBCO mixer optically coupled with a bow tie antenna. Superconductor Science and Technology 12.11 (1999) 853.

[155] Semenov, Alexei D., et al. Terahertz performance of integrated lens antennas with a hot-electron bolometer. IEEE transactions on microwave theory and techniques 55.2 (2007) 239-247.

[156] Naftaly, Mira, Nico Vieweg, and Anselm Deninger. "Industrial applications of terahertz sensing: state of play." *Sensors* 19.19 (2019): 4203.

[157] Sirtori, Carlo. "Bridge for the terahertz gap." *Nature* 417.6885 (2002): 132-133.

[158] Welp, Ulrich, Kazuo Kadowaki, and Reinhold Kleiner. "Superconducting emitters of THz radiation." *Nature Photonics* 7.9 (2013): 702-710.

[159] Delfanazari, Kaveh, et al. "Integrated, portable, tunable, and coherent terahertz sources and sensitive detectors based on layered superconductors." *Proceedings of the IEEE* 108.5 (2020): 721-734.

[160] Dhillon, S. S., et al. "The 2017 terahertz science and technology roadmap." *Journal of Physics D: Applied Physics* 50.4 (2017): 043001.

[161] Farrah, Duncan, et al. "far-infrared instrumentation and technological development for the next decade." *Journal of Astronomical Telescopes, Instruments, and Systems* 5.2 (2019): 020901.

[162] Gong, Aiping, et al. "Biomedical applications of terahertz technology." *Applied Spectroscopy Reviews* 55.5 (2020): 418-438.

[163] Wang, Kaiqiang, Da-Wen Sun, and Hongbin Pu. "Emerging non-destructive terahertz spectroscopic imaging technique: Principle and applications in the agri-food industry." *Trends in Food Science & Technology* 67 (2017): 93-105.

[164] Chen, Zhi, et al. "A survey on terahertz communications." *China Communications* 16.2 (2019): 1-35.

[165] Elayan, Hadeel, et al. "Terahertz band: The last piece of RF spectrum puzzle for communication systems." *IEEE Open Journal of the Communications Society* 1 (2019): 1-32.

[166] Choudhury, Balamati, Aniruddha R. Sonde, and Rakesh Mohan Jha. "Terahertz antenna technology for space applications." *Terahertz Antenna Technology for Space Applications*. Springer, Singapore, 2016. 1-33.

[167] Kulesa, Craig. "Terahertz spectroscopy for astronomy: From comets to cosmology." *IEEE Transactions on Terahertz Science and Technology* 1.1 (2011): 232-240.

[168] Kemp, Michael C., et al. "Security applications of terahertz technology." *Terahertz for Military and Security Applications*. Vol. 5070. International Society for Optics and Photonics, 2003.

[169] Liu, Hai-Bo, et al. "Detection and identification of explosive RDX by THz diffuse reflection spectroscopy." *Optics Express* 14.1 (2006): 415-423.

[170] Zhong, Shuncong. "Progress in terahertz nondestructive testing: A review." *Frontiers of Mechanical Engineering* 14.3 (2019): 273-281.

[171] Afsah-Hejri, Leili, et al. "A comprehensive review on food applications of terahertz spectroscopy and imaging." *Comprehensive reviews in food science and food safety* 18.5 (2019): 1563-1621.

[172] Afsah-Hejri, Leili, et al. "Terahertz spectroscopy and imaging: A review on agricultural applications." *Computers and Electronics in Agriculture* 177 (2020): 105628.

[173] Patil, Mangesh R., et al. "Terahertz spectroscopy: Encoding the discovery, instrumentation, and applications toward pharmaceutical prospectives." *Critical Reviews in Analytical Chemistry* (2020): 1-13.

[174] Yakasai, Izaddeen Kabir, Pg Emeroylariffion Abas, and Feroza Begum. "Review of porous core photonic crystal fibers for terahertz waveguiding." *Optik* (2021): 166284.

[175] Rogalski, Antoni. *Infrared and Terahertz Detectors*. CRC Press, 2019.

[176] Rieke, George. *Detection of Light: from the Ultraviolet to the Submillimeter*. Cambridge University Press, 2003.

[177] Sizov, F., and A. Rogalski. "THz detectors." *Progress in quantum electronics* 34.5 (2010): 278-347.

[178] Hubers, Heinz-Wilhelm. "Terahertz heterodyne receivers." *IEEE journal of selected topics in quantum electronics* 14.2 (2008): 378-391.

[179] Fernandes, L. O. T., et al. "Photometry of THz radiation using Golay cell detector." *2011 XXXth URSI General Assembly and Scientific Symposium*. IEEE, 2011.

[180] Kolenov, I. V., et al. "Application Features of Pyroelectric Detector for THz Wave Receiving." *2020 IEEE Ukrainian Microwave Week (UkrMW)*. IEEE, 2020.

[181] Slocombe, L. L., and R. A. Lewis. "Electrical versus optical: Comparing methods for detecting terahertz radiation using neon lamps." *Journal of Infrared, Millimeter, and Terahertz Waves* 39.8 (2018): 701-713.

[182] Elamaran, Durgadevi, et al. "Comparative Study on 1-THz Antenna-Coupled Bolometer with Various SOI-CMOS based Temperature Sensors: MOSFET, Diode, Resistor and Thermocouple." *2019 Silicon Nanoelectronics Workshop (SNW)*. IEEE, 2019.

[183] Simoens, François. "THz bolometer detectors." *Physics and Applications of Terahertz Radiation*. Springer, Dordrecht, 2014. 35-75.

[184] Rumyantsev, V. V., et al. "Terahertz photoconductivity of double acceptors in narrow gap HgCdTe epitaxial films grown by molecular

beam epitaxy on GaAs (013) and Si (013) substrates." *Semiconductor Science and Technology* 32.9 (2017): 095007.

[185] Ulbricht, Gerhard, Mario De Lucia, and Eoin Baldwin. "Applications for microwave kinetic induction detectors in advanced instrumentation." *Applied Sciences* 11.6 (2021): 2671.

[186] Otsuji, Taiichi, and Akira Satou. "Plasma-Wave Devices." *THz Communications*. Springer, Cham, 2022. 291-296.

[187] Li, Zhuang, et al. "A 0.32-THz SiGe imaging array with polarization diversity." *IEEE Transactions on Terahertz Science and Technology* 8.2 (2018): 215-223.

[188] Kutas, Mirco, et al. "Terahertz quantum sensing." *Science advances* 6.11 (2020): eaaz8065.

[189] Groppi, Christopher E., and Jonathan H. Kawamura. "Coherent detector arrays for terahertz astrophysics applications." *IEEE Transactions on Terahertz Science and Technology* 1.1 (2011): 85-96.

[190] M. Cestelli Guidi (Resp), E. Chiadroni, A. Marcelli, M. Marongiu (Ass. Ric.), J. Rezvani (Ass. Ric.) - TERA - CSN5 - Annual Report

[191] Marongiu, M., et al. "Electromagnetic and Beam Dynamics Studies for High Gradient Accelerators at Terahertz Frequencies." *Journal of Physics: Conference Series*. Vol. 1596. No. 1. IOP Publishing, 2020.

[192] Rezvani, S. J., et al. "A cryogenic magneto-optical device for long wavelength radiation." *Review of Scientific Instruments* 91.7 (2020): 075103.

[193] Pavlou, Christos, et al. "Effective EMI shielding behaviour of thin graphene/PMMA nanolaminates in the THz range." *Nature Communications* 12.1 (2021): 1-9.

[194] Langley, Samuel Pierpont. *The" bolometer"*. The Society, 1881.

[195] Datskos, Panos G., and Nickolay V. Lavrik. "Detectors—figures of merit." *Encyclopedia of Optical Engineering* 349 (2003): 100.

[196] Rogalski, A., and F. Sizov. "Terahertz detectors and focal plane arrays." *Opto-electronics review* 19.3 (2011): 346-404.

[197] Maul, M. K., and M. W. P. Strandberg. "Equivalent circuit of a superconducting bolometer." *Journal of Applied Physics* 40.7 (1969): 2822-2827.

[198] Richards, P. L. "Bolometers for infrared and millimeter waves." *Journal of Applied Physics* 76.1 (1994): 1-24.

[199] Lakew, B., et al. "High-Tc, transition-edge superconducting (TES) bolometer on a monolithic sapphire membrane—construction and performance." *Sensors and Actuators A: Physical* 114.1 (2004): 36-40.

[200] Mather, John C. "Bolometer noise: nonequilibrium theory." *Applied optics* 21.6 (1982): 1125-1129.

[201] Moftakharzadeh, A., et al. "Detectivity of YBCO transition edge bolometer: modulation frequency, bias current and absorber effects." *Journal of Physics: Conference Series*. Vol. 97. No. 1. IOP Publishing, 2008.

[202] Galeazzi, Massimiliano. "Fundamental noise processes in TES devices." *IEEE Transactions on Applied Superconductivity* 21.3 (2010): 267-271.

[203] Laviano, F., et al. "Thickness dependence of the current density distribution in superconducting films." *Physica C: Superconductivity* 404.1-4 (2004): 220-225.

[204] Prusseit, W., S. Furtner, and R. Nemetschek. "Series production of large area $YBa_2Cu_3O_7$ films for microwave and electrical power applications." *Superconductor Science and Technology* 13.5 (2000): 519.

[205] Berberich, P., et al. "Low-temperature preparation of superconducting $YBa_2Cu_3O_{7-\delta}$ films on Si, MgO, and $SrTiO_3$ by thermal coevaporation." *Applied physics letters* 53.10 (1988): 925-926.

[206] Bauer, M., R. Semerad, and H. Kinder. "YBCO films on metal substrates with biaxially aligned MgO buffer layers." *IEEE transactions on applied superconductivity* 9.2 (1999): 1502-1505.

[207] Ramesh, R., et al. "Epitaxy of Y-Ba-Cu-O thin films grown on single-crystal MgO." *Applied physics letters* 56.22 (1990): 2243-2245.

[208] Zhao, Pei, Akihiko Ito, and Takashi Goto. "Rapid deposition of YBCO films by laser CVD and effect of lattice mismatch on their epitaxial growth and critical temperature." *Ceramics International* 39.7 (2013): 7491-7497.

[209] Mazierska, Janina, et al. "Precise microwave characterization of MgO substrates for HTS circuits with superconducting post dielectric resonator." *Superconductor Science and Technology* 18.1 (2004): 18.

[210] Lee, Sang Yeol, Kwang Yong Kang, and Dal Ahn. "Fabrication of YBCO superconducting dual mode resonator for satellite communication." *IEEE Transactions on Applied Superconductivity* 5.2 (1995): 2563-2566.

[211] Smith, Deane K., and H. R. Leider. "Low-temperature thermal expansion of LiH, MgO and CaO." *Journal of Applied Crystallography* 1.4 (1968): 246-249.

[212] Kawashima, Junichi, Yasuji Yamada, and Izumi Hirabayashi. "Critical thickness and effective thermal expansion coefficient of YBCO crystalline film." *Physica C: Superconductivity* 306.1-2 (1998): 114-118.

[213] Bosu, S., et al. "Thermal artifact on the spin Seebeck effect in metallic thin films deposited on MgO substrates." *Journal of Applied Physics* 111.7 (2012): 07B106.

[214] Mishra, S. K., et al. "Lithographic patterning of superconducting YBCO films." *Journal of superconductivity* 5.5 (1992): 445-449.

[215] Gerbaldo, R., et al. "Functional decoupling of nanostructured areas in superconducting strips for electromagnetic detectors." *Journal of Applied Physics* 104.6 (2008): 063919.

[216] Laviano, F., et al. "Evidence of vortex curvature and anisotropic pinning in superconducting films by quantitative magneto-optics." *Physical Review B* 68.1 (2003): 014507.

[217] Yan, Y., and M. A. Kirk. "Observation and mechanism of local oxygen reordering induced by high-energy heavy-ion (U^+, Au^+, Xe^+) irradiation in the high-Tc superconductor $YBa_2Cu_3O_{7-\delta}$." *Physical Review B* 57.10 (1998): 6152.

[218] Laviano, F., et al. "Rugged superconducting detector for monitoring infrared energy sources in harsh environments." *Superconductor Science and Technology* 23.12 (2010): 125008.

[219] Gerbaldo, R., et al. "Nanostructuring YBCO thin films by heavy-ion beam for local magnetic field and infrared photon detection." *Nuclear Instruments and Methods in Physics Research Section B: Beam Interactions with Materials and Atoms* 272 (2012): 291-295.

[220] Lupi S., Laviano F. "THz spectroscopy of heavy-ion irradiated MgO and YSZ crystals*", in preparation*

[221] Benford, Dominic J., Michael C. Gaidis, and Jacob W. Kooi. "Optical properties of Zitex in the infrared to submillimeter." *Applied optics* 42.25 (2003): 5118-5122.

[222] Fardmanesh, Mehdi, Kevin J. Scoles, and Allen Rothwarf. "Control of the responsivity and the detectivity of superconductive edge-transition $YBa_2Cu_3O_{7-x}$ bolometers through substrate properties." *Applied optics* 38.22 (1999): 4735-4742.

[223] "COMSOL: Multiphysics Software for Optimizing Designs," *COMSOL*. https://www.comsol.com/ (accessed Dec. 10, 2021).

[224] Arsenault, Alexandre, Frédéric Sirois, and Francesco Grilli. "Implementation of the H-Φ formulation in COMSOL Multiphysics for simulating the magnetization of bulk superconductors and comparison with the H-formulation." *IEEE Transactions on Applied Superconductivity* 31.2 (2020): 1-11.

[225] Fracasso, Michela, et al. "Modelling and Performance Analysis of MgB2 and Hybrid Magnetic Shields." *Materials* 15.2 (2022): 667.

[226] Zandi, Soma, et al. "Simulation of CZTSSe thin-film solar cells in COMSOL: Three-dimensional optical, electrical, and thermal models." *IEEE Journal of Photovoltaics* 10.5 (2020): 1503-1507.

[227] Golubev, D., Floriana Lombardi, and Thilo Bauch. "Effect of heating on critical current of YBCO nanowires." *Physica C: Superconductivity and its Applications* 506 (2014): 174-177.

[228] Murakami, Yusuke, et al. "Measurement of Out-of-Plane Thermal Conductivity of Epitaxial $YBa_2Cu_3O_{7-\delta}$ Thin Films in the Temperature Range from 10 K to 300 K by Photothermal Reflectance." *International Journal of Thermophysics* 38.10 (2017): 160.

[229] Phillips, Norman E., et al. "Specific Heat of $YBa_2Cu_3O_7$: Origin of the" Linear" Term and Volume Fraction of Superconductivity." *Physical review letters* 65.3 (1990): 357. Bosu, S., et al. "Thermal artifact on the spin Seebeck effect in metallic thin films deposited on MgO substrates." *Journal of Applied Physics* 111.7 (2012): 07B106.

[230] Hofmeister, Anne M. "Thermal diffusivity and thermal conductivity of single-crystal MgO and Al_2O_3 and related compounds as a function of temperature." *Physics and Chemistry of Minerals* 41.5 (2014): 361-371.

[231] Ed. Douglas Mann, LNG Materials and Fluids National Bureau of Standards, Cryogenics Division First Edition, 1977.

[232] NIST Material Measurement Laboratory, https://trc.nist.gov/cryogenics/materials/materialproperties.htm, / (accessed Dec. 10, 2021)

[233] Ed. Holly M. Veres, Thermal Properties Database for Materials at Cryogenic Temperatures. Volume 1

[234] Powell, R.L., Rogers, W.M., and Roder, H.M., Thermal Conductivities of Copper and Copper Alloys Advances in Cryogenic Engineering vol. 2, 1956, pp. 166-171.

[235] N. J.Simon, E.S.Drexler, and R.P.Reed, Properties of Copper and Copper Alloys at Cryogenic Temperature. NIST Monograph 177.

[236] Napolitano, Andrea, et al. "Study of the thermal distribution for YBCO based Transition Edge Bolometers working above 77 K." *2021 IEEE 14th Workshop on Low Temperature Electronics (WOLTE)*. IEEE, 2021.

[237] Napolitano, Andrea, et al. "Multiphysics simulation of a superconducting bolometer working in a portable cryostat." *Journal of Physics: Conference Series*. Vol. 1559. No. 1. IOP Publishing, 2020.

[238] Di Fabrizio, Marta, et al. "Performance evaluation of a THz pulsed imaging system: point spread function, broadband THz beam

visualization and image reconstruction." *Applied Sciences* 11.2 (2021): 562.

[239] Seliverstov, Sergey, et al. "Fast and sensitive terahertz direct detector based on superconducting antenna-coupled hot electron bolometer." *IEEE Transactions on Applied Superconductivity* 25.3 (2014): 1-4.

[240] Hayton, D. J., et al. "A 4.7 THz heterodyne receiver for a balloon borne telescope." *Millimeter, Submillimeter, and Far-Infrared Detectors and Instrumentation for Astronomy VII*. Vol. 9153. International Society for Optics and Photonics, 2014.

[241] Thoma, Petra, et al. "Real-time measurement of picosecond THz pulses by an ultra-fast $YBa_2Cu_3O_{7-d}$ detection system." *Applied Physics Letters* 101.14 (2012): 142601.

[242] Pals, Jan A., et al. "Non-equilibrium superconductivity in homogeneous thin films." *Physics Reports* 89.4 (1982): 323-390.

[243] Perrin, N., and C. Vanneste. "Response of superconducting films to a periodic optical irradiation." *Physical Review B* 28.9 (1983): 5150.

[244] Stockhausen, Axel. *Optimization of hot-electron bolometers for THz radiation*. Vol. 8. KIT Scientific Publishing, 2013.

[245] Semenov, Alexei D., Gregory N. Gol'tsman, and Roman Sobolewski. "Hot-electron effect in superconductors and its applications for radiation sensors." *Superconductor Science and Technology* 15.4 (2002): R1.

[246] Gousev, Yu P., et al. "Electron-phonon interaction in disordered NbN films." *Physica B Condensed Matter* 194 (1994): 1355-1356.

[247] Bergmann, Gerd. "Weak localization in thin films: a time-of-flight experiment with conduction electrons." *Physics Reports* 107.1 (1984): 1-58.

[248] Karasik, B. S., W. R. McGrath, and M. C. Gaidis. "Analysis of a high-Tc hot-electron superconducting mixer for terahertz applications." *Journal of applied physics* 81.3 (1997): 1581-1589.

[249] Cherednichenko, S., et al. "Terahertz superconducting hot-electron bolometer mixers." Physica C: Superconductivity 372 (2002): 407-415.

[250] Ladret, Romain, et al. "THz Mixing with High-TC Hot Electron Bolometers: A Performance Modeling Assessment for Y-Ba-Cu-O Devices." Photonics. Vol. 6. No. 1. MDPI, 2019.

[251] Gershenzon, E. M. "Millimeter and submillimeter range mier based on electronic heating of superconducting films in the resistive state." *Sov. Phys. Supercond.* 3 (1990): 1582-1597.

[252] Gao, Jianrong, et al. "Development of THz Nb diffusion-cooled hot-electron bolometer mixers." *Millimeter and Submillimeter Detectors*

for Astronomy. Vol. 4855. International Society for Optics and Photonics, 2003.

[253] Dalrymple, Bruce J., et al. "Inelastic electron lifetime in niobium films." *Physical Review B* 33.11 (1986): 7514.

[254] Kaplan, Steven B. "Acoustic matching of superconducting films to substrates." *Journal of Low Temperature Physics* 37.3 (1979): 343-365.

[255] Gousev, Yu P., et al. "Broad-band coupling of THz radiation to an hot-electron bolometer mixer." *Superconductor Science and Technology* 9.9 (1996): 779.

[256] Kaganov, M. I., E. M. Lifshitz, and L. V. Tanatarov. "Relaxation between electrons and the crystalline lattice." *Soviet Physics-JETP* 4 (1957): 173-178.

[257] Semenov, A. D., et al. "Evidence for the spectral dependence of nonequilibrium picosecond photoresponse of YBaCuO thin films." *Applied physics letters* 63.5 (1993): 681-683.

[258] Skocpol, W. J., M. R. Beasley, and M. Tinkham. "Self-heating hotspots in superconducting thin-film microbridges." *Journal of Applied Physics* 45.9 (1974): 4054-4066.

[259] Floet, D. Wilms, et al. "Hotspot mixing: A framework for heterodyne mixing in superconducting hot-electron bolometers." *Applied physics letters* 74.3 (1999): 433-435.

[260] a - Lindgren, M., et al. "Intrinsic picosecond response times of Y–Ba–Cu–O superconducting photodetectors." Applied Physics Letters 74.6 (1999): 853-855.

[261] b - Pepe, G. P., et al. "Novel superconducting proximized heterostructures for ultrafast photodetection." Cryogenics 49.11 (2009): 660-664.

[262] c - Time-resolved optical response of all-oxide YBa2Cu3O7/La0.7Sr0.3MnO3 proximitized bilayersRothwarf, Allen, and B. N. Taylor. "Measurement of recombination lifetimes in superconductors." *Physical Review Letters* 19.1 (1967): 27.

[263] Grossman, Erich N., Donald G. McDonald, and J. E. Sauvageau. "Far-infrared kinetic-inductance detectors." *IEEE transactions on magnetics* 27.2 (1991): 2677-2680.

[264] https://www.microwaves101.com/calculators/864-coplanar-waveguide-calculator visited 02-january 2022

[265] Simons, Rainee N. *Coplanar waveguide circuits, components, and systems*. Vol. 165. John Wiley & Sons, 2004.

[266] Harrington, Roger F. *Field computation by moment methods*. Wiley-IEEE Press, 1993.

[267] Subramanian, M. A., et al. "Dielectric constants of BeO, MgO, and CaO using the two-terminal method." *Physics and chemistry of minerals* 16.8 (1989): 741-746.

[268] Alford, N. McN, et al. "Dielectric loss of oxide single crystals and polycrystalline analogues from 10 to 320 K." *Journal of the European Ceramic Society* 21.15 (2001): 2605-2611.

[269] Avenhaus, B., et al. "Microwave properties of YBCO thin films." *IEEE Transactions on Applied Superconductivity* 5.2 (1995): 1737-1740.

[270] https://www.sonnetsoftware.com/support/downloads/guide.pdf visited 02-january 2022

[271] Brorson, S. D., et al. "Kinetic inductance and penetration depth of thin superconducting films measured by THz-pulse spectroscopy." *Physical Review B* 49.9 (1994): 6185.

[272] Trabaldo, E., et al. "Properties of grooved Dayem bridge based $YBa_2Cu_3O_{7-\delta}$ superconducting quantum interference devices and magnetometers." *Applied Physics Letters* 116.13 (2020): 132601.

[273] P. Benzi, E. Bottizzo, and N. Rizzi. "Oxygen determination from cell dimensions in YBCO superconductors." *Journal of Crystal Growth* 269.2-4 (2004): 625-629.